

# Steep, Spatially Graded Recruitment of Feedback Inhibition by Sparse Dentate Granule Cell Activity

Dissertation  
zur  
Erlangung des Doktorgrades (Dr. rer. nat.)  
der  
Mathematisch-Naturwissenschaftlichen Fakultät  
der  
Rheinischen Friedrich-Wilhelms-Universität Bonn

vorgelegt von  
Oliver Braganza  
aus  
Fulda

Bonn 2015

Angefertigt mit Genehmigung der  
Mathematisch-Naturwissenschaftlichen Fakultät der  
Rheinischen-Friedrich-Wilhelms-Universität Bonn

1. Gutachter: Prof. Dr. Heinz Beck
2. Gutachter: Prof. Dr. Michael Pankratz

Promotionsdatum: 20.04.2016

Erscheinungsjahr: 2016



# Acknowledgements

This thesis would not exist without the help of many people. First and foremost, I want to thank my supervisor, Heinz Beck, whose unwavering support during the last years provided the basis for every aspect of this work. I am also indebted to my Cosupervisor, Michael Pankratz, who represents the faculty of natural sciences. Beside these, many others, inside and outside of our group, have contributed critical ideas and insights and a pleasant atmosphere. Especially Tony Kelly, Dirk Dietrich, Thoralf Opitz, Holger Dannenberg, Leonie Pothmann, Milan Pabst and Martin Pofahl helped me with practical as well as theoretical problems. They provided insightful feedback and suggested relevant experiments and practical solutions to problems at many stages of this thesis. I also want to thank Olivia Stefan, Kristina Piwellek and Dominik Holtkamp for breeding and genotyping mice and Margit Reitze, Rommy Liebchen-Lutat and Sabrina Minacapilli for administrative assistance. Further, I am grateful to Stefan Remy and his group for the opportunity to use their multibeam two-photon microscope and facilities. Finally, I would like to thank my family for everything they gave me (including, presumably, a large part of my character and skillset) and friends (some of which happen to have already been mentioned above).

# Abstract

The dentate gyrus of the hippocampus is thought to subserve important physiological functions, such as 'pattern separation'. In chronic temporal lobe epilepsy, the dentate gyrus constitutes a strong inhibitory gate for the propagation of seizure activity into the hippocampus proper. Both examples are thought to depend critically on a steep recruitment of feedback inhibition by active dentate granule cells. Here, I used two complementary experimental approaches to quantitatively investigate the recruitment of feedback inhibition in the dentate gyrus. I showed that the activity of approximately 4 % of granule cells suffices to recruit maximal feedback inhibition within the local circuit. Furthermore, the inhibition elicited by a local population of granule cells is distributed non-uniformly over the extent of the granule cell layer. Locally and remotely activated inhibition differ in several key aspects, namely their amplitude, recruitment, latency and kinetic properties. Finally, I show that net feedback inhibition facilitates during repetitive stimulation. Taken together, these data provide the first quantitative functional description of a canonical feedback inhibitory microcircuit motif. They establish that sparse granule cell activity, within the range observed *in-vivo*, steeply recruits spatially and temporally graded feedback inhibition.

# Content

<b>1. Introduction</b> .....	<b>1</b>
1.1 Neuronal Representations – Insights from Computational Neuroscience .....	2
1.1.1 The Neuronal Code in Time and Space .....	3
1.1.2 Network Oscillations .....	5
1.1.3 Sparse Coding and the Generalization – Discrimination Trade-off.....	6
1.2 Inhibition.....	11
1.2.1 GABA <sub>A</sub> Receptors.....	11
1.2.2 GABA <sub>B</sub> Receptors.....	12
1.2.3 Interneuron Diversity .....	13
1.3 Temporal Organization of Network Activity.....	15
1.4 Inhibitory Microcircuit Motifs .....	16
1.4.1 Feedforward Inhibition and Input Normalization .....	16
1.4.2 Tuning and Selection of Inputs and Outputs.....	17
1.4.3 Feedback Inhibition and Output Normalization.....	18
1.5 The Dentate Gyrus of the Hippocampal Formation .....	20
1.5.1 Anatomy and Physiology of the Dentate Gyrus .....	21
1.5.2 Microcircuitry of the Dentate Gyrus .....	22
1.6 Pattern Separation in the Dentate Gyrus .....	24
1.6.1 The Proposed Role of Feedback Inhibition in Pattern Separation.....	25
1.7 Key Questions .....	26
<b>2. Materials and Methods</b> .....	<b>27</b>
2.1 Animals and Slice Preparation .....	27
2.2 Obtaining Maximum Connectivity Plane Sections .....	27
2.3 Electrophysiological Recordings .....	28
2.4 Pharmacology .....	30
2.5 Dual Patch Experiments.....	30
2.6 Ca <sup>2+</sup> Imaging.....	30
2.7 Electrical Stimulation .....	32
2.8 Calculation of the Recruitment of Feedback Inhibition for Imaging Experiments....	32
2.9 Optogenetic Stimulation.....	33
2.10 Measurement of the Fluorescence Intensity Profile .....	33
2.11 Calculation of the Optogenetically Activated Cell Fraction.....	34

2.12	Comparison of Focal and Global Activation .....	36
2.13	Spatial Distribution of Feedback Inhibition .....	36
2.14	Frequency Dependence of Feedback Inhibition.....	37
2.15	Analysis .....	37
<b>3.</b>	<b>Results .....</b>	<b>39</b>
3.1	Population Ca <sup>2+</sup> Imaging Assessment of the Recruitment of Feedback Inhibition....	39
3.1.1	Detection of Single Action Potentials by Population Ca <sup>2+</sup> Imaging.....	40
3.1.2	Determination of the Maximum Connectivity Plane .....	42
3.1.3	Selective Activation of Feedback Inhibitory Currents .....	44
3.1.4	Steep Recruitment of Feedback Inhibition (1) .....	45
3.2	Optogenetic Assessment of the Recruitment of Feedback Inhibition .....	46
3.2.1	Optogenetic Activation of Feedback Inhibitory Currents .....	47
3.2.2	Optogenetic Activation of Granule Cells .....	49
3.2.3	Steep Recruitment of Feedback Inhibition (2) .....	52
3.3	Absence of Single GC Induced Feedback Inhibition .....	53
3.4	Spatial Distribution of Feedback Inhibition .....	54
3.4.1	Amplitude of Local and Remote Inhibition at Saturation .....	54
3.4.2	Recruitment of Local and Remote Feedback Inhibition.....	56
3.4.3	Kinetic Properties of Local and Remote Feedback Inhibition .....	56
3.5	Frequency Dependence of Feedback Inhibition.....	57
<b>4.</b>	<b>Discussion .....</b>	<b>59</b>
4.1	Major Findings .....	59
4.2	Methodological Considerations.....	59
4.2.1	Electrical Activation and Population Ca <sup>2+</sup> Imaging.....	60
4.2.2	Focal Optogenetic Granule Cell Activation .....	62
4.3	The Recruitment of Feedback Inhibition .....	63
4.3.1	Comparison of the Active Cell Fraction between Studies.....	64
4.3.2	Recruitment of Feedback Inhibition with One to Three Principal Cells.....	66
4.3.3	Comparison of Feedforward and Feedback Inhibition .....	67
4.3.4	Translamellar Feedback Inhibition .....	69
4.4	Spatial Distribution of Feedback Inhibition .....	70
4.4.1	Non-uniform Distribution of Feedback Inhibition.....	71
4.4.2	Functional Implications .....	72
4.5	The Time Course of Feedback Inhibition .....	74
4.5.1	The Temporal Window of Assembly Competition .....	75
4.5.2	Facilitation of Net Feedback Inhibition .....	77

4.6	Implications for the Local Feedback Inhibitory Microcircuitry.....	77
4.6.1	Spatial Distribution of Feedback Inhibition.....	78
4.6.2	Short Term Dynamics of Feedback Inhibition .....	82
4.6.3	Cooperativity between Feedforward and Feedback Inhibition .....	83
4.7	Role of immature GCs.....	84
4.7.1	The Temporal Tag Hypothesis.....	84
4.7.2	Rate Coding or Population Coding .....	85
4.8	Implications for DG function in Health and Disease.....	86
<b>5.</b>	<b>Summary.....</b>	<b>88</b>
<b>6.</b>	<b>Bibliography.....</b>	<b>90</b>
<b>7.</b>	<b>List of Abbreviations.....</b>	<b>107</b>

# 1. Introduction

Across species, the nervous system has evolved to perceive information about the external world, process that information in a meaningful way, and initiate appropriate responses to it. In order to do this, it is thought to represent the information in networks of neuronal cells. These neuronal networks are compartmentalized into modules, each of which performs a particular processing function before the information is passed on to the next module. The term module here is used to describe any neuronal population which acts as a functional unit. Each module is composed of individual neuronal cells which, upon activation, produce action potentials (APs), also referred to as spikes, that are transmitted along the axon to their target synapses. A projection neuron which innervates cells in a downstream module (generally towards the motor output) is termed feedforward while one that projects to upstream regions (generally towards the sensory input) is termed feedback. Additionally, cells within a given module are often interconnected in various complex ways. The principal agents for the transmission of information in the nervous system are networks of glutamatergic principal cells, which represent approximately 80 to 90 % of neurons across cortical areas. Upon activation, these neurons release the excitatory neurotransmitter glutamate and thereby activate their target cells, by eliciting fast excitatory postsynaptic currents (EPSCs), which lead to a transient membrane depolarization (EPSP).

Within modules or local populations, a particular pattern of activity of principal cells is thought to represent a particular piece of information about the external or internal world. Depending on the brain area, this information may be closely related to individual sensory organs; for instance the firing rates of neurons in the visual cortex may represent the orientation of a bar in the visual field (Hubel and Wiesel, 1962). Alternatively the information represented may be inherently multisensory, such as the representation in the hippocampus of the spatial context of an electrical foot shock (Fanselow, 2000). How exactly neuronal activity patterns are shaped in space and time in order to represent and process information is perhaps the most important unresolved question in neuroscience. In the following I will first outline some empirical and computational investigations into the general nature of

neuronal representations and computations (chapter 1.1). I will then briefly introduce the major form of inhibition in the central nervous system along with the cell types that mediate it (chapter 1.2). A major function of inhibition is the temporal organization of network activity (chapter 1.3). Next, I will introduce a number of ‘canonical inhibitory microcircuit motifs’ which are thought to be the physical substrates of important general network functions (chapter 1.4). Finally, I will introduce the dentate gyrus (DG) of the hippocampal formation including its anatomy, specific cell types and microcircuit structure (chapter 1.5). The DG is one of the best studied brain regions in which a number of these microcircuit motifs are thought to be of particular importance for physiological as well as pathological reasons. Of particular interest is the function of pattern separation, which is thought to critically depend on feedback inhibition (chapter 1.6). I will conclude the introduction by precisely formulating the key questions this thesis was designed to answer (chapter 1.7).

## 1.1 Neuronal Representations – Insights from Computational Neuroscience

How information is represented in the spiking activity of neuronal networks is often referred to as the ‘neural code’. In order to investigate the neural code (or codes) neuroscientists search for correlations between external stimuli or motor actions and neuronal firing patterns. The main challenges in such investigations are the probabilistic nature and the high dimensionality of the underlying processes. Additionally, the coded information itself is often highly complex. Any investigation of neural representations is therefore by necessity reductionist and forced to rely on assumptions about the probabilistic model, the relevant dimensions and the coded information. In the following chapter I will first outline empirically established individual dimensions of neural coding (section 1.1.1) and introduce the network oscillations in which these dimensions appear to be organized (section 1.1.2). I will then proceed to briefly describe how computational models have been used to integrate these findings, leading to the hypothesis of sparse, temporally parsed coding (section 1.1.3).

### 1.1.1 The Neuronal Code in Time and Space

Due mainly to experimental constraints, most empirical investigations have concentrated on the information represented in the temporal organization of spikes in individual neurons, i.e. the temporal dimension. The workhorse in empirical as well as theoretical neuroscience has been the ‘rate-code’ hypothesis, which posits that information is primarily coded by the firing rate of individual neurons within a certain predefined time window (deCharms and Zador, 2000). Indeed, rate coded information has been found at a variety of different levels of abstraction, ranging from direct sensory parameters (Adrian and Zotterman, 1926) over visual orientation selectivity (Hubel and Wiesel, 1962) to inherently multisensory representations such as place specific firing (O’Keefe and Dostrovsky, 1971). In addition to being a simple readout, rate coding has the practical advantage, that the firing rate for any particular neuron can be represented by a single number, making it computationally tractable. Frequently reported properties of the input-output function of individual neurons, such as gain, sensitivity, and dynamic range, were developed on the basis of the rate code assumption (**Fig. 1**; Silver, 2010). The gain is the slope of the input-output curve (**Fig. 1**, blue bar). It determines the sensitivity with which a neuron can respond to changes in input strength. The dynamic range is the total range of input strengths to which a neuron can differentially respond (**Fig. 1**, green bar). It is bounded by the firing threshold and the maximal firing rate of the cell (**Fig. 1**; left and right green dashed line respectively).

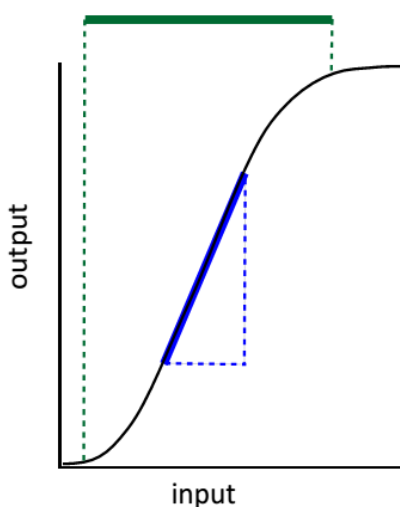


**Fig. 1) Properties of input-output functions,** Input-output functions can be used to describe the rate coded transformation of individual neurons as well as for populations of neurons or local circuits. Two central properties of the input-output function can be described: The gain (blue bar) is the slope of the input-output function. It defines the sensitivity of the output to small changes in input. The dynamic range (green bar) is the range of inputs to which cell/population/circuit can differentially respond. For individual neurons the input may be defined as the current during a current injection, the stimulus intensity of a sensory stimulus or the firing rate of presynaptic cells. The output is then generally the firing rate or firing probability of the neuron. At the population or local circuit level the input may be measured as the mean firing rate or the active fraction of an upstream population. The output may then be defined as the mean firing rate or active cell fraction of the population itself. In the case of local microcircuits, the output can also be measured at the target population.

However, there is general consensus among neuroscientists that information is represented not by individual cells, but by the combined activity of populations of neurons, a notion

often denoted the 'population code' hypothesis (Ince et al., 2010; Trappenberg, 2010). Fortunately, the concepts of gain, sensitivity and dynamic range can also be used at the population level by considering for instance the mean firing rates across cells (**Fig. 1**; Busse et al., 2009; Pouille et al., 2009). Population coding is attractive because using combinations of neurons to code for information dramatically increases the networks capacity (Foldiak, 2002). A quantitative intuition of how population coding affects network capacity will be developed in section 1.1.3. Since individual neurons occupy distinct locations in space, a pattern defined by which neurons fire APs and which do not is often referred to as 'spatial'. A central concept in this respect is that of the Hebbian cell assembly (Buzsáki, 2010; Harris, 2005; Hebb, 1949). According to it, neural representations are held by assemblies of cells, where the identity of the representation is defined by the composition of the assembly. It has been inspired by the realization that under certain conditions synapses undergo plasticity, that is they are strengthened or weakened in a highly specific manner (Bliss and Lomo, 1973; Kandel et al., 2000). Two connected principal neurons which fire in close temporal proximity, for instance because one participates in the recruitment of the other, can undergo associative plasticity forming a strengthened connection with one another. A group of neurons, which by this process has formed strengthened or 'potentiated' connections in response to a particular stimulus, can now be preferentially activated by this stimulus. Importantly, a variety of different plasticity mechanisms exist, including long and short term potentiation and depression (LTP, LTD, STP, and STD), spike timing dependent plasticity (STDP) and many other forms. These mechanisms differ with respect to the direction, strength, and duration of plasticity. Each is conveyed by a distinct molecular cascade depending on the precise pattern of pre and postsynaptic activity (Bliss and Lomo, 1973; Kandel et al., 2000). Together these plasticity mechanisms are thought to finely tune the synaptic connectivity matrix termed the 'synapsemble', which is thought to structurally underlie the formation of cell assemblies (Buzsáki, 2010). Direct evidence for the representation of information in cell assemblies has emerged only relatively recently due to technical advances, which permitted the recording and manipulation of sufficiently sized neuronal populations at cellular resolution (Guzowski et al., 1999; Liu et al., 2012; Pastalkova et al., 2008; Skaggs et al., 1996). This view focuses on the information represented by the spatial dimension. It should be noted however, that the concept of cell assembly is relatively loose and may refer to functionally defined groups of cells at a variety of spatial and temporal

scales (Buzsáki, 2010). But how are the spatial and temporal dimensions of neuronal coding coordinated? One of the most salient aspects of neural network function is its temporal organization into various behavior-dependent oscillatory patterns or ‘rhythms’ (Buzsaki, 2006; Singer, 1999; Steriade and Timofeev, 2003).

### 1.1.2 Network Oscillations

The presence of network oscillations has been observed by recording the summed electrical fields of multiple neurons since Hans Berger invented the electro-encephalogram (EEG) in 1929 (Wiedemann, 1994). Field potential oscillations are apparent at a variety of spatial scales, from the macroscopic EEG to the mesoscopic local field potential (LFP), and temporal scales from the slow delta (0.5-3 Hz) and theta (3-10 Hz) to the fast gamma (30-90 Hz) and ultrafast (90-200 Hz) ranges (Buzsáki and Draguhn, 2004). The presence of such oscillations has long suggested that they serve to temporally organize network function and it has thus been natural to regard them as a temporal reference for the activity of individual neurons. In fact, the investigation of how cellular and subcellular activity is organized with respect to network oscillations has been a central and fruitful theme in modern neuroscience (Buzsaki, 2006). The duration of the oscillation cycles is thought to parse neuronal activity into defined time windows (Buzsáki, 2010; Roux and Buzsáki, 2014). Such time windows have been suggested to define the duration of individual Hebbian cell assemblies and structure their progression in time (Buzsáki, 2010). Analogously, the transient synchronization of oscillations across brain areas has been suggested to underlie the ‘binding’ of features encoded in the respective areas (Gray et al., 1989; Singer, 1999). Finally, the co-occurrence of oscillations at different frequencies, such as theta nested gamma, has been suggested to serve the hierarchical organization of cell assemblies and subassemblies within and across brain regions (Buzsáki, 2010).

It is the combination of spatial and temporal codes, organized into network rhythms, which results in the extraordinarily high dimensionality of neuronal representations. It allows information to be coded not only in firing rates of individual cells or spatial patterns of activity, but also in the relative timing of spikes to each other or to field potential oscillations (Buračas et al., 1998; deCharms and Merzenich, 1996; O’Keefe and Recce, 1993; Skaggs et

al., 1996; Harris, 2005). The central approach to investigate how spatial and temporal codes can work together in order to represent information has been computational neuroscience (Rolls and Treves, 1998; Trappenberg, 2010). The field has supplied empirical neuroscientists not only with mathematical tools to define relevant parameters, but integrates empirical findings into a larger framework. By investigating how simplified neuronal population models can represent and process information, computational neuroscientists are providing means to interpret empirical findings and, perhaps more importantly, generate hypotheses which can be tested experimentally. One general result from computational models has been that a particularly advantageous mode of coding for neuronal networks is ‘sparse coding’ (Foldiak, 2002; Trappenberg, 2010). It combines a relatively high representational capacity with high memory capacity, fast learning, good generalization, controlled interference, high fault tolerance and parallel processing capacity (Foldiak, 2002). In the next section I will develop an intuition on how sparse coding achieves some of these properties and what they mean using a highly simplified but intuitive model.

### 1.1.3 Sparse Coding and the Generalization – Discrimination Trade-off

Why does the ‘sparseness’ of neuronal representation matter? Firstly, it affects the capacity of the network, which is defined as the number of discrete items the network can represent or that can be read out from it. This can be seen in various complex network models as described in standard textbooks of computational neuroscience (Trappenberg, 2010). However, a much simpler model can be used to develop an intuition of the relevance of sparsity for the capacity of the network. Let us assume a population of neurons at a single time point, where each element can be either ‘on’ or ‘off’. Based on Shannon's (1948) theory of information, the number of possible different combinations of active neurons is equivalent to the maximum number of discrete pieces of information, which could theoretically be represented (Trappenberg, 2010). In such a network the number of distinct patterns scales roughly exponentially with the number of cells that participate in a typical representation (for small active cell fractions; Trappenberg, 2010). Specifically, the maximal number of possible representations is given simply by the binomial operator (**Fig. 2A**; Eq. 1),

$$\text{Equation 1} \quad \text{Capacity} = \binom{n}{k}$$

where the total population contains  $n$  cells and an active pattern contains  $k$  cells. The active cell fraction is then given by  $k/n$ . Importantly this general relation holds true even if neurons have more than two states (in fact most computational models rely on rate coded information). If more than 50 % of neurons are simultaneously active, the relation can be reversed, for instance when assuming the simple two-state model of neurons. However, due to the high metabolic cost of firing APs this domain is deemed of little importance in biological systems (**Fig. 2B**). In fact, a biological network is assumed to attempt to minimize the number of spikes necessary for any given representation in order to minimize energy consumption (Attwell and Laughlin, 2001). Therefore the storage capacity of a neuronal population can be increased either by increasing the active cell fraction ( $k/n$  with  $k/n \leq 50\%$ ) or alternatively by increasing the total population size ( $n$ ), both at the cost of higher energy consumption. Importantly, in the simple model described above, the differential activity of a single cell changes the identity of the pattern. However, this makes it highly prone to misclassification or destructive inference between similar patterns if the inputs are noisy. This leads directly to a second central insight from computational neuroscience.

In any network there is a trade-off between its generalization and discrimination capabilities. Generalization refers to the ability to reactivate a complete pattern, even if the input pattern is noisy or incomplete, a notion also referred to as pattern recognition or pattern completion. Discrimination, on the other hand, refers to the ability of a network to differentially represent, respond to, or categorize separate input patterns. The two represent fundamentally opposing forces. If a network generalizes one pattern from a similar pattern, then it can by definition not discriminate between the two. Although this trade-off has been studied primarily in the hippocampus, it is apparent in a variety of different network models for different brain areas with different underlying assumptions (Barak et al., 2013; Myers and Scharfman, 2009; O'Reilly and McClelland, 1994; Olshausen and Field, 1996; Rolls, 2013).

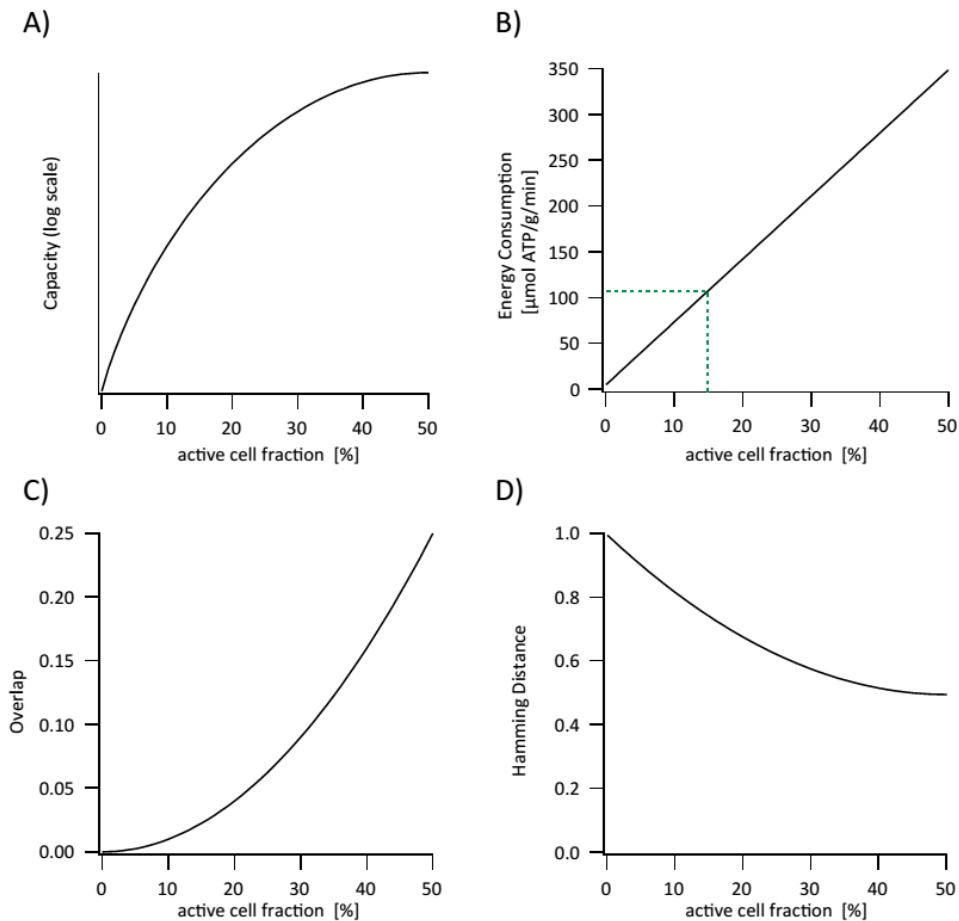


**Fig. 2) Effect of the active cell fraction on network parameters,** A simple population model can be used to illustrate the effect of the active cell fraction on central network parameters. It considers a single time point in which neurons can be only active or inactive, where  $n$  is the total cell number and  $k$  the active cell number. **A)** A measure of the maximum storage capacity of such a population is given by the number of possible combinations to choose  $k$  active cells from  $n$  total cells  $\binom{n}{k}$ . Accordingly, the capacity can be increased by increasing the active cell fraction ( $k/n$ ) or the total population size  $n$ . **B)** An estimate of the energy consumption based on (Attwell and Laughlin, 2001), assuming the active cell fraction is assessed in 10 ms windows. The authors estimate that due to metabolic constraints the active cell fraction must remain  $< 15\%$  (green dashed lines) **C)** A measure of the similarity between two representations of a given active cell fraction is the expected overlap between the two representations. The expected overlap is given by the mean probability that a cell will be active in both representations  $(k/n)^2$ , assuming random sampling. This measure of similarity corresponds to the mathematical concept of correlation, where the two populations are viewed as two binary vectors. **D)** An alternative measure of similarity between two binary vectors, common in computer science, is the Hamming Distance. It registers not only co-active cells but also co-inactive cells as overlap and is given by  $(k/n)^2 + (1 - k/n)^2$ .

But what is the physiological significance of generalization and discrimination? Generalization is thought to be the principal goal of associative plasticity and, for instance, allow the formation of mnemonic associations. Accordingly it has been the subject of a large body of literature including the generalization capabilities of competitive networks and

various types of attractor networks (Amit et al., 1987; Hopfield, 1982; Rolls, 2010; Trappenberg, 2010). Discrimination, on the other hand is believed to be the basis of the separation and categorization of objects and contexts (Santoro, 2013; Trappenberg, 2010). The closely related process of making patterns less correlated between one brain region and the next, in order to allow more efficient discrimination, is referred to as pattern separation or pattern orthogonalization (a detailed introduction into pattern separation will follow in section 1.6; for a disambiguation of terms see Santoro, 2013). If the two input patterns are noisy or partial representations of the same stimulus or context, generalization reflects fault tolerance or correct recognition. However, if the two input patterns reflect different but similar stimuli, generalization reflects destructive interference between these patterns, leading to defective discrimination. Accordingly, both an ability to generalize and an ability to discriminate will affect the functional capacity of the network. Specifically, the capacity of the network will be proportional to its discrimination capabilities, but only as long as each individual piece of information can be successfully recognized by generalization.

The trade-off between discrimination and generalization capabilities is controlled by the sparseness of representation. This relation has been described in a large body of literature based on the work of Marr (1969, 1971), McNaughton and Morris (1987) and O'Reilly and McClelland (1994) and developed in the theories such as 'competitive networks and self-organizing maps' (Rolls, 2010; Rolls and Treves, 1998; Trappenberg, 2010) as well as learning tools such as 'support vector machines' (Aimone et al., 2011; for a general demonstration see Barak et al., 2013). An intuitive understanding of the relation between sparseness and the discrimination-generalization trade-off can be gained from the realization that the sparseness of representation is expected to be inversely related to the overlap between individual patterns. To see this, we can again consider the simple two-state neuron model introduced above. Assuming a random selection of cells for any two patterns of a given active cell fraction, the mean overlap between the two patterns will be given by the square of this fraction (**Fig. 2C**). Mean overlap refers to the fraction of the total population which is expected to participate in both patterns and is identical to the correlation of two binary population vectors. Increased overlap between two patterns leads to better generalization and increased fault tolerance. However, it also leads to increased destructive interference implying decreased discrimination capability and decreased functional capacity. 'Overlap' as a measure of similarity here, is measured only for the co-active elements, as in the more

general mathematical measure of ‘correlation’. An alternative measure of similarity common in computer science is the ‘Hamming distance’ which counts not only co-active but also co-inactive elements as overlap (**Fig. 2D**). The Hamming distance decreases until 50 % of cells are active. Though it is not certain which measure of similarity is more appropriate, the use of Hamming distance can lead to hypotheses of networks in which close to 50 % of cells are active (Myers and Scharfman, 2009), which is not consistent with biological observations and not plausible from a metabolic perspective (Attwell and Laughlin, 2001; Foldiak, 2002). Finally, it is important to realize that the optimal degree and permissible range of sparsity will depend on the precise task of the network, particularly with respect to its generalization and discrimination capabilities (Barak et al., 2013).

In conclusion, computational models have long predicted that sparse coding strikes an optimal balance between the different requirements of a network. An abundance of experimental evidence across brain regions and species supports the role of sparse coding and confirms the nature of the underlying trade-offs (Crochet et al., 2011; Fujisawa et al., 2008; Hromádka et al., 2008; Lin et al., 2014; Papadopoulou et al., 2011; Schneider and Woolley, 2013; Vinje and Gallant, 2000). How then, do networks maintain and regulate sparse coding? And how do they accomplish the other network functions such as the formation and selection of cell assemblies and their temporal coordination. There are a number of relevant factors including the connectivity and plasticity between and within excitatory neurons, and intrinsic neuronal properties such as firing threshold, maximal firing rate, and dendritic properties. All these parameters, by necessity, play a role. However, another essential ingredient of neural network activity is inhibition. It has been suggested as a particularly efficient and robust way to regulate sparsity (Binas et al., 2014; Carandini and Heeger, 2012; Rolls, 2010) and organize network activity in space and time (Roux and Buzsáki, 2014). In the following chapter I will introduce GABAergic inhibition, the most important source of inhibition in the central nervous system.

## 1.2 Inhibition

GABAergic inhibition is exerted by a highly diverse population of inhibitory interneurons (Klausberger and Somogyi, 2008). Although they only represent 10 to 20 % of neurons across brain areas, they potentially control the activity level in the network as well as the spatiotemporal organization of principal cell firing (Goldberg and Coulter, 2013; Roux and Buzsáki, 2014). This can be achieved by either feedforward or feedback inhibition. The unifying feature of all these diverse cells is that, upon activation, they release the neurotransmitter  $\gamma$ -aminobutyric acid (GABA), the major inhibitory neurotransmitter in the brain. Binding of GABA to its postsynaptic receptor will generally lead to inhibitory postsynaptic currents (IPSCs) and inhibitory postsynaptic potentials (IPSPs). GABA receptors can be differentiated into two general types, GABA<sub>A</sub> and GABA<sub>B</sub> receptors, which are present on virtually every neuron in the brain (Mody and Pearce, 2004).

### 1.2.1 GABA<sub>A</sub> Receptors

GABA<sub>A</sub> receptors are members of the Cys-loop pentameric ligand gated anion channel superfamily and mediate the major form of fast inhibitory neurotransmission in the central nervous system (Kandel et al., 2000; Olsen and Sieghart, 2008). The five subunits can be selected from eight classes with one to six known isoforms,  $\alpha$ 1-6,  $\beta$ 1-3,  $\gamma$ 1-3,  $\delta$ ,  $\epsilon$ ,  $\pi$ ,  $\theta$ ,  $\rho$ 1-3, where the class is denoted by a Greek letter followed by the number of isoforms. A receptor's regional and subcellular expression pattern as well as its pharmacological and physiological properties are dependent on its subunit composition (Brickley and Mody, 2012). Synaptic GABA<sub>A</sub> receptors give rise to a rapid phasic inhibitory postsynaptic conductance and are generally composed of two  $\alpha$ , two  $\beta$  and one  $\gamma$  subunit. Depending on the exact subunit composition of the receptors within individual cells and even individual synapses (Strüber et al., 2015) the conductances they produce differ in time course as well as sensitivity for different modulatory mechanisms. On the other hand, extra and perisynaptic GABA<sub>A</sub> receptors have been shown to mediate a tonic inhibitory conductance in a variety of cells (Brickley and Mody, 2012; Nusser and Mody, 2002). Subunits associated with tonic conductances are most prominently the  $\delta$ -subunit but also the  $\alpha$ 5 subunit. Such tonic GABA conductances make a major contribution to the total charge flow across the

membrane and can modulate the firing mode of neurons as well as their general activity level. This is thought to happen primarily due to GABA spillover from synaptic into extrasynaptic areas. Both phasic and tonic GABA<sub>A</sub> conductances generally lead to a hyperpolarization of the neuronal cell membrane which is mediated by an inflow of Cl<sup>-</sup>. However, when the Cl<sup>-</sup> reversal potential is close to or above the resting membrane potential, but still below the AP threshold, the GABAergic Cl<sup>-</sup> conductance can attenuate excitatory conductances without affecting the membrane potential, a mechanism denoted 'shunting inhibition'. Depending on the relative location of the excitatory and inhibitory channels this mechanism can be highly effective (Chiang et al., 2012; Gidon and Segev, 2012).

### 1.2.2 GABA<sub>B</sub> Receptors

GABA<sub>B</sub> receptors are members of the G-protein coupled receptor (GPCR) superfamily characterized by its seven-transmembrane structure (Kandel et al., 2000). Functional GABA<sub>B</sub> receptors are heterodimers consisting of a GABA<sub>B1</sub> and a GABA<sub>B2</sub> subunit both of which are required for successful membrane trafficking. They can be located either presynaptically or postsynaptically depending on the isoform of the GABA<sub>B1</sub> subunit (Gassmann and Bettler, 2012). Upon extracellular binding of the ligand these receptors undergo a conformational change resulting in the dissociation of a bound intracellular G-protein trimer. On the one hand, the G<sub>αi/o</sub> subunit initiates the adenylyl cyclase/protein kinase A second messenger cascade affecting a variety of cellular and network processes by complex interactions with other intracellular messaging cascades. On the other hand, the G<sub>βγ</sub> subunits lead to activation of inward-rectifying K<sup>+</sup> channels and inhibition of voltage gated Ca<sup>2+</sup> channels (Bettler, 2004). Both mechanisms are generally thought to lead to slow inhibition and to be incapable of the rapid dynamic regulation of network activity ascribed to GABA<sub>A</sub> mediated inhibition (Mott and Lewis, 1994; but see Craig and McBain, 2014).

### 1.2.3 Interneuron Diversity

Interneurons can be differentiated on the basis of their morphology, connectivity, gene expression, and electrophysiological properties (Klausberger and Somogyi, 2008; Somogyi and Klausberger, 2005). Although they can be divided into individual classes according to all of these criteria, it is important to bear in mind that the resulting classifications are sometimes ambiguous and often overlap. Moreover, the number of described interneuron classes is growing rapidly (Roux and Buzsáki, 2014). Similar to principal cells, a general distinction can be made between interneurons based on their anatomical orientation with respect to the inputs and outputs of a given region. Interneurons receiving input from a principal cell population and then projecting to the downstream targets of that population are termed feedforward. Conversely, if the interneurons project back to the same principal cell population by which they are excited, they are termed feedback interneurons. It is noteworthy, that while this is generally a valuable functional distinction, most interneurons actually receive feedforward as well as feedback inputs from different regions (Roux and Buzsáki, 2014; Sambandan et al., 2010). Moreover, the notion of feedforward and feedback are dependent on what is functionally conceived of as a population and what is considered to be the predominant direction of information flow. A closely related concept is lateral inhibition which may be implemented by feedforward or feedback circuits (Lin et al., 2014; Olsen et al., 2010; Roux and Buzsáki, 2014). The term describes inhibition of neurons at the same level which are in some respect functionally distinct, for instance coding for a competing feature of input space such as a different odor. In the following I will only briefly introduce the most studied interneuron types, which appear to be repeated across brain areas, based on the criteria by Somogyi and Klausberger (2005) as well as Roux and Buzsáki (2014). A more detailed description of the specific instances of these cell types in the DG, the brain region investigated in this study, will follow in chapter 1.5.2

A central characteristic, by which interneurons can be differentiated, is their target area along the somato-dendritic axis of the postsynaptic cells (Miles, 1990; Miles et al., 1996). According to this criterion, the largest group of interneurons is the perisomatically targeting group (Roux and Buzsáki, 2014). It contains the probably most studied type of interneuron, the fast spiking, parvalbumin expressing ( $PV^+$ ) basket cell (BC), named after its basket like axonal plexus around the principal cell soma (Hu et al., 2014).  $PV^+$  BCs are characterized by

an exceptionally high peak firing rate (>150 Hz at 34° C), short AP duration and fast dendritic processing. Other perisomatically targeting interneurons include slower spiking, cholecystinin expressing (CCK<sup>+</sup>), PV<sup>-</sup> basket cells and PV<sup>+</sup> or PV<sup>-</sup> axo-axonic cells, the latter group selectively innervating the axon initial segment of principal cells. For simplicity, the term BC is often used to refer to only the fast spiking, PV<sup>+</sup> subpopulation of BC, a nomenclature that will be followed here in order to facilitate referencing the relevant literature (Savanthrapadian et al., 2014).

A second highly diverse group of GABAergic cells are the dendrite targeting interneurons. Every excitatory pathway in the cortex is matched by a type of feedforward interneuron, which is activated by, and inhibits the same subcellular compartments as, this pathway (Buzsáki, 1984). Another well studied dendrite targeting interneuron, which appears to be repeated across cortical regions, is characterized by its expression of somatostatin (SST<sup>+</sup>) and innervation of only the distal dendrites of their respective principal cell population. This group includes the Oriens-Lacunosum Moleculare interneurons and the Hilar Perforant Path associated cells (HIPPA) in the DG, both of the hippocampal formation. These interneurons are considered typical feedback interneurons, since they receive most of their inputs from the same principal cell population they innervate. Additional subclasses of interneurons target two or more dendritic domains such as the PV<sup>+</sup> and SST<sup>+</sup> bistratified cells.

A third group of interneurons preferentially innervates other interneurons effectively providing disinhibition of principal cells (Gulyas et al., 1996; Pi et al., 2013). Molecular markers associated with such interneurons include vasoactive intestinal polypeptide and calretinin.

Finally, a fourth major group of interneurons are GABAergic cells with long range projections. These cells are not 'interneurons' in the sense that they are only locally connected but are sometimes included in the class of interneurons due to their expression of GABA. With respect to their morphology and marker expression these cells are highly diverse (Caputi et al., 2013). This extraordinary diversity is thought to reflect the diversity of functions that interneurons perform. In the following two chapters I will outline how inhibition gives rise to some of the computational functions described in chapter 1.1, including mechanisms to temporally organize network activity, to select cells and to regulate sparsity.

### 1.3 Temporal Organization of Network Activity

One of the main functions attributed to interneurons is the generation and organization of network oscillations (Bartos et al., 2007; Chrobak and Buzsáki, 1995; Fukunaga et al., 2014; for a recent review see Roux and Buzsáki, 2014). By supplying rhythmic inhibition to principal cells, interneurons can synchronize principal cells at different time scales thereby effectively generating or enhancing mesoscopic field potential oscillations (Bartos et al., 2002; Cardin et al., 2009; Dannenberg et al., 2015). By restricting principal cell activity to specific time windows, interneurons can create a temporal frame for transiently active cell assemblies (Buzsáki, 2010). Furthermore, this synchronization, or more generally temporal organization, provides the basis for the various forms of synaptic plasticity that shape the synapse.

Rhythmic interneuron activity may be generated intrinsically (Elgueta et al., 2015; Royer et al., 2012), within interneuron networks (Bartos et al., 2007; Hu et al., 2011), or by the interactions of interneuron-principal cell networks. Different types of interneurons have been suggested to be preferentially involved in different oscillation frequencies. Fast spiking, perisomatically inhibiting interneurons in gamma oscillations (Bartos et al., 2007; Hu et al., 2014; Sohal et al., 2009) and slower dendritically inhibiting interneurons in theta oscillations (Fukunaga et al., 2014; Varga et al., 2012; but see Amilhon et al., 2015).

Beside this general role of creating rhythmicity in neuronal networks, interneurons may also define the integration time window of excitatory postsynaptic events during transmission from one brain area to the next (Gabernet et al., 2005; Pouille and Scanziani, 2001). This mechanism controls the temporal precision of principal cell spiking through perisomatically inhibiting interneurons, thereby increasing the temporal fidelity of a population response (Pouille and Scanziani, 2001). It may be important if information is coded not only in the composition of the assembly within an oscillatory window, but in the precise temporal relation of neuronal events.

## 1.4 Inhibitory Microcircuit Motifs

Together with the cells which supply the excitatory and inhibitory inputs and those that receive their postsynaptic outputs, interneurons have been found to form stereotypic inhibitory microcircuit motifs, each adapted to a specific function (Douglas and Martin, 1991; Roux and Buzsáki, 2014). Such functions include the spatiotemporal organization of inputs onto the dendritic trees of principal cells, input normalization, input and output tuning, and population activity control. Some of these microcircuit motifs have so far been described in detail only in a specific brain region, others have been found in multiple brain regions. It is important to point out that any particular function will arise from the interplay between most or all the elements of the network, thus generally involving more than one microcircuit motif as well as long range connections. Similarly, any given interneuron is likely to participate in multiple motifs and functions. However, it has been a valuable approach to associate individual motifs to particular functions in order to dissect the underlying network mechanisms (Carandini and Heeger, 2012; Hu et al., 2014; Roux and Buzsáki, 2014). Such mechanisms have often proven to be generalizable and allow us to reach a better understanding of network function as a whole. In the following, I will introduce some of these microcircuit motifs and how the specific anatomical connectivity and physiological properties of the participating interneurons are believed to give rise to particular functions.

### 1.4.1 Feedforward Inhibition and Input Normalization

The computations which can be performed in a network critically depend on the input strength of that network. Too large input strengths may lead to saturation, rendering the network unable to differentially respond to variations of these inputs. Similarly, too weak inputs may be insufficient to activate enough cells to allow for efficient processing. The range of input strengths, which an individual neuron or a population of neurons can differentially respond to, is denoted the dynamic range (Fig. 1, see section 1.1.1). A canonical function of feedforward interneurons is thought to be increasing the dynamic range by scaling inhibition with input strength (Liu et al., 2011; Pouille et al., 2009; Silver, 2010). This is because feedforward interneurons are ideally suited to integrate information about the input strength from an upstream area and proportionally increase their inhibitory drive. The

result is horizontal scaling of the input-output curve and an increased dynamic range (Olsen et al., 2010; Silver, 2010). The dynamic range ultimately increases because the saturation of the population activation curve is shifted to higher input strengths. This phenomenon has been described for the behavior of individual neurons (Olsen et al., 2010), but also at the population level (Pouille et al., 2009). Notably, in the second case, the dynamic range of individual neurons did not change with input strength, illustrating the importance of population level investigations (Pouille et al., 2009). Feedforward interneurons often target the same subcellular compartments as the excitatory afferents they receive input from (Buzsáki, 1984), implying that input normalization can be performed independently for different input pathways.

#### 1.4.2 Tuning and Selection of Inputs and Outputs

A diverse set of functional inhibitory network motifs has been described, which contribute to the tuning or selection of inputs onto individual cells or groups of cells. This can be seen most directly in sensory cortices, where individual neurons are often found to preferentially respond to a specific stimulus. Furthermore, the spatial arrangement of cells with specific preferred stimuli is often topographic and repeated in consecutive neuronal populations. A fundamental inhibitory motif in this case is lateral inhibition between neurons with different preferred stimuli. It can be either feedforward or feedback. The effect is seen most directly during ongoing neuronal activity, as the acute removal of inhibition blurs or removes the selectivity of individual neurons to their preferred stimuli. Many demonstrations of this have been published, mainly for visual cortex (Adesnik et al., 2012; Liu et al., 2011; Sillito, 1975), but also for somatosensory (Mountcastle and Powel, 1959), olfactory (Olsen et al., 2010), and auditory cortices (Wehr and Zador, 2003). The mechanism by which lateral inhibition achieves tuning or selection of principal cells is competition between the principal cells with different preferred stimuli. A similar mechanism has been described in more complex, multisensory settings. Investigation of hippocampal place cell assemblies has suggested a direct involvement of interneurons in the competition between assemblies (Geisler et al., 2007; Maurer and McNaughton, 2007). Accordingly, lateral inhibition has been termed the fundamental mechanism for the selection of neuronal groups (Isaacson and Scanziani, 2011; Lee et al., 2014; Roux and Buzsáki, 2014; Wilson et al., 2012).

Another interesting motif dynamically shifts inhibition along the somato-dendritic axis during repetitive stimulation (Liu et al., 2014; Pothmann et al., 2014; Pouille and Scanziani, 2004; Stokes and Isaacson, 2010; Tan et al., 2008). It functions by oppositely changing the activation and/or output of perisomatically and distal dendritically inhibiting interneurons, during an input train. During the course of the train perisomatically inhibiting interneurons depress, while dendritically inhibiting interneurons facilitate, resulting in a dynamic shift of inhibition from soma to dendrites. Such a motif may subserve a number of different functions. Firstly, it can differentially modulate which afferent areas are allowed to transmit information to the cell as a function of time (Leão et al., 2012; Lovett-Barron et al., 2014). Secondly, it may define separate time windows for AP generation and dendritic plasticity. This is, because somatic inhibition is most effective at controlling AP initiation, while dendritic inhibition interferes primarily with dendritic electrogenesis and local dendritic synaptic plasticity (Chiu et al., 2013; Cichon and Gan, 2015; Cobb et al., 1995; Losonczy et al., 2008; Miles et al., 1996; Royer et al., 2012). For instance, dendritic disinhibition is necessary for associative fear learning in the auditory cortex (Letzkus et al., 2011) and amygdala (Li et al., 2013a). Since the various forms of plasticity are thought to be the bases of the long term formation of cell assemblies, the involvement of inhibition into neuronal group selection extends to the classical Hebbian sense (Buzsáki, 2010). Accordingly, inhibition is thought to underlie neuronal group selection in a two-fold way, firstly during ongoing activity through direct competition and AP suppression, and secondly in the sculpting of the synapse over longer time scales.

#### 1.4.3 Feedback Inhibition and Output Normalization

A large number of computational studies rely on a canonical microcircuit motif, which is thought to normalize the population level output, termed 'max pooling' (Carandini and Heeger, 2012). Briefly, max pooling refers to the measurement of the total activity level across the population, in order to produce a global adjustment of this activity level. This global adjustment will then suppress all activity, except for that of the cell(s) receiving maximum input. The expected result concerning the population level input-output curve is scaling along the output axis (Olsen et al., 2010; Silver, 2010). This function is frequently assumed to be implemented by feedback inhibition (Binas et al., 2014; Carandini and

Heeger, 2012; Rolls and Treves, 1998). A specific instance of this computation is a 'k-winners-take-all' network, in which the k cells with the highest input strengths are allowed to fire, while all others are suppressed (Binas et al., 2014; Myers and Scharfman, 2009; Rolls, 2010). Recent investigations in the drosophila olfactory system revealed a direct implementation of this motif by a globally inhibiting feedback interneuron (Lin et al., 2014; Papadopoulou et al., 2011). In accordance with long standing computational predictions, the inactivation of the global feedback inhibitory interneuron led to impaired odor discrimination. Due to the larger size of mammalian neural networks, it is unlikely that the max pooling operation is performed by a single inhibitory cell, as demonstrated in drosophila. However, the general mechanism is thought to act across species, in multiple neural systems (Busse et al., 2009; Carandini and Heeger, 2012; Renno-Costa et al., 2010) and be involved in a large number of computations (Binas et al., 2014). The advantage of feedback inhibition as a mechanism to implement a winner-take-all rule is that it receives information about the population activity level. In contrast to feedforward inhibition, it can respond as a function of the population activity level, while the former can respond only as a function of the input strength. Specifically, feedforward inhibition lacks the information of the activation curves resulting from intrinsic principal cell properties. Though it could be tuned to perform a k-winners-take-all function in a static network, for instance by evolutionary hard wiring, this task becomes highly challenging in a plastic network. The tuning of intrinsic principal cell properties is even less well suited to generate winner-take-all like activity, since it lacks a means to implement competition. Though plastic intrinsic properties of the population could also be tuned to arrive at the appropriate active cell fraction, individual cells do not have access to information about the input or output level of their neighbors. Accordingly, the use of feedforward inhibition or intrinsic properties to implement a max pooling operation would require additional assumptions about how the missing information is generated and communicated.

## 1.5 The Dentate Gyrus of the Hippocampal Formation

A region in which ‘max pooling’ is deemed of critical importance is the DG of the hippocampal formation, one of the best studied regions in the brain. Together with the DG, the hippocampus proper is part of the archicortex, which in contrast to neocortex has a clear three layered structure and contains only one principal cell layer. In rodents it forms a banana shaped structure stretching from the dorsomedial septal pole to the ventrolateral temporal pole. Beside the glutamatergic principal cells, all regions of the hippocampus contain a variety of different interneurons which are interconnected with the principal cells forming complicated microcircuits (Savanthrapadian et al., 2014; Somogyi and Klausberger, 2005). The hippocampus proper, also called the cornu ammonis (CA), can be subdivided into two main sections, namely the CA3 and CA1 area. Together with the DG, it forms the canonical trisynaptic circuit of the hippocampus. The DG receives information via the perforant path projection from the entorhinal cortex and conveys that information to the CA3 area. The CA3 area, which is characterized by pronounced recurrent connectivity, projects to the CA1 area which in turn feeds the information back to neocortical areas. The hippocampus is essential for the formation of episodic and contextual memories in humans as well as rodents (Kandel et al., 2000; Kheirbek et al., 2013; Scoville and Milner, 1957). Furthermore, it has been extensively studied as part of the brain system responsible for spatial navigation, since it contains cells which show location specific firing, so called ‘place cells’ (Moser et al., 2015; O’Keefe and Dostrovsky, 1971). A specific challenge in understanding its function is the inherently multisensory nature of the information it processes.

Substantial evidence points to the involvement of the DG in the function of ‘pattern separation’ (Bakker et al., 2008; Gilbert et al., 1998; Leutgeb et al., 2007; Neunuebel and Knierim, 2014; Rolls, 2013) and it has been associated with the misclassification deficits of schizophrenia (Das et al., 2014; Heckers and Konradi, 2015) as well as the memory deficits in Alzheimer’s disease (Palmer and Good, 2011). Moreover, it is thought to play a role in ‘regulating the input to the hippocampus’ thus potentially protecting against the spread of over-excitation observed in temporal lobe epilepsy (Goldberg and Coulter, 2013; Heinemann et al., 1992; Krook-Magnuson et al., 2015; Lothman et al., 1992). Accordingly, the dentate microcircuitry has been a prime target for investigations into the pathology of chronic

temporal lobe epilepsy, where it is found to undergo substantial anatomical and physiological changes (Coulter, 2000; Hunt et al., 2011; Nadler et al., 1980; Peng et al., 2013; Ratzliff et al., 2004; Wright and Jackson, 2014; Zhang et al., 2009). Interestingly, the ‘dentate gate’ appears to be only transiently impaired during epileptogenesis, suggesting that the observed changes are at least partially compensatory (Ang et al., 2006; Krook-Magnuson et al., 2015; Wozny et al., 2005). In this chapter I will briefly outline the anatomical organization and function of the rodent DG, with a special section on the hilar microcircuit.

### 1.5.1 Anatomy and Physiology of the Dentate Gyrus

The DG is bent around the end of the CA3 region of the hippocampus proper in a ‘V’ or ‘U’ shape (Amaral et al., 2007). The two blades are denoted the superior and inferior blade, where the superior blade is surrounded by the downstream regions of the hippocampus proper. The glutamatergic principal cells of the DG are the granule cells (GCs), which form the tightly packed dentate GC layer, in the center of the three layered structure. An important feature of the DG is that it contains approximately ten-fold more principal cells than the entorhinal cortex and five-fold more cells than the CA3 region (Schmidt et al., 2012). GCs have several long, spiny dendrites which emanate in a cone-like manner from the soma, and span the molecular layer (ML) pointing away from CA3 (Claiborne et al., 1990). They receive multisensory input, mainly from the entorhinal cortex via the perforant path. On the other side of the GC layer, GCs emit their axons, the mossy fibers, which converge within the hilus, also called the polymorphic layer, to form a dense bundle which then runs alongside and innervates the principal cells of the CA3 region. The mossy fibers run strictly perpendicular to the septo-temporal axis of the hippocampus defining the transverse, lamellar or maximum connectivity plane (MCP; Amaral et al., 2007; Andersen et al., 1971; Bischofberger et al., 2006). Mossy fibers physiologically innervate local interneurons and downstream CA3 cells but not other GCs. This is reflected in the anatomical spread of mossy fiber collaterals which spread profusely within the polymorphic layer but never enter the ML where GC dendrites are located. The lack of recurrent excitatory connections between principal cells is unique to the DG, and makes it ideally suited for a quantitative investigation of the feedback inhibitory circuit. *In vivo*, GCs are characterized by extremely sparse firing (Alme et al., 2010; Leutgeb et al., 2007). They have a strongly hyperpolarized resting

membrane potential of less than -80 mV and a comparably high AP threshold at -49 mV (Staley et al., 1992). Furthermore their dendrites have distinct electrophysiological properties including strong voltage attenuation and linearized summation of inputs (Krueppel et al., 2011).

Finally, an important particularity of the DG is that it is one of the few regions displaying adult neurogenesis. Adult born, immature GCs display a transient period of markedly greater excitability and plasticity than mature GCs (Espósito et al., 2005; Ge et al., 2007). During this critical developmental period immature GCs come to respond to significant features of their environments (Kee et al., 2007; Tashiro et al., 2007) and are characterized by a much higher and less selective firing rate than mature GCs.

### 1.5.2 Microcircuitry of the Dentate Gyrus

Interspersed into all three layers of the DG are numerous interneurons which are innervated by perforant path (feedforward), mossy fibers (feedback), or both (Hsu et al., 2015; Li et al., 2013b). Notably, mossy fibers synapse onto up to ten times more GABAergic than glutamatergic cells by means of a distinct set of collaterals in the polymorphic layer, indicating a potent feedback inhibitory pathway (Acsády et al., 1998). When GABA is released from these cells, it inhibits GC activity via shunting, rather than hyperpolarization, due to the low GC resting potential (Chiang et al., 2012; Staley and Mody, 1992). Additionally, GCs *in vitro* display a high tonic GABAergic conductance due to GABA spillover from synaptic into extra synaptic sites, contributing to their lack of excitability (Nusser and Mody, 2002). In the DG there are at least five types of GABAergic interneurons (Amaral, 1978; Halasy and Somogyi, 1993; Han et al., 1993; Hosp et al., 2014; Lorente De Nó, 1934; Mott et al., 1997; Sik et al., 1997).

The most intensively studied DG interneuron is the fast spiking, PV<sup>+</sup> pyramidal BC which is typically situated at the edges of the GC layer and provides potent perisomatic inhibition to GCs via its basket like axonal plexuses (Amaral et al., 2007; Bartos et al., 2002). It mediates feedforward (Zipp et al., 1989) as well as feedback inhibition (Acsády et al., 1998; Geiger et al., 1997) and is characterized by extremely fast response characteristics and a high maximal AP frequency (Geiger et al., 1997). Another prominent interneuron, which is often

considered a classical feedback interneuron, is the SST<sup>+</sup> hilar perforant path associated interneuron (HIPP; Han et al., 1993; Hosp et al., 2014; Katona et al., 1999). It receives its inputs from GCs and projects to the distal dendrites of GCs together with the perforant path. A third major type of DG interneuron is the CCK<sup>+</sup> hilar commissural/associational path related cell (HICAP), which innervates the inner third of the ML. Beyond these, there appear to be additional types of DG interneurons which have not yet been well described (Amaral et al., 2007; Hosp et al., 2014; Liu et al., 2014). Beside these GABAergic interneurons the hilus contains one type of glutamatergic interneuron, the mossy cell (Amaral, 1978). Mossy cells received their name because their proximal dendrites are covered by large thorny excrescences which are the termination sites of mossy fiber inputs (Amaral, 1978). They give rise to the commissural/associational path, an excitatory tract innervating the inner third of the ML in the ipsi- as well as the contralateral hemisphere, where they synapse on GC as well as interneuron dendrites (Scharfman, 1995).

Importantly, these different interneurons (including mossy cells) also innervate each other forming complex networks (Larimer and Strowbridge, 2008; Savanthrapadian et al., 2014). In a detailed study Savanthrapadian et al. (2014) report inhibitory interactions between HICAP cells as well as between HIPP cells. Moreover, both cell types inhibit BCs while BCs and HICAP cells rarely target HIPP cells. The time course and reliability of inhibition is defined by the identities of both the presynaptic and the postsynaptic cell (Savanthrapadian et al., 2014). Mossy cells also receive input from, and project to, hilar interneurons (Larimer and Strowbridge, 2008). Additionally, interneuron- interneuron synapses show cell type specific short term dynamics during trains of activity ranging from facilitation at HICAP-HICAP, biphasic modulation at HIPP-HIPP to depression at BC-BC synapses (Savanthrapadian et al., 2014). Finally, different interneurons display different synaptic properties at their output synapse onto GCs concerning the latency, jitter, amplitude, failure rate and short term plasticity (Harney and Jones, 2002; Liu et al., 2014). It should be noted, that while the functional studies cited above have almost exclusively addressed the local connectivity of an acute slice preparation, there is also pronounced translamellar connectivity, most prominently by HIPP and mossy cells (Amaral et al., 2007).

In view of these complex connections, it is questionable whether the recruitment of feedback inhibition at a population level can be investigated by probing the behavior of

individual interneuron types. However, the ultimately relevant output of the complex interactions within the feedback inhibitory microcircuitry is the inhibition elicited in GCs, which can be readily recorded. In the following chapter I will review the concept of pattern separation in the DG from a historic perspective with a special section on the putative role of feedback inhibition. This will lead directly to the key questions and approach of the present study (chapter 1.7).

## 1.6 Pattern Separation in the Dentate Gyrus

As introduced in section 1.1.3, pattern separation refers to the reduction of correlation between two population representations from one brain area to the next. It is thought to be a recurring phenomenon throughout the brain but has received particular interest in the DG (Aimone et al., 2011). The term pattern separation is often used somewhat ambiguously for phenomena at different levels, namely algorithmically (as originally defined), physiologically, and behaviorally (Santoro, 2013). Specifically, it is important to distinguish the term pattern discrimination, which refers to patterns within one population, from the term of pattern separation, which refers to the decrease of correlation between two patterns from one population to the next. Although it is prudent to remain aware of the different nature of these levels and definitions, their conflation ultimately represents the attempt to understand how physiological systems implement algorithms in order to bring forth behavior. This is best understood by briefly reviewing the history of the theory of pattern separation. The theory originally arose from computational neuroscience (Aimone et al., 2011). In 1971, David Marr proposed his highly influential ‘theory for archicortex’. It stated that the CA3 region of the hippocampus may function as an autoassociation or attractor network, ideal for forming memory representations, because it displayed such pronounced recurrent connectivity (Marr, 1971). Subsequent work on attractor networks showed, that they are highly prone to destructive interference, and that their capacity can be dramatically increased if their input, during the encoding phase, is orthogonal (Amit et al., 1987; Hopfield, 1982; see also section 1.1.3). Due to its sparse projection to CA3 and large cell population the DG seemed ideally suited for the task of providing decorrelated input (McNaughton and Morris, 1987; Treves and Rolls, 1992). It was the confirmation of several predictions which

this theory ‘pattern separation’ made, that ‘solidified a general consensus in the community’ (Aimone et al., 2011). Firstly, the discharge of very few GCs should efficiently activate CA3 cells (Henze et al., 2002). Secondly, the GC population should be characterized by extremely sparse firing, possibly being under strong inhibitory control (Nitz and McNaughton, 2004). Thirdly, the DG should play an important role during memory encoding rather than during recall (Kheirbek et al., 2013; Lee and Kesner, 2004). Fourth, the cellular activity patterns in DG should display some form of decorrelation (Leutgeb et al., 2007; Neunuebel and Knierim, 2014; Schmidt et al., 2012). And finally, the DG should play a role during behavioral discrimination tasks (Bakker et al., 2008; Das et al., 2014; Gilbert et al., 2001; McHugh et al., 2007). In addition there is evidence that adult neurogenesis, a defining trait of the DG, plays an important role in pattern separation (Clelland et al., 2009; Sahay et al., 2011).

While this confluence of evidence has led to a general consensus as to the validity of the general concept of pattern separation in the DG, it is important to keep in mind that the large majority of the studies actually address discrimination within individual populations or at a behavioral level rather than the process of pattern separation as originally defined computationally (Santoro, 2013; but see Neunuebel and Knierim, 2014).

### 1.6.1 The Proposed Role of Feedback Inhibition in Pattern Separation

As a result of these theoretical considerations and empirical findings the feedback inhibitory microcircuitry is deemed of critical importance for DG processing (Ewell and Jones, 2010; Faghihi and Moustafa, 2015; Jinde et al., 2012; Nitz and McNaughton, 2004; Sambandan et al., 2010; Temprana et al., 2015). It has been assumed to serve two functions in particular: ‘max pooling’ contributing to sparse firing and ‘neuronal group selection’ leading to additional pattern orthogonalization.

Most computational studies have explicitly or implicitly assumed feedback inhibition to implement variations of the k-winners-take-all rule in the DG (de Almeida et al., 2009; Myers and Scharfman, 2009; O’Reilly and McClelland, 1994; Petrantonakis and Poirazi, 2015; Rolls and Treves, 1998). The sparsification of individual representations is in itself already likely to lead to pattern orthogonalization in the sense of a reduced overlap as detailed in section 1.1.2. Separate from this purely statistical orthogonalization it is possible that active

mechanisms of decorrelation exist. Again, feedback inhibition has been the primary suspect due to its ability to implement active competition between assemblies of principal cells, thereby implementing neuronal group selection (Buzsáki, 2010; Roux and Buzsáki, 2014).

As detailed above, the feedback inhibitory microcircuit is highly complex. However, the relevant parameter at the population level is the inhibition ultimately delivered to dentate GCs. Consequently, this study treats the feedback inhibitory microcircuitry as a black box, considering only the net output arriving at the GC population. Note that the function of immature GC in the learning of discriminable patterns has been proposed to rely on the lack of a proper integration into the feedback inhibitory circuit (Aimone et al., 2011; Temprana et al., 2014; see also chapter 4.7). Accordingly, this study concentrates on the mature GC population.

## 1.7 Key Questions

Although decades of computational models have relied on feedback inhibition to implement important computational functions such as max pooling and neuronal group selection, the underlying microcircuit is poorly understood. To arrive at a better understanding of how feedback inhibition may contribute to these functions requires a quantitative characterization of the recruitment of feedback inhibition from the population perspective. Firstly, what is the dynamic range of the feedback inhibitory circuit? Secondly, what is the gain of the circuit and how does this gain develop as more cells are activated? In order to answer these questions it is furthermore necessary to understand how feedback inhibition is organized in space and time. Specifically, how are the cells receiving inhibition from a given GC population distributed in space and what is the time course of this inhibition. Finally, how does inhibition behave during trains of GC activity? Although these questions are overtly important in the DG of the hippocampal formation, the underlying network motif is likely to play an important role throughout the brain.

## 2. Materials and Methods

### 2.1 Animals and Slice Preparation

All animals were treated according to the University of Bonn Animal Experiment Guideline, minimizing unnecessary pain and discomfort. Experiments were performed on horizontal hippocampal slices of 21 to 97 day old mice.  $\text{Ca}^{2+}$  imaging and some dual recording experiments were performed in C57/Bl6 mice obtained from Charles River Laboratories (Wilmington, Massachusetts, USA). Optogenetic experiments were performed on double transgenic offspring of Tg(Prox1-cre)SJ39Gsat/Mmucd) obtained from MMRRC UC Davis as cryopreserved sperm and rederived in the local facility (Gong et al., 2003, 2007) and Ai32-mice (B6;129S-Gt(ROSA)26Sor<sup>tm32(CAG-COP4\*H134R/EYFP)Hze</sup>/J, Jackson Laboratory, Bar Harbor, USA). For preparation the animals were deeply anesthetized with Isoflurane (Abbott Laboratories, Abbot Park, USA) and then decapitated. The head was instantaneously submerged in ice-cold carbogen saturated artificial cerebrospinal fluid (containing in mM: NaCl, 60; sucrose, 100; KCl, 2.5;  $\text{NaH}_2\text{PO}_4$ , 1.25;  $\text{NaHCO}_3$ , 26;  $\text{CaCl}_2$ , 1;  $\text{MgCl}_2$ , 5; glucose, 20) and the brain removed.

### 2.2 Obtaining Maximum Connectivity Plane Sections

Horizontal 350  $\mu\text{m}$  thick slices were cut with a vibratome (VT1200 S, Leica, Wetzlar, Germany). The brain was glued to the to the slicing chamber on its dorsal surface, such that slices will be parallel to the dorsal brain surface (compare Bischofberger et al., 2006). To obtain slices of the MCP the slicing depth at which the temporal pole of the hippocampus first became visible was noted (depth = 0  $\mu\text{m}$ ). From here the first four sections were discarded (up to a depth of 1400  $\mu\text{m}$ ). The following two to three sections were secured such that one further section before the beginning of the dorsal hippocampus (approximately 2400  $\mu\text{m}$ ) could be discarded. The beginning of the dorsal hippocampus, identified by its oval shape and oblique orientation towards the midline, served as an additional control for the anatomical position. Slices were then incubated at 35 °C for 20 to 40 minutes. Afterwards, slices were stored in normal ACSF (containing in mM: NaCl, 125; KCl, 3.5;  $\text{NaH}_2\text{PO}_4$ , 1.25;  $\text{NaHCO}_3$ , 26;  $\text{CaCl}_2$ , 2.0;  $\text{MgCl}_2$ , 2.0; glucose, 15) at room temperature for up to 6 hours. For

the experiments slices were transferred into a submerged recording chamber at 35 °C under constant superfusion with normal ACSF (approximately 3 ml/min). Experiments were performed in the superior blade unless otherwise indicated. All experiments were conducted in accordance with the guidelines of the Animal Care and Use Committee of the University of Bonn.

### 2.3 Electrophysiological Recordings

Hippocampal dentate GCs were visually identified using infrared oblique illumination contrast microscopy in a 20x or 60x water immersion objective (Olympus, XLumPlanFI, NA0.95W or Nikon, N60X-NIR Apo, NA1.0W) on an upright microscope (TriMScope®, LaVision Biotech, Bielefeld, Germany or Nikon Eclipse FN1, Tokyo, Japan). For voltage clamp measurements the whole-cell patch-clamp configuration was established with a low chloride cesium-methane-sulfonate based intracellular solution (intracellular solution containing in mM: CH<sub>3</sub>O<sub>3</sub>SCs, 140; 4-(2-hydroxyethyl)-1-piperazineethanesulfonic acid (HEPES-acid), 5; ethylene glycol tetraacetic acid (EGTA), 0.16; MgCl<sub>2</sub>, 0.5; sodium phosphocreatine, 5; glucose, 10). For current clamp experiments a low chloride solution (CC-intracellular solution containing in mM: K-gluconate, 140; 4-(2-hydroxyethyl)-1-piperazineethanesulfonic acid (HEPES-acid), 5; ethylene glycol tetraacetic acid (EGTA), 0.16; MgCl<sub>2</sub>, 0.5; sodium phosphocreatine, 5) was used. Cell-attached recordings were performed with normal ACSF or in some cases with VC-intracellular solution. The calculated Cl<sup>-</sup>-equilibrium potential with low Cl<sup>-</sup> intracellular solution is given by the Nernst equation (Eq. 2),

$$\text{Equation 2} \quad V_{Cl^-} = \frac{R \times T}{-F} \ln \left( \frac{[Cl^-]_{ex}}{[Cl^-]_{in}} \right) = -130.5 \text{ mV}$$

where R is the universal gas constant ( $R = 8.314 \text{ J K}^{-1} \text{ mol}^{-1}$ ), T is the absolute temperature ( $T = 308.5 \text{ K}$ ), F is the Faraday constant ( $F = 9.649 \times 10^4 \text{ C mol}^{-1}$ ),  $[Cl^-]_{ex}$  is the extracellular Cl<sup>-</sup> concentration ( $[Cl^-]_{ex} = 136.5 \text{ mM}$ ), and  $[Cl^-]_{in}$  is the intracellular Cl<sup>-</sup> concentration ( $[Cl^-]_{in} = 1 \text{ mM}$ ). For voltage clamp experiments the intracellular solution was additionally K<sup>+</sup>-free in order to allow stable recording at 0 mV further increasing the Cl<sup>-</sup> driving force as well as minimizing cation-mediated currents. The electrochemical driving force for Cl<sup>-</sup> under these conditions is given by (Eq. 3),

Equation 3  $V_{DF} = V_m - V_{Cl^-} = 130.5 \text{ mV}$

where  $V_{DF}$  is the  $Cl^-$  driving force and  $V_m$  is the membrane potential at which the cell is held ( $V_m = V_h = 0 \text{ mV}$ ). The high resulting  $Cl^-$  driving force produces large  $Cl^-$  mediated outward currents with good signal to noise ratio. The input resistance was measured in voltage clamp with a 25 ms, -5 mV pulse. Cells with input resistances greater than 300 M $\Omega$  were discarded in order to exclude immature GCs (Schmidt-Hieber et al., 2004). In all imaging experiments and a subset of optogenetic experiments the intracellular solution additionally contained 100  $\mu$ M Alexa 594 hydrazide sodium salt (Life Technologies, Carlsbad, USA). The identity of visually and electrophysiologically identified mature GC was confirmed by their dendritic morphology after dye filling in every case tested. Patch pipettes were made from borosilicate glass capillaries (GB150F-8P, Science Products) with a horizontal puller (P-97, Sutter Instruments, Novato, USA or Zeitz DMZ, Zeitz-Instruments, München, Germany). Pipette resistance of the patch pipettes was 3 – 7 M $\Omega$ .

Voltage-clamp recordings were performed with a Multiclamp 700B (Molecular Devices, Sunnyvale, USA) or a BVC-700A amplifier (Dagan Corporation, Minneapolis, USA). Current-clamp recordings were performed with a Multiclamp 700B. Series resistance was compensated for both CC and VC (8 – 30 M $\Omega$ ). Voltage or current signals were digitized with a Digidata 1322A (Molecular Devices) or (Instrutech ITC-16, Heka Electronics, Ludwigshafen, Germany) at 10 to 50 kHz and recorded using Clampex 10.2 (Molecular Devices) or Igor Pro 6 (Wavemetrics, Lake Oswego, USA) on a PC running Windows XP. For IPSC measurements cells were held at 0 mV including liquid-junction potential correction (16 mV). The liquid junction potential for VC recordings was calculated using the Clampex Junction Potential Calculator. For CC-recordings liquid junction potential was not corrected. The IPSC input-output relationships were only used if they showed saturation. For further analysis they were then normalized to the maximally elicited IPSC for the respective cell. Note, that due to this normalization all normalized IPSC values are by definition below 100 %. All chemicals for electrophysiological experiments were obtained from Sigma-Aldrich (St. Louis, USA).

## 2.4 Pharmacology

All experiments were performed in the presence of 0.5  $\mu\text{M}$  CGP (CGP 52432) to block GABA<sub>B</sub> receptors. To exclude direct electrical activation of interneurons during Ca<sup>2+</sup> imaging experiments, 25  $\mu\text{M}$  6-cyano-7-nitroquinoxaline-2,3-dione (CNQX) + 50  $\mu\text{M}$  D-2-amino-5-phosphonovalerate (D-APV) was bath applied at the end of each experiment. DCG-IV (0.5  $\mu\text{M}$ ) and Gabazine (SR 95531 hydrobromide, 10  $\mu\text{M}$ ) were also bath applied. For optogenetic experiments 40  $\mu\text{M}$  CNQX + 50  $\mu\text{M}$  D-APV was used. All drugs were purchased from Tocris Bioscience (Bristol, UK).

## 2.5 Dual Patch Experiments

Two GCs within 100  $\mu\text{m}$  of each other were recorded. To test for single GCs induced feedback inhibition 10 to 15 trains of 10 APs at 100 Hz were elicited by brief (3 ms) current injections in one cell. To monitor inhibition in the other cell it was either injected with a positive current such that its membrane potential was approximately -60 mV (for dual CC-recordings) or held at 0 mV as described above (for VC-recordings, section 2.3). The resulting traces were averaged in order to be able to detect even minute IPSCs or IPSPs. This was necessary due to the high level of spontaneous activity in MCP slices.

## 2.6 Ca<sup>2+</sup> Imaging

Dye loading was modified from (Garaschuk et al., 2006) and performed in the submerged chamber at 35°C under constant superfusion. A high affinity Ca<sup>2+</sup> dye Oregon Green<sup>®</sup> 488 BAPTA-1 acetoxymethyl ester (OGB-1 AM, 50 $\mu\text{g}$ ) was dissolved in 4.5  $\mu\text{l}$  20 % pluronic F-127 in DMSO (both Life Technologies, Carlsbad, USA) by 10 to 15 min of vortexing. The resulting stock was diluted 1:10 with simplified Ca<sup>2+</sup>-free Ringer's solution (containing in mM: NaCl, 150; KCl, 2.5; HEPES, 10) to yield a dye concentration of approximately 0.9 mM. Before use, the staining solution was filtered with 0.45  $\mu\text{m}$  pore diameter (Merck Millipore, Darmstadt, Germany). Approximately 5  $\mu\text{l}$  was filled into a standard patch pipette with a resistance of 3 – 7 M $\Omega$ . The dye was then injected into the slice at 4 to 5 locations along the superior blade

of the granule cell layer at 100  $\mu\text{m}$  intervals. Each bolus was injected  $\sim 30 \mu\text{m}$  below the slice surface for 3 minutes at 500 mbar. Upon application of the dye in this manner, the lipophilic OGB-1 AM is taken up through the cell membranes. Intracellularly the acetoxy-methyl group is cleaved by unspecific esterases rendering the dye hydrophilic and thus trapped inside the cytoplasm. Recordings were started at least 45 minutes after the staining procedure when a sufficient amount of dye had accumulated inside the cells. Comparison with cells, filled with known concentrations of OGB-1 through a patch pipette, indicate the dye concentration achieved by bolus loading was in the range of 50 to 100  $\mu\text{M}$ .

Population  $\text{Ca}^{2+}$  Imaging was performed using a multibeam two-photon fluorescence microscope (TriMScope<sup>®</sup>, LaVision Biotech, Bielefeld, Germany). This system is based on a beam splitter that separates the incoming femtosecond laser beam (provided by a Ti:Sapphire laser, Chameleon Ultra, Coherent, Santa Clara, USA; excitation wavelength tuned to 810 nm) into 64 beams, which are scanned simultaneously through the slice. This allowed imaging of a large field of view (320 x 240  $\mu\text{m}$ ) with high spatial and temporal resolution (1920 x 1440 pixels, 20 Hz) as well as sufficiently low signal to noise ratios for the detection of single AP induced  $\text{Ca}^{2+}$  transients (see section 3.1.1). Images were acquired with a digital CMOS camera (ORCA-Flash, Hamamatsu) through a high numerical aperture 20x water immersion Objective (XLumPlanFI, NA-0.95, Olympus).

Time series were processed with ImageJ 1.48o and IGOR Pro 6.3 in a semiautomatic manner. To correct for movement artifacts and drift, time series were first registered. Regions of interest were then manually placed onto all well loaded cells in an average projection of the series. Individual cellular fluorescence over time traces were extracted and further processed with IGOR Pro software.  $\text{Ca}^{2+}$  fluorescence increase normalized to baseline ( $\Delta F/F$ ) traces of individual cells were calculated without background subtraction. The fraction of responders for each time series was extracted by automatic thresholding. The threshold was determined by combined cell-attached and  $\text{Ca}^{2+}$  imaging experiments (section 3.1.1). Note, that for these experiments the stimulation electrode was placed into the hilus in order to obtain a sufficient number of true positive responders. Responders and non-responders were further confirmed visually. The imaged cell population comprised on average  $46 \pm 18$  (standard deviation) cells ( $n = 23$  slices). The active cell fraction corresponds to the fraction of responders normalized to the dye loaded population within each section.

To assess the spatial distribution of cell activation in imaging experiments,  $\Delta F/F$  projections were created by averaging and smoothing four frames during the transient and four frames at baseline fluorescence and then calculating the pixel wise  $\Delta F/F$ .

## 2.7 Electrical Stimulation

To electrically elicit feedback inhibition a bipolar cluster microelectrode (FHC, Bowdoin, USA) connected to a digital stimulus isolator (AM-systems, Sequim, USA) was placed into stratum lucidum in the CA3 region. Stimuli between 50 and 500  $\mu\text{A}$  were applied for 0.1 ms in a randomized fashion in order not to mistake decreasing stimulus efficiency at increasing power with IPSC saturation. IPSCs at individual powers were elicited 5 to 13 times at 0.1 Hz and averaged. The stimulus isolator was constantly monitored to ascertain that the applied current could be passed by the electrode. This was sometimes not the case for currents between 300 and 500  $\mu\text{A}$  leading to missing data points for these powers. In order to sever CA3 backprojections in a subset of experiments two cuts were made along the hilar border sparing only the mossy fiber tract. Only experiments in which a complete block of inhibition by glutamatergic blockers could be demonstrated were considered for the analysis of feedback inhibition (8 of 23, see section 2.4).

## 2.8 Calculation of the Recruitment of Feedback Inhibition for Imaging Experiments

In order to obtain the input-output relationships of the feedback inhibitory circuit the GC activation (input) was related to the GC inhibition (output). To this end data concerning each variable was averaged over slices by power. This was necessary since only a small subset of experiments in which inhibition was completely blocked could also be successfully imaged (6 of 8 sections). Due to the small numbers of active cells throughout the entire dataset with sufficient dye loading ( $n = 23$ ) analysis of only these 6 slices leads to a very piecemeal recruitment curve. A more accurate estimation of the recruitment of feedback inhibition can be obtained by averaging the cell activation and inhibition over all respectively appropriate slices and relating them by power. Note, that while the fraction of activated cells in non-MCP

sections (not included in the quantitative analysis) was mostly zero (in 7/8 sections; single cell in 8<sup>th</sup> section), IPSCs were almost always present (in 28 of 29 cells in non-MCP sections which were not included in analysis). In other words, the exclusion of non-MCP sections represents a bias towards larger cell fractions.

## 2.9 Optogenetic Stimulation

Optogenetic experiments were performed on double transgenic mice conditionally expressing of ChR(H134R)-eYFP in dentate GCs (Prox1-ChR-eYFP mice, (Gong et al., 2003, 2007; see also Allen Mouse Brain Atlas, Lein et al., 2007). Focal stimulation was achieved through a galvanometer driven spot illumination device coupled to a 473 nm DPSS Laser (UGA-40, DL-473, Rapp Optoelectronics, Hamburg, Germany) on an upright microscope (Nikon Eclipse FN1, Tokyo, Japan). The FWHM of the resulting stimulation spot at the focal plane was  $8.36 \pm 0.04 \mu\text{m}$  (Nikon 10X Plan Fluor, NA 0.3). It was measured by rendering the laser spot on a chrome plate and fitting the resulting intensity profile with a Gaussian. Laser powers are given in arbitrary units from 1 to 7 corresponding to  $15 \pm 1 \mu\text{W}$ ,  $107 \pm 14 \mu\text{W}$ ,  $292 \pm 42 \mu\text{W}$ ,  $762 \pm 105 \mu\text{W}$ ,  $1433 \pm 49 \mu\text{W}$ ,  $1729 \pm 165 \mu\text{W}$  and  $1660 \pm 163 \mu\text{W}$  measured at the objective ( $n = 5$  measurements spread over several months). Individual illumination spots were placed at approximately  $40 \mu\text{m}$  into the ML at the slice surface thereby activating the dendrites of several juxtaposed GC. Stimulation pulses were of 20 ms duration.

## 2.10 Measurement of the Fluorescence Intensity Profile

To measure the fluorescence intensity profile throughout a slice the setup was modified to be able to image the slice from below while the laser beam was focused to its surface. This was achieved by focusing a Surgical Microscope with 36x magnification (M695, Leica Microsystems, Wetzlar, Germany) to the lower slice surface. Images were taken with a CCD camera (Nikon D60, 0.25 ms exposure, no gain). A neutral density filter (ND4) was introduced into the light path in order to avoid saturation. Acute sections of 100, 150, 200, 250, 300 and 350  $\mu\text{m}$  thickness were cut from Prox1-ChR-eYFP mice as described above. The laser was focused to the surface of in the hilus and an image taken at every laser power ( $P =$

1 to 7 AU). The stage was moved for every image to avoid bleaching or phototoxicity. The two-dimensional profiles of individual slices were roughly isometric. Therefore linear profiles were measured in several directions and averaged to obtain a single x profile per section. The x-profiles of slices of different thickness were then stacked to obtain the xz-profile. Values below 100  $\mu\text{m}$  depth were obtained through fitting a Gaussian function in x-direction at 100  $\mu\text{m}$  depth and an exponential function in z-direction. Complete three-dimensional intensity profiles of three different locations of two slices within the dentate molecular layer were averaged.

## 2.11 Calculation of the Optogenetically Activated Cell Fraction

To assess the active fraction of GCs individual cells were recorded in cell-attached mode and illumination spots were placed along the GC layer at 100  $\mu\text{m}$  intervals, all approximately 40  $\mu\text{m}$  into the ML. The entire profile was then probed in triplicate with 1 s intervals between individual locations. When the stimulation spot was in sufficient proximity to the recorded cell clear APs were generally visible (in 25 of 26 cells). The non-responding cell was pre-depolarized via the cell-attached pipette and stimulated with very high powers to confirm its general ability to spike in response to light stimulation. For stimulation, the focal plane was set to the depth at the middle between the highest and lowest point of the slice surface. This was generally not the plane of the recorded cell. The dependence of the IPSC and cell spiking on focusing 50  $\mu\text{m}$  above or below the slice was tested and no differences were observed ( $n = 6$ , not shown). Cell-attached spikes were detected by automatic thresholding at 6x standard deviation of the baseline. The spatial profile of firing probabilities, centered on the recorded cells, was averaged within each section. Probability distributions for sections were then averaged to obtain the overall firing probability distribution as a function of the x – distance for each power ( $n = 14$  cells). To test if cell activation properties differed between blades the maximum firing probabilities (at  $P = 7$ ) as well as the slopes (increase in firing probability from  $P = 1$  to 7) when simply averaging over all location of a given cell were compared by t-test ( $p = 0.490$  and  $0.684$  respectively). Since no difference was observed a single firing probability distribution was calculated for all cells.

Importantly, the decay of the firing probability with increasing distance from the light focus depends on both, the decay of the light intensity and the spread of the dendritic trees of GCs. In order to calculate the firing probabilities throughout the slice, the firing probability distribution at the surface was correlated to the light intensity distribution at a given power. This was done by calculating the firing probability distribution as a function of the 'virtual distance'. The virtual distance is given by the intensity weighted mean distance from a given pixel to all other pixels of the light intensity profile at a given power. It therefore incorporates the distances from an individual cell to all illuminated pixels weighted by the intensity within those pixels. Assigning the firing probabilities of pixels in the top row to their respective virtual distance yields the firing probability distribution as a function of virtual distance. It can now be used to also calculate the firing probabilities of pixels deeper in the slice using the measured light intensity distribution as input. The active cell fraction then corresponds simply to the mean firing probability throughout the slice. This calculation is independent of the size and number of GC. The procedure was performed for every power individually. For comparison the active cell fraction was also computed with alternative assumptions about the decay of the firing probability with increasing slice depth. If no firing probability decay with increasing depth is assumed, the active cell fraction throughout the slice is given simply by the average of the measured firing probabilities at the slice surface. Alternatively, the firing probability decay with depth was assumed to be identical to the measured decay along the slice surface (isometric firing probability distribution). In this case, Gaussian functions were fit to the probability distributions at the surface and these Gaussian functions were then assumed to extend also in the z-dimension. This approach assumes that the firing probability distribution in x and z is dependent mainly on the dendritic arbor while the light intensity distribution is negligible. The active cell fraction was then calculated by numerical integration under the two dimensional Gaussian (with the bounds from 0 to 350  $\mu\text{m}$  in z and -888 to 888  $\mu\text{m}$  in x, which corresponds to the mean GC layer length) normalized to the same area with a uniform firing probability of 1.

Finally, the given cell fractions were corrected by a factor reflecting the fact that a large portion of spikes occurred later than the mean IPSC. This factor was calculated simply as the number of spikes preceding the mean IPSC for each power and fitting the resulting relation with an exponential function. Note that this does not take account of the disynaptic delay between mossy fiber output and interneuron input.

## 2.12 Comparison of Focal and Global Activation

To globally activate the GC population a multimode light fiber (BF-22, Thorlabs, New Jersey, USA) coupled to a 473 nm laser (Omicron Phoxx, Rodgau-Dudenhofen, Germany) was placed above the slice surface, non-specifically illuminating the entire hippocampus. Analogous to focal stimulations, the activated cell fraction was calculated as the firing probability of individual cells following 20 ms pulses. Here no spatial normalization is necessary since cells were sampled from random locations with respect to the light fiber. Firing probabilities for the focal stimulation in these sections was calculated as the simple average of all stimulation locations, corresponding to the assumption of no firing probability decay with depth. The laser power for global stimulation was measured at the fiber end.

## 2.13 Spatial Distribution of Feedback Inhibition

The same stimulation paradigm which was used to assess cell activation was used to assess the spatial distribution of feedback inhibition. For individual cells, IPSCs at each location and power were averaged. The entire profile was then normalized to the largest measured IPSC of that cell, independent of the power and stimulation location at which it occurred. GCs were measured at various positions within the superior and inferior blades of the DG. For analysis, all IPSC profiles were spatially aligned to the recorded cells. The mean distance to apex  $\pm$  one standard deviation was  $356 \pm 163 \mu\text{m}$  and  $322 \pm 97 \mu\text{m}$  for superior and inferior cells respectively ( $n = 8, 8$  cells). In order to test whether there were any distinct effects of the apex, such as a steep decay of inhibition, which would be masked by alignment to the recorded cells, I also aligned the profiles to the apex (not shown). However, no such effects were visible. To analyze the saturated IPSC profiles, normalized IPSC amplitudes from  $P = 5$  to 7 were averaged for each cell. In order to analyze the effects of local versus remote stimulation for each blade a distance was chosen such that each remote location was still within the DG but always in the other blade ( $800 \mu\text{m}$  from the recorded cell). Normalized IPSCs of the three locations surrounding the recorded cell or this remote location were averaged within each power to obtain the IPSC amplitudes for further analysis. The cell fraction required for the activation of a half maximal IPSC in each section was assessed for each cell by linear interpolation between the measured values.

GCs of both blades were pooled to analyze the kinetic properties of IPSCs in order to gain power. All parameters were calculated on the multiple trials of individual cells. The latency was measured as the time from the beginning of the pulse to when the IPSC superseded 6 fold standard deviation of the baseline. The jitter was calculated as the standard deviation of these latencies for individual cells. The rise time was calculated as the mean 20 to 80 rise time of each cell and the decay time was obtained from an exponential fit to the decaying phase of the IPSC and corresponds to the fit-parameter tau.

## 2.14 Frequency Dependence of Feedback Inhibition

The frequency dependence of inhibition was tested optogenetically with 20 ms pulses at powers below saturation (usually  $P = 2$  for local inhibition and  $P = 3$  for remote inhibition). For each power and frequency five repeats were recorded and averaged. The peak amplitude between 15 and 35 ms following stimulus beginning was extracted and normalized to the first IPSC in a train. For comparison of the different stimulation frequencies the mean of the last three stimuli normalized to the first was calculated at each frequency. AP probabilities were assessed by cell-attached recordings with the stimulation site close to the recorded cell. Cell-attached spikes were detected by automatic thresholding as above during the exact time window of the pulse for each pulse (0 to 20 ms).

Antidromic electrical stimulation was also performed at subsaturation powers (usually 100 to 150 pA). Only cells in which the IPSC could be blocked by  $> 90\%$  with glutamatergic blockers were used ( $n = 5$  of 6) and the insensitive component was subtracted. Furthermore, in contrast to optogenetic stimulation IPSC peaks were detected between 5 and 15 ms following the stimulus. All further analysis was identical to that for optogenetic frequency stimulation.

## 2.15 Analysis

Analyses were performed using ImageJ, Microsoft Excel and Igor Pro. Fits were performed using Igor Pro. Statistical analyses were performed using GraphPad Prism 6 or Igor Pro

software. In order to maintain consistent statistical assumptions data were always tested with parametric tests (this was required to perform two way repeated measures ANOVA). In pharmacological experiments, IPSC amplitudes following block were normalized to their respective control values and then tested using one sided t-tests. Electrical versus optogenetic stimulation paradigms were compared using two sided, paired t-tests. IPSC distribution experiments were analyzed by two-way, repeated-measures ANOVA with Sidak's posttest comparing local versus remote stimulation in each blade. Frequency dependence experiments were analyzed by two-way ANOVA or one sided t-test with Bonferroni-Holm correction. Unless indicated otherwise data are given as mean  $\pm$  standard error of the mean.

### 3. Results

The primary goal of this study was to quantify the recruitment of feedback inhibition within the hippocampal dentate GC population. To achieve this, it is necessary to activate controlled subpopulations of GCs, while simultaneously monitoring the magnitude of feedback inhibition. Electrical stimulation of the mossy fiber tract in CA3 leads to antidromic activation of a subpopulation of GCs as well as their local postsynaptic targets. Importantly, it allows the selective activation of feedback inhibition, while omitting feedforward inhibition. However, for the quantification of the recruitment of feedback inhibition, it is necessary to not only control but also monitor the fraction of active GC. This was achieved by population  $\text{Ca}^{2+}$  imaging.

#### 3.1 Population $\text{Ca}^{2+}$ Imaging Assessment of the Recruitment of Feedback Inhibition

Every AP is accompanied by a transient rise in the intracellular  $\text{Ca}^{2+}$  concentration.  $\text{Ca}^{2+}$  sensitive fluorescent dyes allow recording such transients in a large number of cells simultaneously by fast, low-noise imaging techniques. I therefore set out to monitor the fraction of antidromically activated GCs via population  $\text{Ca}^{2+}$  imaging while recording feedback inhibition from a single GC within, or immediately adjacent to, the imaging field.

With most current imaging approaches single AP induced  $\text{Ca}^{2+}$  transients are only marginally above noise level. Therefore their reliable detection depends crucially on the exact experimental parameters such as cell type, imaging system, imaging parameters, intracellular dye, and dye concentration. Accordingly, it was necessary to begin by investigating the reliability of detection of single AP induced  $\text{Ca}^{2+}$  transients in our settings.

### 3.1.1 Detection of Single Action Potentials by Population Ca<sup>2+</sup> Imaging

In order to assess the relationship between AP firing and Ca<sup>2+</sup> fluorescence increase in our experimental settings, I recorded from OGB-1-AM bolus loaded GCs in cell-attached mode, while simultaneously imaging fluorescence changes with multibeam two-photon microscopy (**Fig. 3A, B**). The stimulation electrode was placed immediately adjacent to the imaging field. Cells were differentiated into true responders or non-responders on the basis of the presence or absence of stimulus induced cell-attached spikes (**Fig. 3C, D**, responders green, non-responders grey). A histogram of the peak  $\Delta F/F$  at the soma of non-responders upon a single stimulus was fitted with a Gaussian (**Fig. 3E**, grey dots, grey bars,  $n = 33$ ). Using a threshold of the quadruple standard deviation of this fit (0.94 %  $\Delta F/F$ , dashed line in Fig. 3E) I found that most true responders could also be identified by their Ca<sup>2+</sup> signal (**Fig. 3E**, green dots, green bars). In order to explore the expected false positive and false negative rates in these settings I plotted both as a function of the detection threshold (**Fig. 3F**, false positives grey, false negatives green). It is important to realize that the resulting rates will depend on the true positive rate. The data were well approximated by sigmoidal fits (**Fig. 3F**, black traces). Using the detection threshold of 0.94 %, I found that at a true positive rate of 3 % the number of false positives and false negatives would be exactly equal, in effect canceling each other out (**Fig. 3F**, inset).

Further, I noted a highly variable dye loading of different granule cells raising the question whether single AP induced Ca<sup>2+</sup> transients may not be detectable below a certain level of intracellular dye loading. However, there was no correlation between baseline fluorescence and peak  $\Delta F/F$  of either responders (**Fig. 3G**, F-test,  $p = 0.9$ ) or non-responders (not shown, F-test,  $p = 0.92$ ). A further potential source of systematic error is an increase in total diffracted light when a larger fraction of cells truly responds. This possibility arises, because in multibeam two-photon Ca<sup>2+</sup> imaging a CCD camera is used to record the fluorescence of the entire imaging field simultaneously. The effect would result in non-responders mimicking the transient waveform of responders and ultimately more non-responders being falsely detected at higher stimulation powers. However, the peak  $\Delta F/F$  of non-responders was not correlated to stimulation power (**Fig. 3H**, bottom, F-test,  $p = 0.67$ ). Thus, our settings allow the reliable detection of single AP induced Ca<sup>2+</sup> transients and the quantification of the active fraction of cells at the population level.

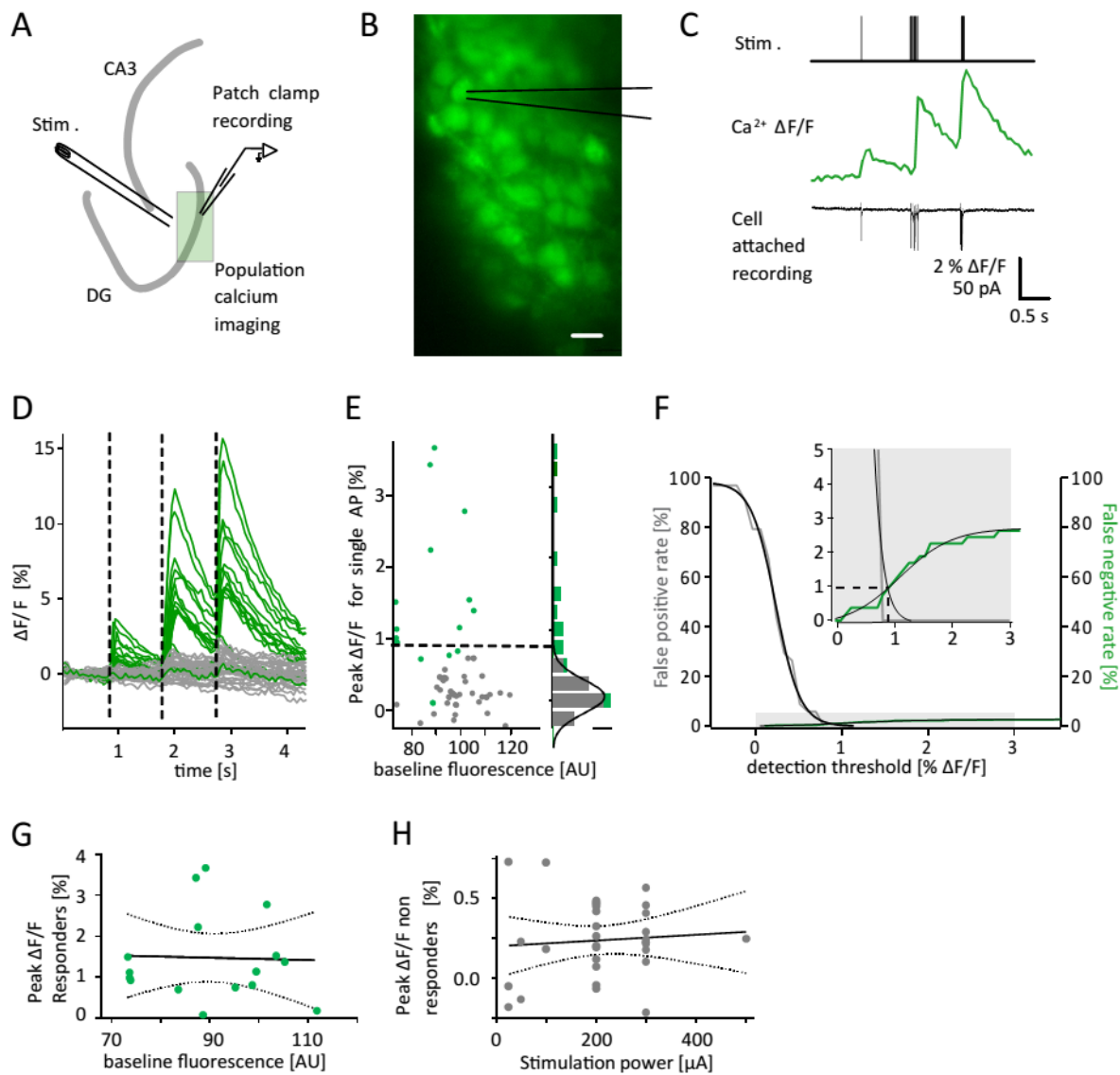


**Fig. 3) Detection of single action potential induced calcium transients,** A section of the dentate gyrus was loaded with OGB1-AM and imaged with multibeam two-photon microscopy, while antidromically eliciting action potentials and recording from individual cells in cell-attached mode. **A)** Schematic illustration of the experimental setup. **B)** Example of OGB1-AM loaded GCs. Scale bar: 10  $\mu\text{m}$  **C)** Cells were stimulated with a single pulse (left) or bursts of 5 pulses at 30 Hz (middle) or 100 Hz (right). Cell-attached recordings revealed the exact number of induced action potentials (bottom) which could then be correlated with the intracellular calcium dynamics (middle). **D)** Superposition of the calcium fluorescence traces of 49 recorded cells constituted of cells identified as responders (green) or non-responders (grey) by cell-attached recordings. **E)** Peak  $\Delta F/F$  of identified responders and non-responders plotted against their respective baseline fluorescence (left). A histogram of the peak  $\Delta F/F$  of both respective groups revealed a Gaussian distribution of the non-responders (right, scale bar = 5 cells). The dashed line indicates the detection threshold at the quadruple standard deviation of this fit (0.94%  $\Delta F/F$ ). **F)** False positive (grey) and false negative (green) rates were plotted as a function of the detection threshold and fitted with sigmoidal functions. A detection threshold of 0.94% leads to exactly equal numbers of false positives and false negatives at a true positive rate of 3% (inset, dashed lines). **G)** To test for potential effects of variable dye loading on detection efficacy, peak  $\Delta F/F$  of responders and baseline fluorescence intensity were tested for correlation. **H)** Since in multibeam two-photon calcium imaging the entire frame is detected simultaneously scattered light from responders at high stimulation powers might introduce a systematic error. Peak  $\Delta F/F$  of non-responders did not increase with stimulation power. Dashed lines in (G) and (H) represent the 95% confidence intervals of linear fits.

### 3.1.2 Determination of the Maximum Connectivity Plane

Next, I moved the stimulation electrode into stratum lucidum of CA3 in order to antidromically activate GCs via the mossy fiber tract, while minimizing direct electrical activation of hilar interneurons (**Fig. 4A**). Two cuts were made around the mossy fiber tract to sever CA3 backprojections (**Fig. 4A**, dashed lines, Scharfman, 2007). Mossy fibers are organized in a strictly laminar fashion (Andersen et al., 1971), i.e. they run in the plane perpendicular to the septo-temporal axis of the hippocampus. A portion of the hippocampus in which this plane is aligned with the dorsal brain surface is the dorsal part of the ventral hippocampus (three short dashed lines in **Fig. 4C, D**, see section 2.2 for details). Sections obtained at this depth are therefore expected to contain a maximum of intact mossy fibers and were therefore denoted maximum connectivity plane sections (MCP; see also Bischofberger et al., 2006; arrow in **Fig. 4B**). In the sections corresponding to this MCP the number as well as fraction of antidromically activatable granule cells was maximal, consistent with an intact mossy fiber tract (**Fig. 4E**,  $n = 40$  sections). Therefore all experiments included into the quantitative analyses were carried out in the thus defined MCP.

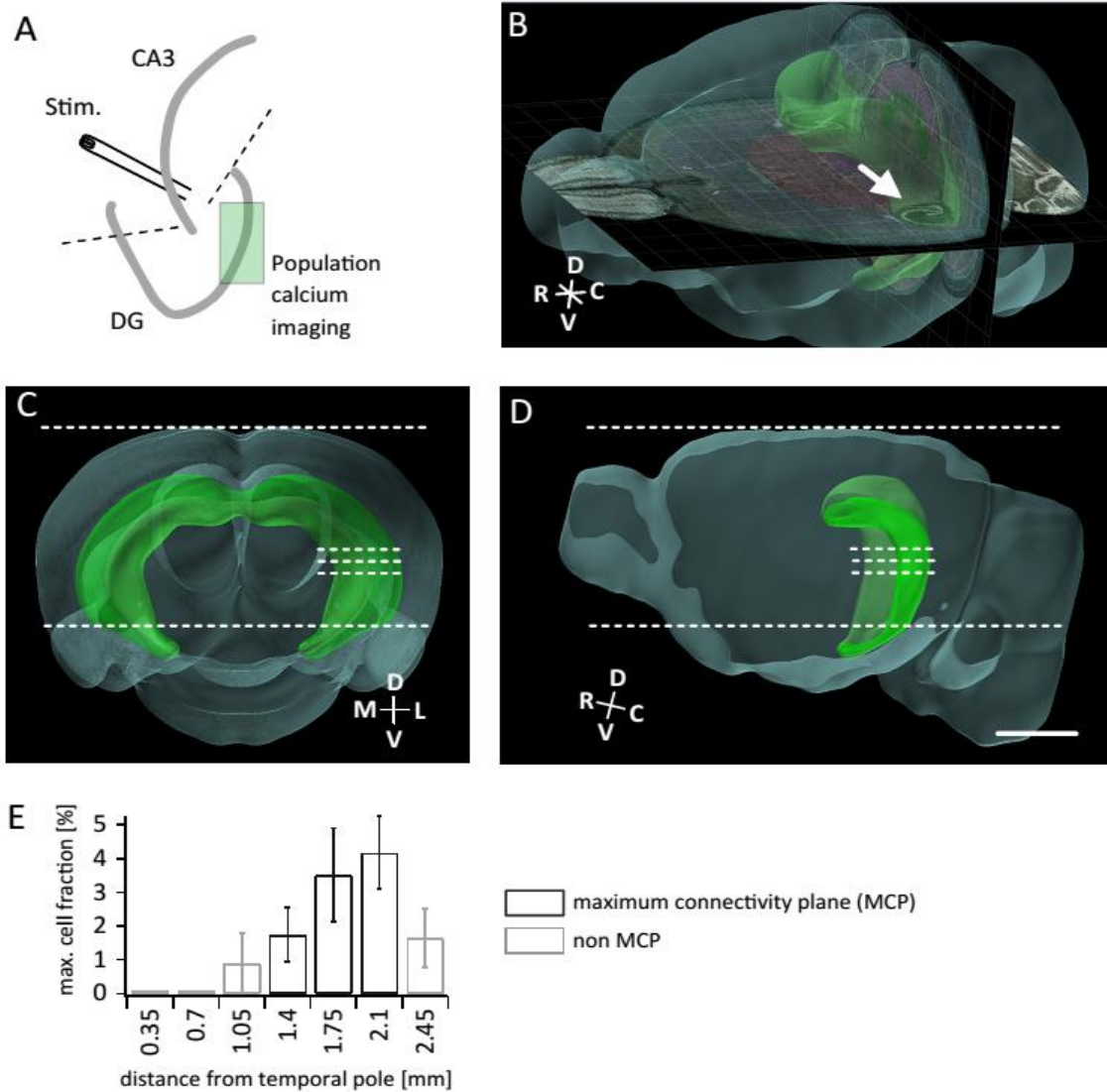


**Fig. 4) Selection of the maximum connectivity plane; A)** Illustration of the experimental setup in which GCs in an imaging-region (green square) are stimulated antidromically via a stimulation electrode placed into stratum lucidum of the adjacent CA3 region. Two cuts were made to isolate the mossy fiber tract while eliminating CA3 backprojections (dashed lines) **B) to D)** Three dimensional renderings of the mouse brain (blue) and hippocampal formation (green) from Allen Mouse Brain Atlas (Lein et al., 2007). D indicates dorsal, V ventral, R rostral, C caudal, M medial and L lateral. The maximum connectivity plane (MCP) is any plane perpendicular to the septotemporal axis (e.g. arrow in B). The mossy fibers of GCs are organized in a strictly lamellar fashion, i.e. they run within the MCP. **C,D)** Coronal (C) and sagittal (D) projections. A portion of the hippocampus in which the MCP is parallel to the dorsal surface of the brain is marked by three short dashed white lines. It is located approximately 1400 to 2100  $\mu\text{m}$  from the temporal pole, where the temporal pole is defined as the first section in which the three layered hippocampal structure was visible (lower white dashed line) **E)** During antidromic stimulation in the mossy fiber tract and simultaneous population calcium imaging a larger fraction of cells within the imaged sample could be activated in the sections corresponding to the MCP. Scale bar 2 mm

### 3.1.3 Selective Activation of Feedback Inhibitory Currents

In order to quantify the amplitude of feedback inhibition I recorded from single dentate GCs in whole-cell voltage clamp mode with a  $K^+$  free, low  $Cl^-$  intracellular solution. Cells were held at 0 mV creating a high  $Cl^-$  driving force. The experimental setup was as described above (**Fig. 5A**). Granule cells were filled with Alexa594 during recording to confirm their identity as granule cells (**Fig. 5B**, top). Stratum lucidum stimulation elicited transient outward currents, which increased with stimulation strength (**Fig. 5B**, bottom). The elicited currents were completely blocked by 10  $\mu$ M Gabazine (to  $1.5 \pm 0.9$  %, **Fig. 5C**, left,  $n = 6$ ,  $p < 0.001$ , one-sided t-test) confirming that they reflected inhibitory currents. Importantly, although the stimulation electrode was placed into stratum lucidum of CA3, hilar interneurons may still be activated directly. Their dendritic trees are expansive and may in some cases reach into the CA3 region. Furthermore, in some cases very high stimulation powers were required in order to reach saturation of the IPSC. However, larger stimulation powers also expand the stimulated area increasing the probability of direct interneuron stimulation. To ascertain that the elicited currents reflected exclusively disynaptic feedback inhibition, only cells in which IPSCs were completely abolished by blockage of excitatory neurotransmission (25  $\mu$ M CNQX + 50  $\mu$ M D-APV) were used (**Fig. 5C**, middle,  $n = 8$  of 23). An additional way to confirm that the IPSCs represented mossy fiber mediated feedback inhibition is to test their sensitivity to a selective agonist of the metabotropic glutamate receptor type 2/3 (mGluR2/3). This receptor is expressed in presynapses of mossy fibers onto dentate hilar border interneurons (Shigemoto et al., 1997). Its selective activation by low concentrations of DCG-IV reduces transmission onto these interneurons from mossy fibers but not CA3 pyramidal cells (Doherty and Dingledine, 1998; Toth et al., 2000). I found that IPSCs were reduced to  $16.3 \pm 6.1$  % by 0.5  $\mu$ M DCG-IV (**Fig. 5C**, right,  $n = 4$ ,  $p < 0.001$ , one-sided t-test) confirming they were mossy fiber mediated feedback IPSCs (Ewell and Jones, 2010; Sambandan et al., 2010).

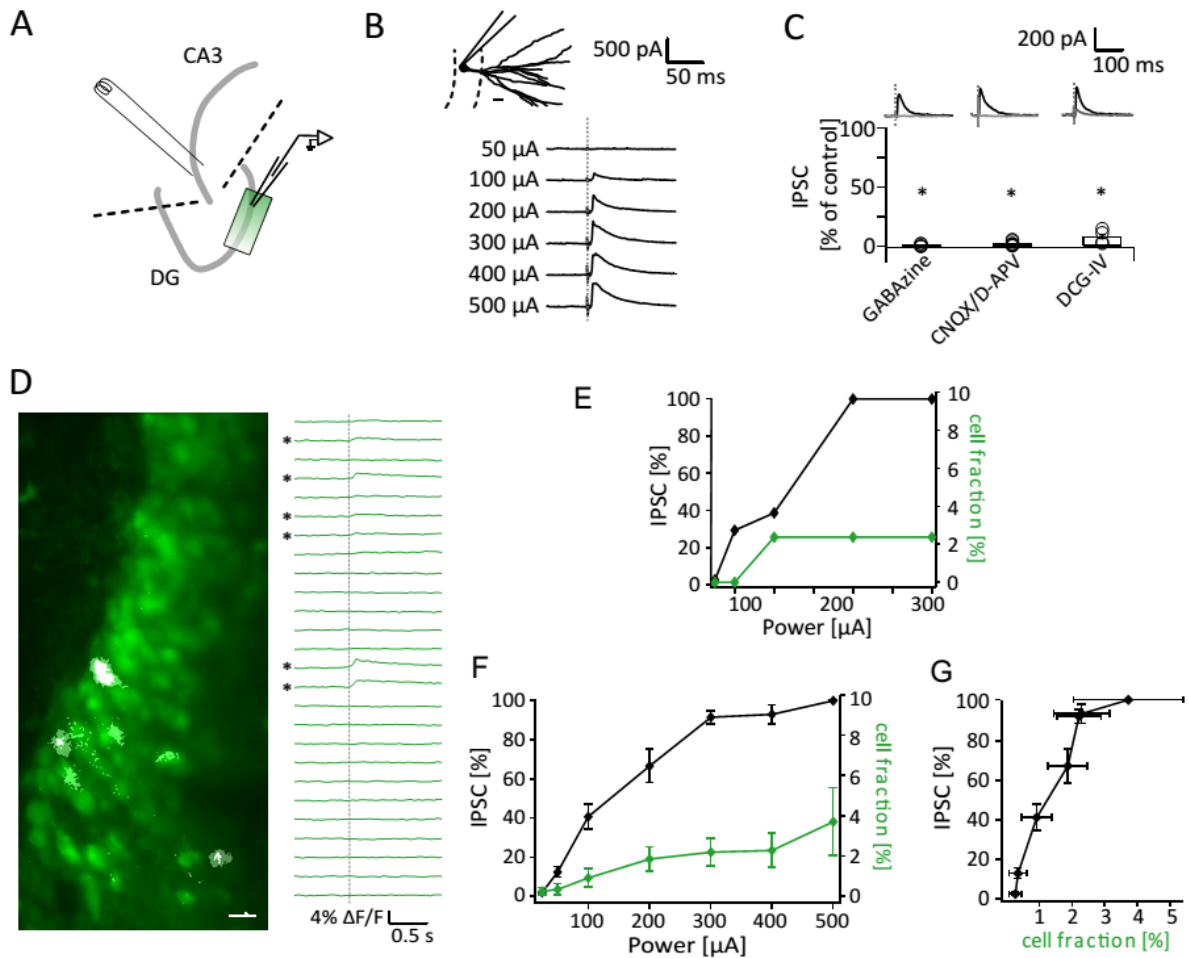


**Fig. 5) Steep recruitment of feedback inhibition assessed by population calcium imaging,** Combined IPSC recordings and population calcium imaging in MCP sections. **A)** Schematic of experimental setup. **B)** Dentate GCs were recorded and filled with Alexa 594 (top, scale bar 20  $\mu\text{m}$ ) while eliciting feedback IPSCs with incremental stimulation intensities (bottom). **C)** IPSCs were completely blocked by 10  $\mu\text{M}$  Gabazine and largely by 0.5  $\mu\text{M}$  DCG-IV. Only IPSC measurements in which a complete block with 25  $\mu\text{M}$  CNQX + 50  $\mu\text{M}$  D-APV was achieved were used. **D) Left,** OGB1-AM loaded population of dentate GCs (green) overlaid with a  $\Delta\text{F}/\text{F}$  projection after stimulation (white). **Right,**  $\Delta\text{F}/\text{F}$  traces of a subpopulation of these cells. GCs detected as active are labeled by asterisks. **E)** Plot of the IPSC amplitude (black) and active cell fraction (green) as a function of stimulation power for an individual section. **F)** Summary plot of the increases of IPSC amplitude and active cell fraction with stimulation intensity ( $n = 8, 22$  respectively). The mean IPSC amplitude at saturation was  $324.1 \pm 99.2$  pA ( $n = 8$ ) **G)** Data from F plotted to show the recruitment of feedback inhibition as a function of the active cell fraction.

### 3.1.4 Steep Recruitment of Feedback Inhibition (1)

Combining IPSC recordings (**Fig. 5B**) with population  $\text{Ca}^{2+}$  imaging (**Fig. 5D**) in individual slices allowed probing the relation between the IPSC amplitude and the active fraction of GCs. The input-output relation of inhibition was recorded in a GC within or immediately adjacent to the imaging field (**Fig. 5A**). The IPSC amplitudes of all cells were normalized to the

amplitudes of their respective saturation. **Fig. 5E** shows an example from an individual slice in which the active cell fraction saturates at 2.4 % of the imaged population. In those sections in which both a saturating, CNQX/D-APV sensitive IPSC recordings as well as population imaging could be completely obtained IPSCs reached 100 % when  $2.9 \pm 1.5$  % of GCs were active ( $n = 6$ ). However, due to the small number of active cells within each slice, this estimate is subject to high variability. A more precise estimate can be gained by pooling the data from all appropriate recordings. These include IPSC recordings with successful glutamatergic block from 8 sections, of which 2 were excluded from imaging analysis due to insufficient dye loading, and videos from 23 sections of which 15 were excluded from IPSC analysis due to failure to demonstrate a glutamatergic block. I found a saturation of the IPSC at approximately 300  $\mu$ A stimulation strength, where the mean active cell fraction was  $2.2 \pm 0.7$  % (**Fig. 5F**). Accordingly, my results indicate that the magnitude of feedback inhibition rises steeply reaching 90 % with less than 2.2 % of granule cells active and complete saturation at  $3.7 \pm 1.7$  % of cells (**Fig. 5G**).

### 3.2 Optogenetic Assessment of the Recruitment of Feedback Inhibition

The experimental paradigm described above yielded a first estimate of the recruitment of feedback inhibition in GCs. However, it has several advantages as well as disadvantages, which will be discussed in detail below (chapter 4.2). The most important caveat is that, although the IPSC amplitude appeared to saturate, it was not possible to activate larger cell fractions without starting to recruit interneurons directly. Therefore it is necessary to confirm that IPSCs are actually saturated. Additionally, antidromic stimulation can be expected to activate a disperse population of GCs spread out in three dimensions. Although this aspect is likely to correspond to the physiological situation it raises the question, if the imaged sample population is representative of the population involved in recruiting the interneurons mediating local inhibition. More generally, it raises the question how feedback inhibition is spatially distributed. This is important, since cells which are not integrated into the feedback inhibitory circuit should not be considered when assessing the active fraction of the recruiting population.

### 3.2.1 Optogenetic Activation of Feedback Inhibitory Currents

We therefore decided to verify the findings from the population  $\text{Ca}^{2+}$  imaging approach by an alternative method, namely the controlled optogenetic activation of varying fractions of GCs at defined locations within the slice. To this end mice selectively expressing  $\text{ChR2}^{(\text{H134R})}$ -eYFP in GCs were created by crossing Prox1-Cre mice ( $\text{Tg}^{(\text{Prox1-cre})}\text{SJ39Gsat/Mmucd}$ ; Gong et al., 2003, 2007) with Ai32-mice ( $\text{B6};129\text{S-Gt}^{(\text{ROSA})}26\text{Sor}^{\text{tm32}(\text{CAG-COP4}^*\text{H134R/EYFP})\text{Hze}/\text{J}$ ). Prox1-Cre mice express Cre-recombinase under the prospero-related homeo box 1 promoter which, in the central nervous system, is expressed specifically in dentate GCs (Gong et al., 2003, 2007; see also Allen Mouse Brain Atlas, Lein et al., 2007). Ai32 mice are homozygous for the conditional Rosa-CAG-LSL- $\text{ChR2}^{(\text{H134R})}$ -eYFP-WPRE construct (Madisen et al., 2012). In it a loxP-flanked STOP cassette prevents transcription of  $\text{ChR2}^{(\text{H134R})}$ -eYFP under the universal CAG promoter. The resulting double transgenic mice stably and selectively expressed  $\text{ChR2}^{(\text{H134R})}$ -eYFP in dentate gyrus GCs (**Fig. 6**). Fluorescence was concentrated in the regions of GC processes while the GC-layer itself (**Fig. 6A**, two short black lines) displayed little fluorescence (compare Kheirbek et al., 2013). This is most likely due to a higher membrane fraction in these regions, since  $\text{ChR2}^{(\text{H134R})}$ -eYFP is a membrane bound construct. Note the prominent visibility of the mossy fiber tract (**Fig. 6A**, arrow).

In order to achieve spatially controlled illumination, we used a laser integrated into the microscope light path controlled in x and y direction by galvanometric mirrors (**Fig. 6B**). At the focal plane this resulted in a narrow laser spot with  $8.36 \pm 0.04 \mu\text{m}$  FWHM and up to 1.7 mW power (corresponding to  $P = 7 \text{ AU}$ ; **Fig. 6B**, inset). Use of a low magnification, water immersion objective (10x) allowed the rapid placement of this laser spot along the entire dentate GC layer (**Fig. 6A**, field of view indicated by blue square).

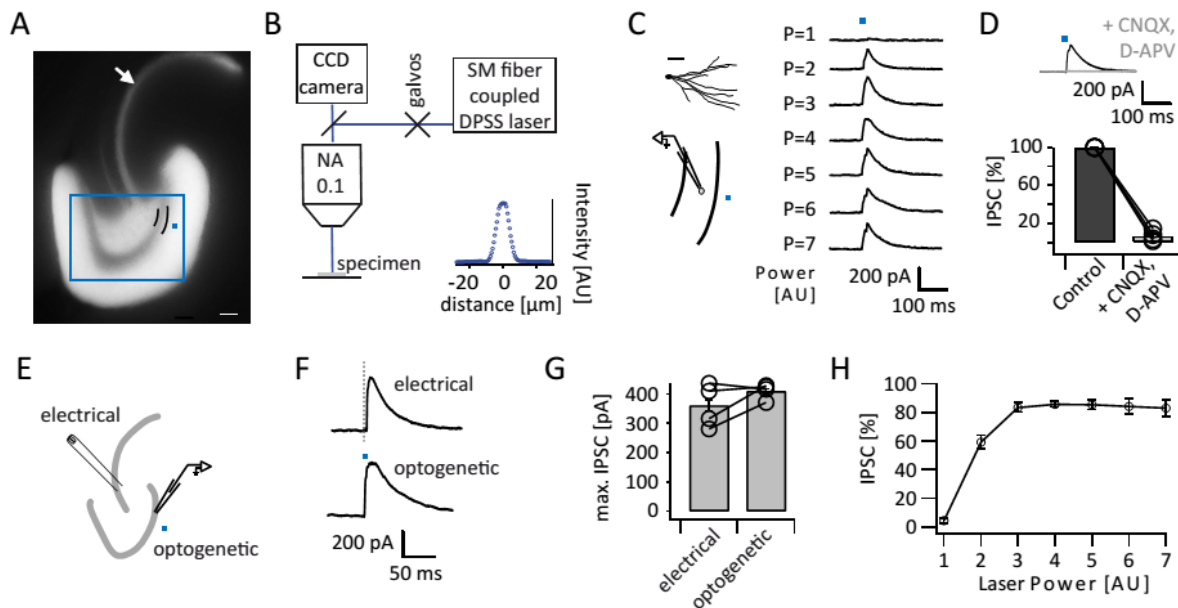


**Fig. 6) Optogenetically elicited feedback inhibition**, Mice constitutively expressing Chr2<sup>(H134R)</sup>-EYFP controlled by the Prox1 promoter reliably and specifically showed EYFP expression in the dentate GC dendritic and axonic regions. **A)** Epifluorescence image of an acute maximum connectivity plane slice. Note the prominent visibility of the mossy fiber tract (arrow). The field of view under the 10x water immersion objective used for optogenetic stimulation is indicated by a blue square. A portion of the superior blade of the GC layer is outlined by two short black lines and the blue dot indicates a typical stimulation site relative to it. **B)** Schematic of the microscope setup used to achieve spatially controlled illumination. The inset shows the intensity profile of the laser focus on a non-diffracting surface. **C) Top left**, reconstruction of an A594 filled dendritic tree from an epifluorescence image (scale bar 50  $\mu$ m). **Left**, illustration of the position of the recorded cell in the GC layer and the position of the stimulation spot 40  $\mu$ m into the molecular layer; **Right**, IPSCs for 20 ms stimulation powers at increasing laser power (P = 1 to 7 AU). Each trace represents an average of 3 trials. **D)** All optogenetically elicited IPSCs were completely blocked by 40  $\mu$ M CNQX + 50  $\mu$ M D-APV (n=9). **E)** Schematic of the two stimulation paradigms in an individual slice. **F)** Example traces for IPSCs following electrical or focal optogenetic stimulation. **G)** The maximal IPSC amplitude was similar for the two stimulation paradigms (361  $\pm$  37 versus 410  $\pm$  13 pA for electrical and optogenetic stimulation respectively, paired t-test, p = 0.28, n = 4) **H)** Summary IPSC amplitudes from cells in the superior blade (n=7 cells). IPSC amplitudes for each cell were normalized to the maximum amplitude measured in that respective cell.

In order to assess the recruitment of feedback inhibition I recorded feedback inhibitory currents upon a single 20 ms light pulse within 100  $\mu$ m of the recorded cell and 40  $\mu$ m into the molecular layer (**Fig. 6C**, left). Progressively increasing the laser power led to increasing IPSC amplitudes which usually saturated quite rapidly (around P = 3 AU corresponding to 300  $\mu$ W, **Fig. 6C**, right). Optogenetically elicited inhibitory currents were completely abolished by 40  $\mu$ M CNQX + 50  $\mu$ M D-APV, confirming that interneurons were not directly activated (**Fig. 6D**, n = 9). In order to compare the optogenetic activation of feedback inhibition to antidromic electrical stimulation I combined the two techniques in a subset of sections (**Fig. 6E, F**). The maximal CNQX/D-APV sensitive IPSC amplitude achievable through antidromic

electrical stimulation was similar to the maximal optogenetically elicited IPSC (**Fig. 6G**,  $361 \pm 37$  versus  $410 \pm 13$  pA respectively, paired t-test,  $p = 0.28$ ,  $n = 4$ ). Combining the data on IPSC recruitment by local stimulation normalized to the maximal individually observed IPSC for each cell revealed a clear saturation of inhibition as early as  $P = 3$  AU corresponding to  $300 \mu\text{W}$  ( $n = 7$ , **Fig. 6H**).

### 3.2.2 Optogenetic Activation of Granule Cells

Next, I estimated the GC fraction which is activated at each respective laser power. To this end one to two GC were recorded in cell-attached mode in the same slices in which the input-output relation of inhibition was recorded ( $n = 14$  sections, 26 cells). Cells were recorded in both the superior and inferior blades ( $n = 13$ , 13 respectively). Since their activation properties did not significantly differ, cells from both blades were pooled. In order to assess the spatial distribution of GC activation resulting from a single stimulation spot (as used to probe inhibition) illumination spots were placed at  $100 \mu\text{m}$  intervals along the GC layer and probed sequentially (**Fig. 7A**). This allowed the estimation of a mean firing probability as a function of the distance between the stimulation spot and the recorded cell for each laser power (**Fig. 7B**, three example powers shown). Here the distance is measured at the slice surface, along the GC layer (x-distance in **Fig. 7B, D, E, G**). However, the firing probability of cells in the vicinity of the illumination spot is likely to increase not only as a function of the laser power and spread at the surface, but also of the penetration depth of the light cone. Accordingly, an accurate estimation of the total active cell fraction in the slice requires knowledge about the light intensity distribution throughout the slice at different powers. Therefore, I modified the setup in order to record the light intensity distribution at the other side of hippocampal slices of varying depth, with the illumination laser focused to the slice surface as for GC recordings (**Fig. 7C**). As expected the light intensity decayed rapidly along the slice surface (**Fig. 7D, E**; x-distance) and less rapidly with increasing slice depth (**Fig. 7D, F**; z-distance). The light intensity profile in x and y (the plane parallel to the slice surface) was isometric, so only the x and z dimensions are plotted in **Fig. 7D**. Since the GCs form a narrow cell layer, the spread of GCs is adequately described by the xz-plane, with 'x' again referring to the distance along the GC-layer at the surface and 'z' to the slice depth. Moreover, since the light intensity profile is isometric in x and y, the curvature of the GC-

layer can be ignored, because the x-distance from any illumination spot just outside the GC layer will correspond to the radial distance from the center of the isometric xy-profile. To account for the narrow spread of GCs in y (perpendicular to the xz-plane), GCs were picked from randomly chosen y-positions within the GC layer. In order to obtain a measure which would allow the estimation of firing probabilities throughout the xz-plane, I calculated the light-intensity weighted mean of xz-distances for every pixel along the slice surface (virtual distance; **Fig. 7G**; illustration for a single pixel at 440  $\mu\text{m}$  x-distance from the laser focus). This 'virtual distance' incorporates the precise profile of the light intensity distribution at a given power and can be calculated not only for the pixels in the top row (at the surface) but also for all other pixels in the xz-plane. It further allows the assignment of the measured probabilities at the top row (**Fig. 7B**) to the corresponding virtual distances for each respective laser power (**Fig. 7H**). The resulting distribution of firing probabilities is well approximated by a Gaussian fit allowing the extrapolation of firing probabilities for all xz-distances in the slice at a given power. The mean of the firing probabilities across all locations corresponds to the mean probability of any cell to be active. Given the entire population of GCs, this mean firing probability will be equivalent to the active cell fraction.

Finally, I noted that a large fraction of the recorded spikes occurred with larger latency than the typical IPSC following the beginning of the 20 ms stimulation pulse (**Fig. 7I**, example from a single slice). Since only APs preceding the IPSC can participate in its recruitment, I calculated the fraction of total spikes which preceded the mean IPSC latency for every power (**Fig. 7J**). Correction of the active cell fraction by this factor (**Fig. 7J**, bottom) yields an estimate of the active cell fraction responsible for recruiting an IPSC at a given laser power (**Fig. 7K**, black). For comparison the cell fraction was also estimated assuming no firing probability decay with increasing slice depth (**Fig. 7K**, green) or assuming isometric firing probability decay (**Fig. 7K**, blue).

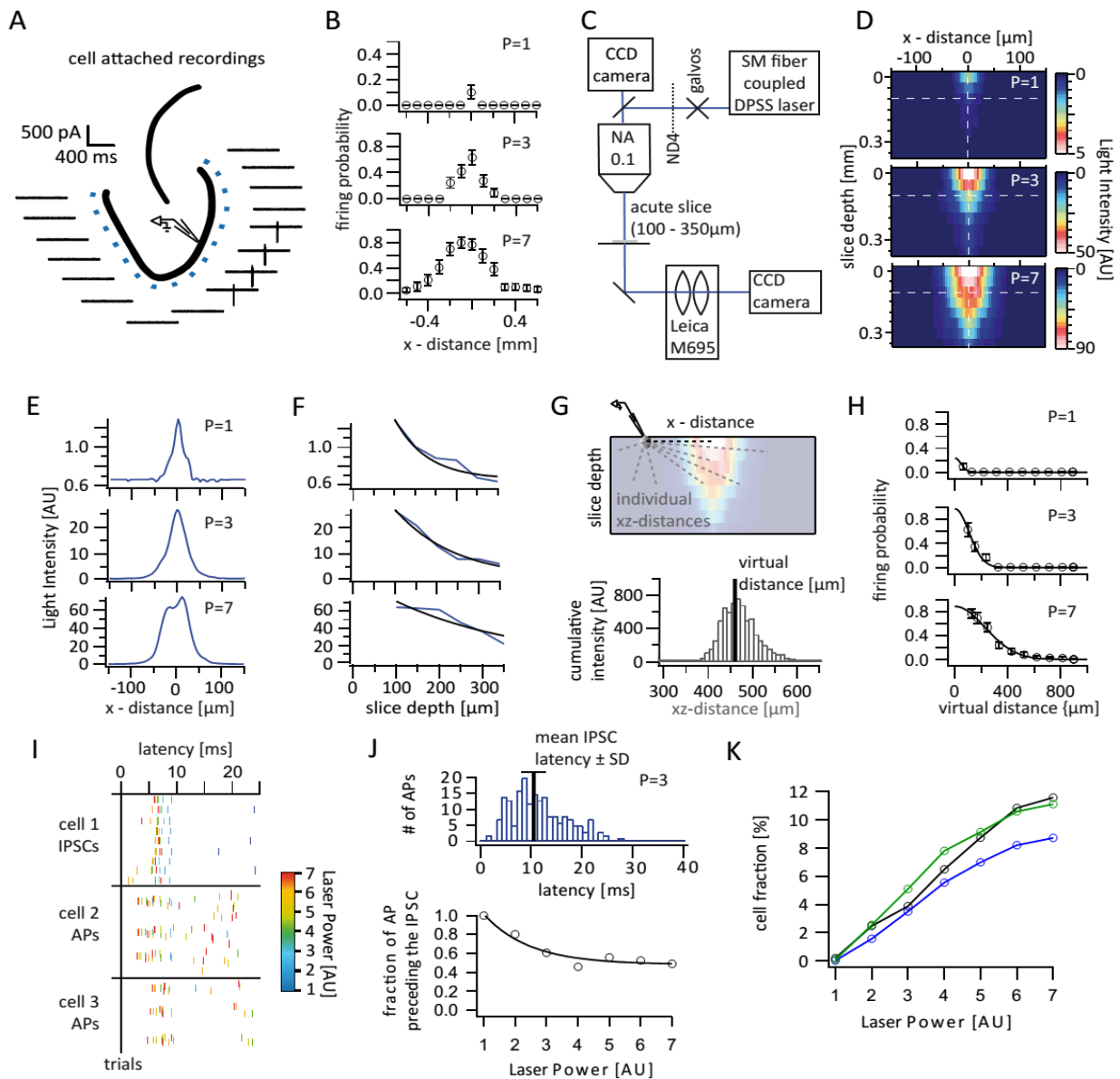


**Fig. 7) Calculation of the optogenetically activated cell fraction, A)** Schematic illustration of the stimulation paradigm and example traces of an individual trial. Cells were recorded in cell-attached mode while systematically stimulating at varying distances along the GC layer. Traces are from a representative single trial at  $P = 3$ . **B)** Calculating the mean firing probability of every location over trials and cells yields a firing probability distribution for each laser power (three example powers shown). **C)** Schematic of the modified setup to record the 3D light intensity profile in an acute slice. **D)** Cross section of the light intensity profile of the laser spot at increasing slice depth. The dashed white lines indicate the location of the cross sections shown in (E) and (F). Depths below  $100\ \mu\text{m}$  were extrapolated from fits to (E) and (F). **G) top**, Illustration of the calculation of the virtual distance for a particular cell/pixel  $440\ \mu\text{m}$  lateral to the laser focus. The distances between the given cell/pixel and all other pixels (individual  $xz$ -distances) were weighted by the intensity at those pixels. **Bottom**, This weighting is illustrated by a histogram displaying the intensities for each respective  $xz$ -distance. The virtual distance corresponds to the intensity weighted mean of  $xz$ -distances. **H)** The measured firing probabilities were assigned to the respective virtual distances. The resulting firing probability distribution was well approximated by a Gaussian fit (black line). **I)** Example of the IPSC and AP latencies upon a stimulation pulse from an individual slice. Laser Powers are color coded. **J) Top**, Example Histogram of the distribution of all AP latencies for  $P = 3$  (blue). The black bar indicates the mean IPSC latency  $\pm$  standard deviation at that power. **Bottom**, The fraction of action potentials that precede the mean IPSC for each power was well approximated by an exponential fit (black line). Light stimulation in (I) and (J) was from 0 to 20 ms. **K) black**, Estimated active cell fraction in the slice calculated from the light intensity profiles in (D) and the virtual firing probability distributions in (H) and corrected by the fraction of APs occurring after the mean IPSC (J). The estimated active cell fraction is identical to the mean firing probability throughout the slice. For comparison the cell fraction was also estimated assuming no firing probability decay with increasing depth (green) or assuming isometric decay (blue).

### 3.2.3 Steep Recruitment of Feedback Inhibition (2)

Combining the input-output curves for inhibition and cell activation from sections 3.2.1 and 3.2.2 respectively yields the feedback inhibition recruitment curve (**Fig. 8A**). The recruitment of feedback inhibition saturates at a comparable active cell fraction as in the  $\text{Ca}^{2+}$  imaging approach (compare Fig. 5, section 3.1.4; approximately 4 % of GCs). Furthermore, higher active cell fractions (up to 12 %) do not lead to any further increase, confirming the saturation. However, it is still not certain that larger cell fractions cannot lead to additional recruitment of inhibition.

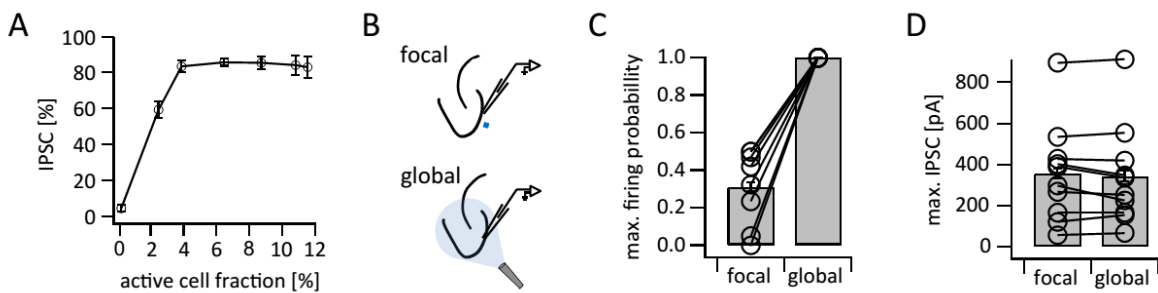


**Fig. 8) Recruitment of feedback inhibition assessed optogenetically, A)** Data from Figs. 4 and 5 combined showing the recruitment of feedback inhibition as a function of the active cell fraction. **B)** Schematic illustration of focal and global optogenetic stimulation. **C)** Comparison of the maximal firing probability (at the largest stimulation power) of individual GCs for focal and global stimulation. **D)** Comparison of the maximal IPSC amplitude under focal and global stimulation for individual GCs.

In order to unequivocally confirm the saturation of inhibition within the local network I additionally globally activated the GC population in a subset of sections via a light fiber positioned over the slice surface, while stimulating at high powers (up to 50 mW; **Fig. 8B**). Under these conditions all cells tested fired APs with 100 % reliability, even though focal stimulation in direct proximity to the cell led to much lower maximal firing probabilities (**Fig. 8C**,  $100.0 \pm 0.0$  versus  $31.2 \pm 7.1$  % respectively, paired t-test,  $p < 0.0001$ ,  $n = 8$ ). However, the maximal amplitude of inhibition did not increase further during global stimulation when compared to maximal focal stimulation (**Fig. 8D**,  $356.9 \pm 76.2$  versus  $344.3 \pm 77.5$  pA, paired t-test,  $p = 0.29$ ,  $n = 10$ ). Thus the recruitment of feedback inhibition in the DG is steep, with sparse populations of GCs efficiently leading to maximal recruitment of feedback inhibition.

### 3.3 Absence of Single GC Induced Feedback Inhibition

Previous work has addressed the initial phase of the recruitment of feedback inhibition in various contexts (Kapfer et al., 2007; Miles, 1990; Silberberg and Markram, 2007). The authors report the ability of even a single principal cell to activate feedback inhibitory interneurons and a supralinear increase of inhibition as the second and third principal cells are co-activated (Kapfer et al., 2007). Given my findings so far I asked whether single GCs might also suffice to elicit feedback inhibition in the DG. To this end I performed dual patch-clamp recordings and elicited short trains of ten APs at 100 Hz in one cell while monitoring inhibition in the other (**Fig. 9A**). Inhibition was monitored either in VC, while holding the cell a 0 mV to allow the detection of small IPSCs (**Fig. 9B**, n = 7 cell pairs, 7 directions) or current clamp while holding the cell at -60 mV, allowing to probe for inhibition in both directions (n = 4 cell pairs, 8 directions). However, I did not find clear single GC induced feedback inhibition in any case.

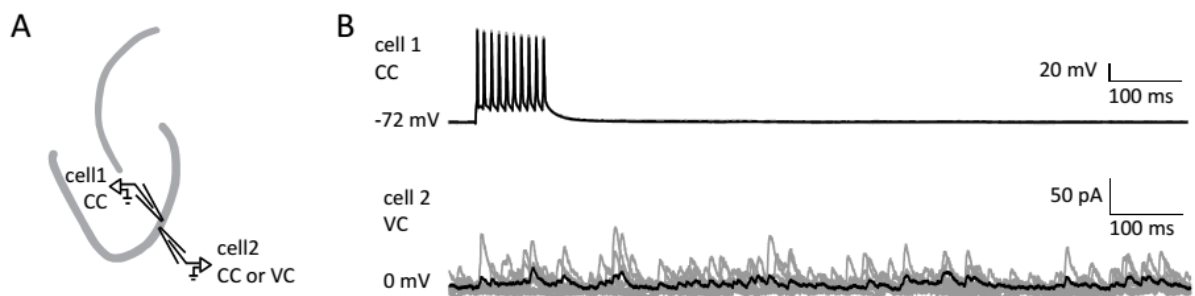


**Fig. 9) Absence of single granule cell induced feedback inhibition**, Pairs of juxtaposed GCs (< 100  $\mu\text{m}$  distance) were patched to test for single GC induced feedback inhibition. **A)** Schematic illustration of the experimental setup. **B)** Example of a paired recording where cell 1 is fired at 100 Hz in current clamp mode while cell two is recorded in voltage clamp mode in order to detect IPSCs. (grey, 10 individual trials; black, average). Note the high spontaneous activity rate typical of MCP sections.

### 3.4 Spatial Distribution of Feedback Inhibition

Recent evidence indicates that inhibition by PV<sup>+</sup> fast spiking hilar border interneurons is non-uniformly distributed over space (Strüber et al., 2015). To test whether feedback inhibition by the entire ensemble of feedback inhibitory interneurons also displays a spatial gradient I activated cell populations at 100  $\mu\text{m}$  intervals along the GC layer while recording inhibition in individual GCs (**Fig. 10A**). Spatial profiles were recorded for increasing laser powers in cells in the superior as well as inferior blade of the DG (**Fig. 10B, C** respectively;  $n = 8$  cells for each blade). IPSC amplitudes across locations and powers were normalized to the maximal IPSC amplitude of each respective cell. It did not differ between cells in different blades ( $366 \pm 40$  versus  $390 \pm 84$  pA for superior and inferior blades respectively; t-test,  $n = 8, 8$ ;  $p = 0.800$ ).

#### 3.4.1 Amplitude of Local and Remote Inhibition at Saturation

First, I investigated the distribution of feedback inhibition at stimulation powers at which inhibition had saturated (**Fig. 10D, E**). In all cells tested the inhibition was greatest when stimulating in the direct vicinity of the recorded cell ( $n = 8, 8$  for superior and inferior blades respectively). Activating cells at increasing distances led to monotonically decreasing IPSC amplitudes for both blades. However, even at the most distal stimulation sites the inhibition never decreased to zero, indicating that even the most distal cells from the contralateral blade contribute to feedback inhibition of a given GC. In order to statistically compare the relation of local versus remote stimulation between blades I defined a remote location in the contralateral blade at 800  $\mu\text{m}$  from the recorded cell (measured along the granule cell layer and equidistant in all slices; **Fig. 10D, E**; grey lines) and compared it to the local IPSC (stimulating in proximity to the recorded cell; black lines). As expected, remote inhibition was significantly smaller than local inhibition in both blades (**Fig. 10F**; two-way repeated-measures ANOVA,  $p < 0.0001$ ; recordings within superior as well as inferior blade significant in Sidak's multiple comparison test, both  $p < 0.0001$ ). No significant differences were observed between blades.

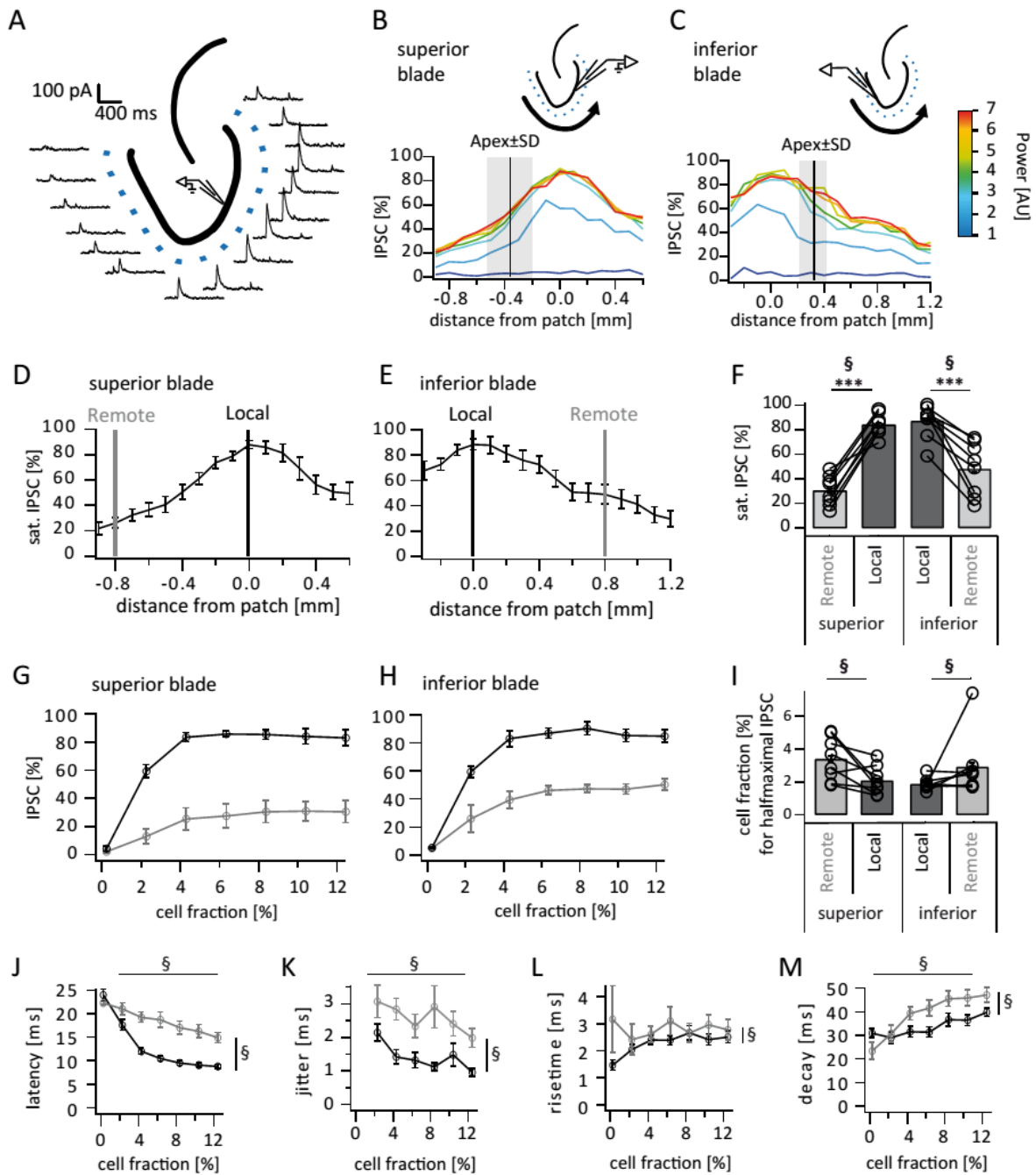


**Fig. 10) Spatial distribution of feedback inhibition, A)** Schematic illustration of the stimulation paradigm and example of an individual trial. Cells were recorded in whole-cell VC mode while systematically stimulating at varying distances along the GC layer. Traces are from a representative single trial at  $P = 3$ . **B,C)** Distribution of IPSC amplitudes as a function of the distance of the stimulation site for superior and inferior blade GCs respectively ( $n=8,8$ ). Traces represent the mean of IPSC amplitude for cells aligned to the recording location (0 mm). The distance of these cells to the apex  $\pm$  standard deviation is indicated by the black bar and grey area respectively. Individual laser powers are color coded. **D,E)** IPSC distribution over space at saturation. Black and grey bars indicate a local and a remote location at 800  $\mu$ m from the recorded cell respectively **F)** Comparison of the amplitude of the locally and remotely activated IPSCs at saturation (two way repeated measures ANOVA, overall test indicated by  $\S$ : Blade  $p = 0.128$ ; Distance  $p < 0.0001$ , Interaction  $p = 0.089$ ; Sidak's multiple comparison post tests indicated by \*: superior blade  $p < 0.0001$ , inferior blade  $p < 0.0001$ ). **G,H)** Comparison of the recruitment curves during local (black) or remote (grey) stimulation for superior and inferior blade respectively. **I)** Comparison of the cell fraction required for halfmaximal IPSC activation between stimulation sites and blades (two way repeated measures ANOVA overall test indicated by  $\S$ : Blade  $p = 0.470$ , Distance  $p = 0.014$ , Interaction  $p = 0.759$ ; Sidak's multiple comparison post tests not significant: superior blade  $p = 0.087$ , inferior blade  $p = 0.189$ ). (continued on next page)

**J-M)** Since no differences were observed between blades in any respect cells from both blades were pooled for the analysis of IPSC kinetics between local (black) and remote (grey) stimulation. To test for systematic variations of kinetic parameters with increasing active cell fractions as well as stimulation site two way repeated measure ANOVAs with no post tests were performed. Overall significance indicated by §. **J)** Cell fraction  $p < 0.0001$ , Distance  $p < 0.0001$ , Interaction  $p = 0.031$ . **K)** Cell fraction  $p = 0.037$ , Distance  $p < 0.0006$ , Interaction  $p = 0.707$ . **L)** Cell fraction  $p < 0.633$ , Distance  $p = 0.010$ , Interaction  $p = 0.388$ . **M)** Cell fraction  $p < 0.0001$ , Distance  $p = 0.0008$ , Interaction  $p = 0.1243$ .

#### 3.4.2 Recruitment of Local and Remote Feedback Inhibition

Next, I investigated whether there are differences in the recruitment dynamics of local versus remote inhibition between blades (black and grey respectively, **Fig. 10G, H**). To this end I calculated the active cell fraction which produces half maximal inhibition during local or remote stimulation for each individual cell (**Fig. 10I**). Comparison of the recruitment between the four groups revealed no differences between blades (two-way repeated-measures ANOVA;  $p = 0.470$ ). However, local inhibition was significantly more steeply recruited than remote inhibition ( $p = 0.014$ ). While local inhibition had reached 50 % of saturation amplitude at  $1.99 \pm 0.22$  % active cells remote inhibition required  $3.17 \pm 0.57$  % for halfmaximal activation (pooled over blades). This implies that the smaller amplitude of remote compared to local feedback inhibition is even more pronounced in the subsaturation domain.

#### 3.4.3 Kinetic Properties of Local and Remote Feedback Inhibition

Next, I tested if IPSCs elicited by increasing GC populations differed between local and remote activation with respect to their kinetic properties. Since all previous data showed no indication of blade specific differences the analysis of the kinetics of feedback IPSCs were performed on the pooled data for both blades. Interestingly, local and remote inhibition differed in all tested respects while the active cell fraction was also often significantly correlated to kinetic properties (**Fig. 10J - M**). Local IPSCs occurred with shorter latency and lower jitter than remote IPSCs (**Fig. 10J, K**;  $p < 0.0001$  and  $p = 0.0006$  respectively). Furthermore, both latency and jitter decreased as larger populations were activated ( $p < 0.0001$  and  $p = 0.004$  respectively). IPSCs were also significantly slower in remote versus local inhibition. IPSC rise time was slightly shorter in the larger local IPSCs (**Fig. 10L**;  $p =$

0.010) but did not correlate with the active cell fraction ( $p = 0.633$ ). Similarly, decay times were significantly shorter in local versus remote inhibition, at least at larger active cell fractions (**Fig. 10M**;  $p = 0.0008$ ). Finally, the decay time progressively increased with increasing stimulation power (**Fig. 10M**;  $p < 0.0001$ ). Accordingly, remote inhibition arrives at its target cells up to 10 ms later and with greater jitter. Furthermore, it produces significantly slower IPSCs.

### 3.5 Frequency Dependence of Feedback Inhibition

As noted in the introduction, the feedback inhibition ultimately arriving in dentate GCs is potentially a product of complex interactions within the feedback inhibitory microcircuitry. Different connections within this network may facilitate or depress in variable frequency dependent manners. I therefore investigated the frequency dependent evolution of compound feedback inhibition between 1 Hz and continuous stimulation (**Fig. 11**). Trains of ten feedback IPSCs were elicited by focal light stimulation at a single site (**Fig. 11A**). For all frequencies tested the IPSC amplitudes appeared to either stay constant or slightly depress during the train (**Fig. 11B**,  $n = 9$ ). Comparison of adaptation between local and remote stimulation revealed no overt differences (**Fig. 11C**; two way ANOVA, stim. location  $p = 0.491$ ,  $n = 9, 10$  for local and remote stimulation respectively). To see if individual GCs could follow trains of stimulation at these frequencies I also probed the firing probability in response to each pulse in cell-attached mode (**Fig. 11D**). Interestingly, the firing probability during a train decreased dramatically, most prominently during continuous stimulation (to  $0.16 \pm 0.03$ , one sample t-test,  $p < 0.0001$ ,  $n = 10$ ). This indicates that the number of GCs required to maintain a certain level of inhibition decreases during prolonged activity, suggesting some facilitative process. To test for facilitation directly I used antidromic electrical stimulation trains (**Fig. 11E**). In contrast to optogenetic stimulation IPSCs facilitated over the course of a train for frequencies greater than 10 Hz (**Fig. 11G, H**,  $n = 7$ ).

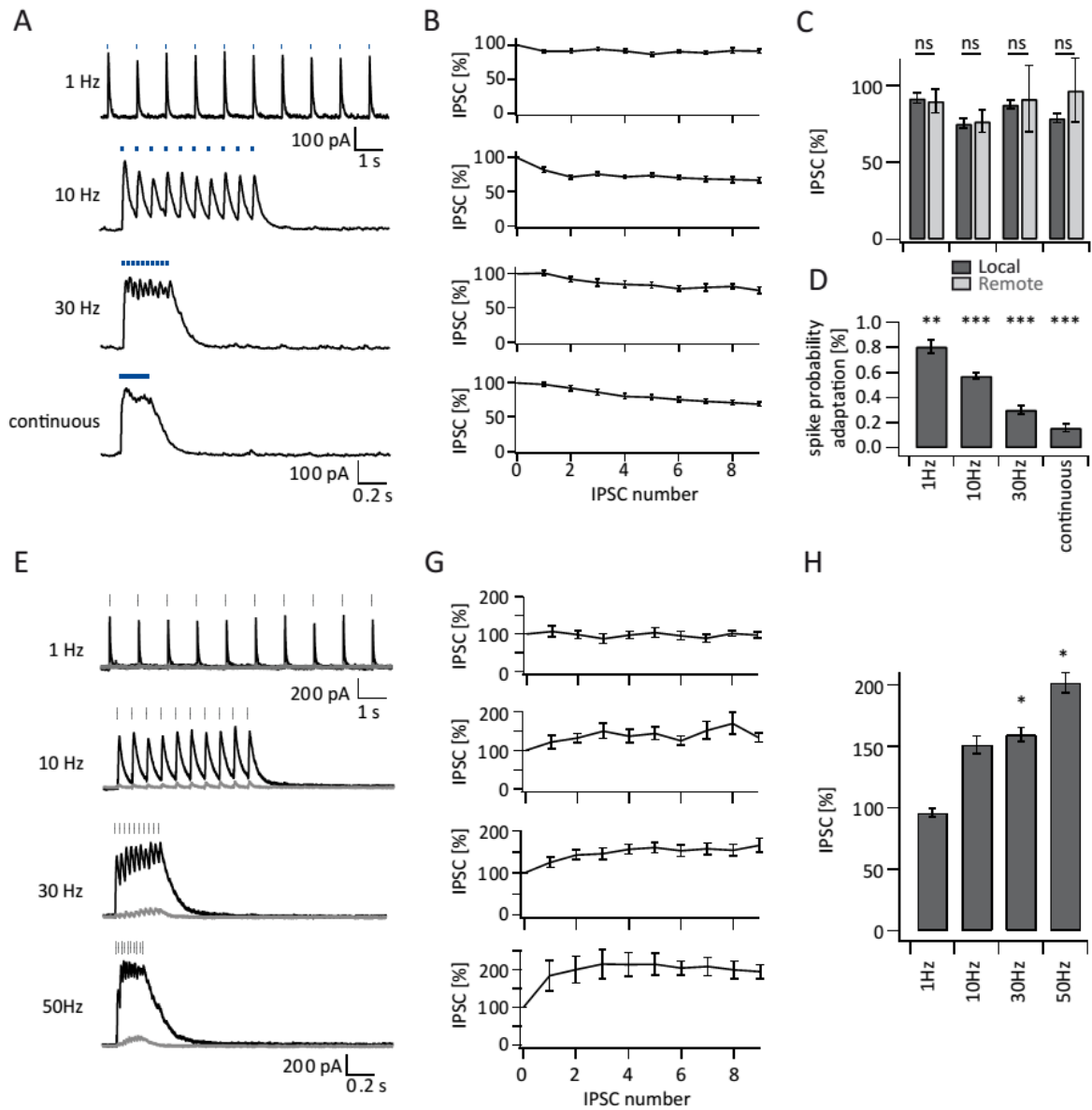


**Fig. 11) Frequency dependence of feedback inhibition,** Trains of 10 focal optic (A to D) or antidromic electrical (E to H) stimulations were applied to elicit feedback inhibition. **A)** Example traces for optic stimulation at 1, 10, 30 Hz or continuously for 200ms to a single site close to the recorded cell. **B)** Evolution of the peak IPSC amplitude during a train for each frequency. **C)** The mean of the last three IPSCs was normalized to the first. Comparison of local (dark grey) and remote (light grey) stimulation revealed no significant differences (two way ANOVA; Distance  $p = 0.491$ ). **D)** The spike probability due to an optic pulse decreased significantly during a train (one sample t-tests with Bonferroni correction; 1 Hz to 0.8,  $p = 0.006$ ; 10 Hz to 0.5,  $p < 0.0001$ ; 30 Hz to 0.3,  $p < 0.0001$ ; continuous to 0.2,  $p < 0.0001$ ). **E,G)** same as (A,B) but with antidromic electrical stimulation (black traces). Only cells in which IPSCs were blocked to  $<10\%$  with  $40 \mu\text{M}$  CNQX and  $50 \mu\text{M}$  D-AP-V (gray traces) were used ( $n=7$ ). **H)** The mean of the last three IPSCs was normalized to the first (one sample t-test with Bonferroni/Holm corrected p-values; 1Hz  $p = 0.651$ ; 10Hz  $p = 0.066$ ; 30Hz  $p = 0.019$ ; 50Hz  $p = 0.014$ ).

## 4. Discussion

Feedback inhibitory microcircuits are thought to perform the important functions of max pooling and assembly competition throughout the brain. In the present study I used a combination of electrophysiological, imaging and optogenetic techniques in order to quantitatively describe the recruitment of feedback inhibition in space and time in the dentate gyrus of the hippocampal formation.

### 4.1 Major Findings

I found that feedback inhibition is steeply recruited by sparse populations of GCs. The gain and sensitivity of the feedback inhibitory microcircuit are steepest at active cell fractions below 3 % and slowly decrease as more cells are activated. Inhibition saturates when approximately 4 % of GCs are active. This feedback inhibition is non-uniformly distributed over space with regard to its recruitment, amplitude and temporal properties. Local inhibition is recruited more steeply and has greater amplitude, shorter latency and faster kinetic properties than remote inhibition. Finally, in marked contrast to area CA1, net feedback inhibition facilitates during repetitive stimulation.

In the following I will first discuss the advantages and disadvantages of the experimental approaches taken here, including potential sources of variability and errors and some conceptual considerations (chapter 4.2). I will then proceed to discuss the individual findings and their potential implications (chapters 4.3 to 4.8).

### 4.2 Methodological Considerations

The quantification of the recruitment of feedback inhibition in this study is based on two complementary approaches. Firstly, GC APs were elicited electrically through antidromic stimulation while the activated GC fraction was assessed by population  $Ca^{2+}$  imaging. Secondly, GCs were activated optogenetically by focal laser stimulation while the active cell fraction was calculated from systematic cell-attached recordings. These approaches are

likely to differ with regard to the spatial and temporal properties with which the GC population is activated. This is important because both parameters may affect the recruitment of inhibitory interneurons. Additionally, each approach has particular sources of variability and errors with respect to the estimation of the activated cell fraction. In this respect, a general conceptual question is how to define the total population to which the population of active cells should be normalized. Functionally, any cell which is integrated into the feedback inhibitory circuit should be included in the total population. Anatomical findings indicate that most feedback inhibitory interneurons receive input from and project to a large number of granule cells over a large area (Acsády et al., 1998; Amaral et al., 2007), suggesting that the entire GC population within a hippocampal lamella might function as a unit (Andersen et al., 1971). Accordingly, most computational studies have assumed that all GCs within individual lamellae are integrated into the feedback inhibitory circuit (de Almeida et al., 2009; Myers and Scharfman, 2009). In the present study I followed this assumption for descriptive purposes and provided some evidence to support it, which will be discussed in chapter 4.4.

#### 4.2.1 Electrical Activation and Population $\text{Ca}^{2+}$ Imaging

Antidromic electrical stimulation is a standard electrophysiological technique which leads to highly synchronous activation of cells with short latency. Since the axons of the entire GC layer converge into a dense bundle at the electrical stimulation site in stratum lucidum, it can be furthermore expected to lead to cell activation spatially distributed throughout the GC layer. A caveat of electrical stimulation is that it is not selective for particular cell types. This is particularly problematic, because in the present study it was necessary to increase the stimulation power until saturation of the feedback IPSC was observed. However, especially the large stimulation currents required to produce a saturated IPSC often led to direct activation of interneurons. This was reflected by a component of the IPSC which was insensitive to the block of glutamatergic transmission. The problem was addressed by including only experiments in which a complete block of inhibitory currents by glutamatergic antagonists could be demonstrated (8 of 23).

Population  $\text{Ca}^{2+}$  imaging allows the monitoring of a large number of cells simultaneously, which is a distinct advantage over standard electrophysiological techniques. This is particularly important due to the sparse, spatially distributed population activity resulting from antidromic stimulation. Electrophysiological probing of a sufficient number of cells to detect the small, distributed population of responders within each individual section is not feasible. However, the quantification of the active cell fraction by population  $\text{Ca}^{2+}$  imaging is also accompanied by several caveats. Firstly, the cell fraction is estimated within a two dimensional field of view within a single sample plane. Due to methodological constraints, such as the maximal imaging depth and the required temporal resolution this plane could not be placed randomly. This is a significant source of variability due to the strict laminar organization of the mossy fiber tract. In fact, in sections which were not aligned to the MCP of the hippocampus the number of antidromically activatable cells within the sampling plane was close to zero whereas feedback inhibitory currents were always observed. While using only sections from the MCP (see methods chapter 2.2) partially addresses this problem, it remains a potential source of variability, because the slicing plane cannot be defined with high precision and animals are subject to anatomical variability. Secondly, the active cell fraction was calculated by normalizing to the total number of dye loaded cells present in the imaging frame. This tacitly assumes that the imaged population is representative of the entire GC population integrated into the feedback inhibitory circuitry. Conceptually, it raises the question how this feedback inhibitory circuitry is organized in space, which was addressed by the optogenetic experiments and will be discussed below.

A further potential source of error in the estimation of the active cell fraction is the presence of a small population of inhibitory interneurons within the GC layer. For the calculation of the cell fraction it was not possible to systematically distinguish between GCs and these interneurons. However, interneurons are generally located at the inner border of the GC layer and are usually twice as large as GCs. Neither of these traits was observed within the population of activated cells. Additionally, the sparsity of the interneuron population in the DG (approximately 0.5 - 1 %, Amaral, 2007) suggests that the contribution of activated interneurons to the estimated active GC fraction is small.

Note that most of the sources of error described above are likely to lead to an overestimation of the active GC fraction as reported in this study. Accordingly, the data should be regarded as an upper bound.

#### 4.2.2 Focal Optogenetic Granule Cell Activation

In contrast to antidromic electrical stimulation, focal optogenetic stimulation elicited GC activity which was spread over more than 10 ms in time, but was spatially localized. Since the illumination spot could be rapidly and precisely shifted, it was possible to determine how individual GCs responded to focal stimulations at multiple distances, revealing a detailed spatial activation profile for each sampled cell. This information could be used to calculate the firing probability of potential responders as a function of the distance from the stimulation spot. Together with measurements of the three dimensional profile of light intensity within the slice, it allowed the estimation of the total responding population for individual light pulses. In this approach, GC activation was sampled by cell-attached recordings in only a small number of cells in each slice. Nevertheless, the knowledge of how the activated cells are spatially distributed offers a distinct advantage over the electrical stimulation experiments. This information could also be used to estimate the firing probabilities of cells deeper within the slice. The calculation of the active fraction of cells now requires an explicit assumption about the total number of cells integrated into a feedback inhibitory circuit and their spatial distribution. As stated above, the cell fractions reported here rely on the assumption that all cells within the slice are integrated into the local circuit. The spatially defined activation of cells provided evidence justifying this assumption, which will be discussed in the chapter 4.4. Another difference between the two stimulation approaches is that during antidromic activation, responders will preferentially be cells with preserved axons. In contrast, during optogenetic stimulation, a portion of cells at the slice surface identified as responders may have severed axons.

In summary, the two experimental approaches are likely to differ in several important ways. While antidromic electrical stimulation is expected to produce synchronous but spatially distributed GC activation, optogenetic stimulation produces a relatively asynchronous and local GC activation. The fact that the results of both approaches are comparable suggests

that the recruitment of feedback inhibition is relatively robust towards variations of these parameters. Moreover, the two approaches act as controls for each other concerning the other potential sources of error mentioned above.

### 4.3 The Recruitment of Feedback Inhibition

Previous studies have begun to address the question of how feedback inhibition is recruited in other regions, investigating mainly the initial part of recruitment with up to three principal cells activated (Kapfer et al., 2007; Miles, 1990; Silberberg and Markram, 2007). Kapfer et al. (2007) additionally used their experimental data to model the recruitment of inhibition over a larger range of population activity (up to 20 cells). However, the question of how feedback inhibition is recruited over the entire range of population activity has to my knowledge never been empirically addressed before.

I found that feedback inhibition is recruited steeply by small percentages of GCs and saturates when around 4 % of GCs are active. Importantly, this was the case during spatially distributed but synchronous electrical population activation as well as during the spatially localized but more desynchronized optogenetic activation. This range corresponds well to the activity range of 0.1 to 4 % reported for GCs *in vivo* (Alme et al., 2010; Chawla et al., 2005; Jung and Mcnaughton, 1993; Leutgeb et al., 2007; Schmidt et al., 2012; see also section 4.3.1). The data further indicate that the gain and sensitivity of the inhibitory recruitment curve is very high at values below 3 % of active GCs and gradually decreases as more cells are activated. Accordingly, the feedback inhibitory microcircuit responds with high gain and sensitivity within the range of physiological GC activity, consistent with its purported functions of max pooling and assembly competition.

In this chapter I will discuss the findings of the present study in comparison to the studies mentioned above (sections 4.3.1 and 4.3.2). Additionally, I will compare the recruitment curve found here with that of a feedforward inhibitory circuit described by Pouille et al. (2009; section 4.3.3). It should be noted that the present study addressed only the recruitment of feedback inhibition within the local microcircuit (section 4.3.4).

#### 4.3.1 Comparison of the Active Cell Fraction between Studies

In the present study the active cell fraction was assessed as the population activated by a single electrical or optogenetic stimulus, in order to assess the ability of a ‘more or less’ synchronously activated GC population to recruit feedback inhibition (see chapter 4.2). It covers the temporal range between previous *in vitro* studies (Pouille et al., 2009) with near synchronous electrical stimulation and the less synchronous fundamental assembly window of 20 ms proposed by Buzsaki (2010). In both cases, the recruitment of feedback inhibition was tuned to a similar range, displaying maximum gain and sensitivity at active cell fractions below 3 % and saturating at approximately 4 %. This is in good accordance with the range of activity of GCs described *in vivo*. The estimates gained using immediate early gene studies and *in vivo* recordings range between 0.1 to 4 % (Aimone et al., 2011; Schmidt et al., 2012).

However, in order to compare the active cell fraction as assessed in the present study to estimates of GC activity *in vivo*, it is necessary to review the methodology with which this range was measured in previous studies. This is because the assessment of the active cell fraction is associated with specific biases for each experimental approach taken. Furthermore, while some approaches, such as immediate early gene studies generally report active cell fractions, *in vivo* electrophysiological studies report firing rates. How the two are related requires some theoretical consideration about the temporal window of assembly formation and competition. This will be only touched upon here and discussed in more detail in section 4.5.1.

In immediate early gene studies cell activity is typically integrated over time windows of several minutes, during which the animals explore an environment. However, this implies, that cells active at different time points may cumulate, leading to an overestimation of the active cell fraction (Guzowski et al., 1999). On the other hand immediate early gene studies will detect as active only a subset of cells undergoing the plasticity mechanism in which the gene under study is involved (Bramham et al., 2010; Guzowski et al., 2006). Precisely how different levels of activity in individual cells leads to immediate early gene expression is unknown, but it may well involve repeated firing, which would suggest that reported active cell fractions are underestimations. Furthermore, the population of cells expressing the respective gene is then typically normalized to the entire population of anatomically detectable cells in the principal cell layer. However, some of these cells may be GABAergic,

exclusively involved in unrelated functions, or may not be able to fire at all (Alme et al., 2010). This would again lead to an underestimation. Depending on the time window and behavioral task, the reported active cell fraction in immediate early gene studies of the DG varies between 0.1 and 5 % (Alme et al., 2010; Chawla et al., 2005).

By contrast, extracellular *in vivo* recordings can detect only cells which display a sufficiently high spiking activity. This is likely to bias cell detection toward the more active population of immature GCs. Cells which do not fire during the recording period cannot be detected. Furthermore, cells with an insufficient firing rate cannot be isolated from noise. Therefore the calculation of the mean firing rate combines the omission of insufficiently active cells from the denominator with the bias toward more active cells in the numerator. Accordingly, estimates gained with this method are likely to represent overestimations. Mean firing rates reported for dentate GCs in extracellular *in vivo* studies vary between 0.4 to 1 Hz (Alme et al., 2010; Leutgeb et al., 2007; Nitz and McNaughton, 2004).

Finally, a recent *in vivo* whole-cell patch-clamp study of morphologically identified mature GCs in awake, behaving animals reported a mean firing rate of approximately 0.25 Hz ranging between 0 and 0.6 Hz for individual cells (3/8 GC did not spontaneously fire within the > 15 min recording period but only during current injections). Interestingly, the majority of APs in the active GC subpopulation occurred as bursts (65 % of events). Though this approach is not subject to the biases described above, the technical challenges of obtaining long, stable, awake, *in vivo* recordings and the perturbation of the intracellular milieu may lead to alternate biases. Furthermore, the sample size is necessarily small.

As mentioned above a comparison of these firing rates to the cell fractions of immediate early gene studies requires an assumption about the temporal window of a functional cell assembly. For instance, if all cells fire on average at 1 Hz, then a temporal window of 20 ms is expected to contain on average 2 % active cells (see also section 4.5.1.).

#### 4.3.2 Recruitment of Feedback Inhibition with One to Three Principal Cells

Previous *in vitro* studies in different brain regions have reported that the activation of a single principal cell could elicit feedback inhibition in a simultaneously recorded second principal cell (Kapfer et al., 2007; Miles, 1990; Silberberg and Markram, 2007). Disynaptic feedback inhibition was observable in approximately 30 % of pairs in the guinea pig CA3 region (Miles, 1990) as well as the rat somatosensory cortex layer 5 (Silberberg and Markram, 2007) and 12 % of pairs in the rat somatosensory cortex layer 2/3 (Kapfer et al., 2007). By contrast, in the present study no case of single GC induced feedback inhibition was found in 11 GC pairs which were tested in a total of 15 directions. In this context it is noteworthy, that despite a substantial number of studies presenting data from simultaneously recorded pairs of GC and hilar interneurons, all of which characterize the interneuron input to GCs, reports of GC input to interneurons is remarkably scarce (Table 1; but see Geiger et al., 1997). A potential explanation would be a comparatively low connectivity from GC to interneuron with simultaneously high connectivity from interneuron to GC. The comparison should be viewed with caution due to differences in species and region. Nevertheless, it may reflect differences in the tuning of recruitment curves between these regions due to the specific requirements of the DG. For instance, in contrast to area CA3, GCs possess an extremely low intrinsic excitability and lack direct recurrent excitatory connections. Therefore, adding feedback inhibition when input strengths are very low may completely suppress sparse GC activity. Accordingly, very small numbers of GCs may be comparatively less efficient at recruiting inhibitory interneurons than other principal cells. A step function, in which the recruitment of feedback inhibition begins, only when a certain minimum active cell fraction is activated, would also be well suited to constrain the maximum active cell fraction, while simultaneously permitting unperturbed activity below this minimum.

In the neocortex, Kapfer et al. (2007) have characterized the initial part of recruitment (with only one to three cells active) as 'supralinear'. The authors estimate that the activation of an additional principal cell leads to a five-fold increase in the probability of feedback inhibition. This supralinearity results from the convergence of principal cells onto interneurons and the fact that two inputs are ten-fold more likely to depolarize the interneuron to threshold than one. The mechanism suggests that supralinear recruitment will occur whenever principal cell

input converges onto interneurons and individual principal cells do not generally depolarize their targets to threshold. Therefore it may well be a general phenomenon when only small numbers of principal cells are active. Although no supralinear phase of the recruitment of feedback inhibition was observed in the present study, this is very likely due to insufficient resolution of GC population activation with small GC numbers.

In order to address the question of how feedback inhibition is recruited when more than three cells are coactive, Kapfer et al. (2007) developed a model based on the experimentally determined connectivity and EPSP amplitudes in SST<sup>+</sup> interneurons, the subpopulation identified to mediate inhibition in their settings. In this model they explore the effects of the distribution of EPSP amplitudes in these interneurons on the sensitivity and gain of the feedback inhibitory circuit. They predict a half maximal activation of inhibition with approximately 10, and complete saturation with 20, active principal cells. By comparison, the half maximal activation of inhibition observed for GCs in this study was greater than 1 % of the total population independent of the experimental approach taken (up to 4 % in the case of exclusively remotely activated inhibition). Assuming that the entire GC population in a section comprises approximately 20000 cells (a rough estimate based on the mean cell size of OGB-1 loaded GCs and the total volume of the GC layer), 1 % translates to more than 200 GCs, an order of magnitude greater. Although, the model by Kapfer et al. addressed only one interneuron subtype and a different brain region than this study, the discrepancy highlights the necessity for more empirical data.

#### 4.3.3 Comparison of Feedforward and Feedback Inhibition

The recruitment curve for feedback inhibition determined in this study also differs markedly from a previously published recruitment curve for feedforward inhibition in the CA1 region (Pouille et al., 2009). While the present study found the complete saturation of feedback inhibition with around 4 % of the GC population active, Pouille et al. (2009) found a slow progressive increase of feedforward inhibition until approximately 40 – 50 % of the total input strength. The input strength in their study was measured by the slope of the field EPSP in the CA1 input area normalized to the slope observed during the maximal population spike amplitude. It is related to the fraction of active cells in the upstream population. This

upstream population encompasses all cells of which the output contributes to the downstream population spike. The differential recruitment curves in the two cases may reflect the different physiological activity ranges of the respective recruiting populations.

In their study, Pouille et al. went on to investigate the potential network function of feedforward inhibition. Their principal finding was that in this region feedforward inhibition leads to an increased dynamic range of the population response. In other words it allows individual cells to be recruited over a wider range of input strengths, in effect decreasing the gain of the population response curve and delaying its saturation. While this normalization allows differential responses to a larger range of input strengths, it does the opposite of the proposed role of feedback inhibition, which is to compress the population activation curve to a small range of active cell fractions. This contrast has been formalized by Olsen et al. (2010) in a simple model, based on the normalization equations by Carandini and Heeger (2012; see also Silver, 2010). Although this type of equation has been primarily used to model the firing rate of individual cells it can also be used to describe populations of cells (Busse et al., 2009). In their study Olsen et al. contrast feedforward mediated input normalization, which stretches the activation curve along the input axis, to feedback inhibition mediated output normalization, which compresses it along the output axis (**Fig. 12**). Depending on the physiological range of input strengths this can have diametric effects on the range of population activity, with feedforward inhibition expanding the range and feedback inhibition compressing it (**Fig. 12**).

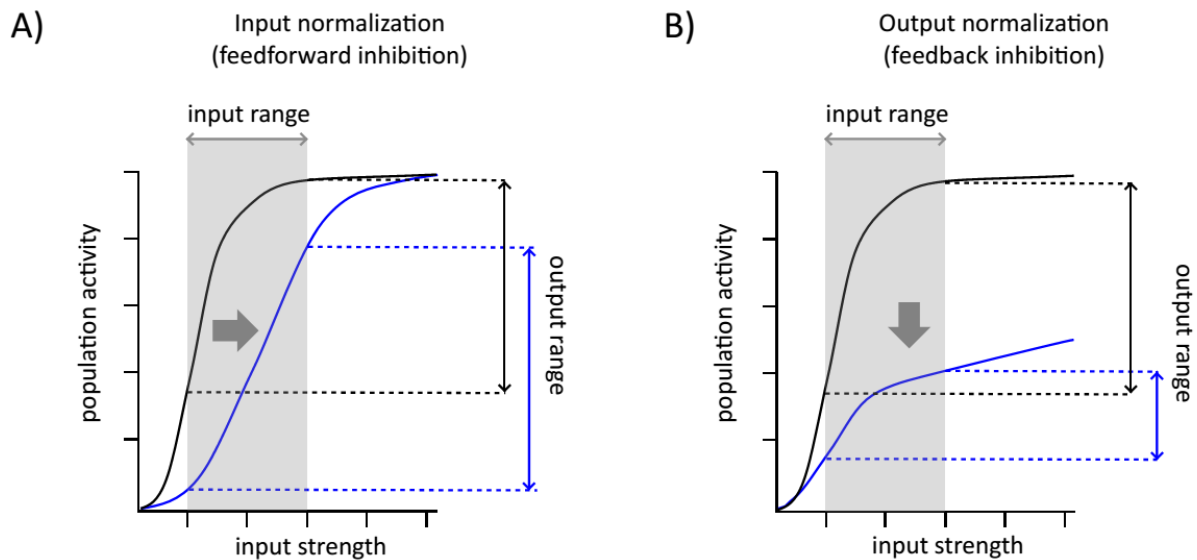


**Fig. 12, Feedforward and Feedback inhibition in a simplified model,** Schematic illustration of the differential effects of feedforward and feedback inhibition on the population activation curve based on the model proposed by Olsen et al. (2010). **A)** Feedforward inhibition is proposed to implement input normalization (grey arrow in A) stretching the curve along the input axis (blue curve in A). **B)** Feedback inhibition is proposed to implement output normalization (grey arrow in B) compressing the curve along the output axis (blue curve in B). In this model for a given range of input strengths (grey area in A and B) feedforward inhibition can expand the output range while feedback inhibition compresses it (compare the black and blue vertical bars in A and B).

Finally, note that the analysis of Pouille et al. (2009) relies on the synchronicity and short latency of an electrically elicited population spike to isolate feedforward inhibition from feedback inhibition. Since the entire principal cell population is activated within four to five milliseconds following the electrical stimulation, there is no time for feedback inhibition to take effect. It is important to realize, that the purported functions of feedback as well as feedforward inhibition will depend crucially on the temporal distribution of presynaptic inputs and population activity under physiological conditions. The implications of the timing of feedback inhibition will be discussed in more detail in chapter 4.5.

#### 4.3.4 Translamellar Feedback Inhibition

The present study described the recruitment of feedback inhibition in the intralamellar microcircuit of an acute slice. It is important to note, that this precludes the detection of translamellar feedback inhibition or other long range connections (Amaral et al., 2007; Freund and Antal, 1988; Jinde et al., 2012, 2013; Ribak et al., 1986; Sloviter and Brisman,

1995). Accordingly, the recruitment function described here applies only for the local microcircuit and should be regarded as a fundamental building block. *In vivo* it will be complemented by translamellar and other long range connections. How these fundamental building blocks are integrated and coordinated by such long range connections remains an important open question. The quantitative description of the local feedback circuit provided here will help to address this question. Furthermore, the observation of a spatiotemporally graded local feedback circuit, offers qualitatively new insights as will be discussed in the following chapter. Such insights can further inform future computational and empirical investigation of the macroscopically intact circuit.

#### 4.4 Spatial Distribution of Feedback Inhibition

The spatially restricted GC activation during focal optogenetic stimulation allowed the investigation of the spatial distribution of feedback inhibition within the transverse plane. It is important to ascertain that remote GCs are integrated into the local feedback inhibitory circuit, if they are to be considered part of the total population. The central finding in this respect is that every recorded GC received inhibition, no matter where in the slice other GCs were activated. Even if the optogenetically activated cells were at the most remote locations within the slice, approximately 30 to 40 % of inhibition remained. This was the case irrespective of the blade and location of the recorded GC. Thus, the entire population of GC within the slice can be regarded as integrated into a single feedback inhibitory circuit. This justifies the description of the fraction of active cells as a fraction of the total GC population in the slice as used here. However, feedback inhibition was found to be non-uniformly distributed over space within this circuit. This implies that the network is actually spatially weighted. Accordingly, more elaborate models, which differentially define the recruiting GC populations and the resulting spatial distribution of feedback inhibition, may add additional insights. In this chapter I will discuss the spatial distribution of feedback inhibition described in the present study (section 4.4.1) and its potential functional implications (section 4.4.2).

#### 4.4.1 Non-uniform Distribution of Feedback Inhibition

I found that GCs exert the largest inhibitory effect on cells within an approximately 300  $\mu\text{m}$  radius, while increasingly distant GCs receive progressively less inhibition. This spatial profile was observed largely independent of laser power. Importantly however, the recruitment of remote inhibition required a larger cell fraction for halfmaximal activation. This implies that the difference in amplitude between local and remote inhibition is even more pronounced in the subsaturation regime.

Note that during stimulation at the very edge of the GC layer fewer cells can be activated, since part of the light cone will be beyond the GC layer. At the smallest power at which the IPSC was saturated ( $P = 3$ ) the active cell population spanned an approximately 300  $\mu\text{m}$  region of the GC layer (FWHM of a Gaussian fit: 240  $\mu\text{m}$ ; see Fig. 7B). This implies that the decrease of inhibition at the very edge of the GC layer is at least partially due to the decrease in the activatable population size rather than other spatially organized properties, especially for high powers. However, the monotonous decrease in the amplitude of inhibition with increasing distance was also consistently observed if the entire active GC population was well within the blade (**Fig. 10B – E**).

The latencies and kinetic properties of inhibition also differed markedly between local and remote stimulation and as a function of laser power (**Fig. 10J – M**). However, the temporal IPSC properties are expected to depend on the temporal distribution of GC population activation. While this distribution is identical when comparing local and remote inhibition at individual powers, it changes with increasing laser power (**Fig. 7**). Therefore the temporal changes in IPSC properties between laser powers must be interpreted with caution. Nevertheless, local and remote inhibition differentially evolve with increasing laser power, indicating that factors beyond the change in the temporal distribution of GC population activation must play a role. This clearly shows that the properties of feedback inhibition in a given GC depends on both, the spatial distribution of the recruiting GC population, and its size. Together these findings demonstrate the presence of a spatiotemporally graded inhibitory microcircuit.

Spatiotemporally graded inhibition has recently been described in detail for individual perisomatically inhibiting fast-spiking interneurons within the DG (Strüber et al., 2015). The

authors describe a spatial gradient of presynaptic release probabilities as well as postsynaptic GABA<sub>A</sub> receptor subunit composition. This leads to a decreased amplitude, an increased latency and slower kinetics of IPSCs at more remote synapses, strongly reminiscent of the observations presented in the present study. However, the connection probability of individual fast spiking interneurons to target GCs decreased to zero within approximately 300  $\mu\text{m}$  from the soma (Strüber et al., 2015). By comparison the distance dependent changes described here were observed along the entire length of the GC layer (~up to 1200  $\mu\text{m}$  from the recorded cell). Moreover, the range of latencies and kinetic properties observed by Strüber et al. differ markedly from those observed here.

Therefore the distance dependent changes in inhibition over the entire GC layer must also depend on other factors, such as the distribution of the GC axonal arbor and/or the anatomical organization of the feedback inhibitory microcircuitry. Accordingly, this study adds to the findings of Strüber et al. in several important ways. Firstly, the spatiotemporal grading of unitary IPSCs, described for fast spiking interneurons, is conserved and expanded when the entire feedback inhibitory network, with all participating interneurons, is activated. Secondly, the spatial gradient observed in the monosynaptic interneuron-GC connection is preserved and expanded in the disynaptic GC-interneuron-GC feedback circuit. Accordingly, the microcircuit motif of spatially graded inhibition must be supported by both arms of the inhibitory feedback loop. How exactly the feedback inhibitory microcircuit may bring forth the observed characteristics will be discussed in detail in section 4.6.1.

#### 4.4.2 Functional Implications

What is the function of the spatially graded feedback inhibition? In their study of fast spiking DG interneurons, Strüber et al. explore the impact of non-uniform inhibition in a computational network model containing rhythmically and synchronously active fast-spiking PV<sup>+</sup> interneurons. They find that networks with distance dependent inhibition improve the entrainment of principal cell populations in the gamma range. This is essentially because in networks with non-distance dependent inhibition, the IPSCs of interneurons at different distances from the target GC have different axonal conductance times, producing a temporally imprecise compound inhibitory conductance. In contrast, when the same total

inhibitory conductance is modelled in a distance dependent manner, the major inhibitory contribution for each target GC is from an interneuron in close proximity, thereby decreasing the jitter due to axonal conductance delays. The resulting compound inhibitory conductance is stronger and sharper leading to increased GC synchronicity. This result is predicated on the relatively strong assumption of complete synchronicity in interneuron activity, which may in part rely on the finding by Bartos et al (2002) that a large percentage of BC-BC pairs are electrically coupled. The strong degree of electrical coupling was found to lead to a near synchronous activation of interneuron pairs and an increased ability of the network to produce gamma oscillations. However, such substantial electrical coupling has not been reported in subsequent work (Larimer and Strowbridge, 2008; Savanthrapadian et al., 2014). The differential latencies between local and remote inhibition found in this study are also inconsistent with a high degree of electrical coupling between BCs. Nevertheless, under the assumption of a sufficient degree of interneuron synchronicity in the DG, my findings are consistent with the proposed function described by Strüber et al. (2015). Accordingly, spatially graded inhibition would lead to increased GC synchronicity. It remains to be shown whether this represents a physiologically significant mechanism.

As mentioned above, I found that not only the output of interneurons is spatially graded, but also their activation. In other words, interneurons which supply inhibition to different portions of the GC layer can be independently activated by local GC populations. This would be highly relevant if synchronously activated populations of GCs were locally clustered. Localized inhibition would then have an equalizing effect on the active cell fraction across space, in effect moving all portions of the GC layer closer to the optimal active cell fraction (see section 1.1.2). The portion of the DG receiving more input would also receive more feedback inhibition, thereby more effectively reducing the active cell fraction compared to the portion of the DG receiving less input. Assuming that the total inhibitory conductance available in the DG is fixed, such a local allocation of inhibition would increase the pattern separation ability by means of a more efficient regulation of the active cell fraction. Additionally, competition between active GCs would be most intense locally which may play a role in shaping the spatial distribution of individual assemblies. Interestingly, an increased spatial clustering of active granule cell ensembles has recently been described during spontaneous activity in a model of temporal lobe epilepsy (Feldt Muldoon et al., 2013). Moreover, the superior and inferior blade of the DG are known to be differentially active,

with inferior GCs displaying much lower levels of activity (Alme et al., 2010; Chawla et al., 2005). The spatial gradient of inhibition may allow for independent processing of the two blades despite this differential activity.

Finally, the localized application of inhibition only where it is needed will increase the energy efficiency of the network. Firstly, inhibition is supplied by interneurons, which have to generate AP and release GABA, all of which requires energy. Secondly, localized application of inhibition is likely to entail greater overall GC sparsity, thereby reducing energy consumption due to GC spiking. This is because current evidence indicates that inhibition in GCs is at least partially divisive, i.e. applying the same inhibition to a population with greater mean input leads to a stronger reduction of that input (Silver, 2010; Temprana et al., 2015; Wilson et al., 2012). Allocating inhibition preferentially to more active sections of the GC layer will accordingly cause greater overall sparsification. Additional functional implications arise from the differential time courses of inhibition across space as will be discussed in the next chapter.

## 4.5 The Time Course of Feedback Inhibition

So far, I have discussed mainly the spatial aspects of feedback inhibition, mostly neglecting the temporal dimension. However, the time course of feedback inhibition and its temporal evolution during trains of activity are evidently important for its ultimate function. Unfortunately, our knowledge concerning the temporal windows of assembly representation and competition remains limited. Nevertheless, an understanding of the possible implications of the time course of inhibition onto the proposed information representation by sparse GC assemblies requires consideration of these temporal windows (see chapter 1.1). In the following chapter, I will introduce some considerations about the temporal structuring of neural activity proposed by Buzsaki (2010) and discuss the temporal aspects of the present findings mainly in this context (section 4.5.1). I will then extend this reasoning to the evolution of feedback inhibition during trains of activity (section 4.5.2).

#### 4.5.1 The Temporal Window of Assembly Competition

It is common in computational models to simplify the temporal dimension by discretizing time. The winner-take-all rule is then applied by calculating the pre-inhibition population activity, the resulting inhibition, and the inhibition-corrected population activity in a single discrete time step (Binas et al., 2014; Myers and Scharfman, 2009; Rolls and Treves, 1998; Trappenberg, 2010). In physiological neural networks however, the feedback inhibition elicited by any group of principal cells must by definition occur with a delay. The implication is that the 'winning' cell assembly must not only receive stronger inputs than its competitors, but must also precede them by at least this delay period. This raises the question of the relevant time window for individual assemblies and assembly competition. György Buzsáki (2010) suggested a 'neural syntax' in which a 'fundamental assembly window' lasts approximately 20 ms, based on the integration time of EPSPs in postsynaptic neurons, the gamma-oscillation and the timeframe for STDP (Lin et al., 2006). He further proposed that combinations of such fundamental assemblies could be linked together in 100 to 200 ms time windows based on the observation of gamma-nested-theta oscillation and the timescale of place cell assemblies in CA1 (Geisler et al., 2007; Maurer et al., 2006). Further network oscillations may serve to form different types of assemblies or additional hierarchical levels. The ultimately relevant parameter for the temporal window of assemblies and assembly-competition in this view, is the reader mechanism, in our case the CA3 attractor network (Buzsáki, 2010). More precisely, since the DG pattern separation mechanism is thought to act mainly during encoding, it is the time window required for recurrent CA3 networks to undergo plasticity (Kheirbek et al., 2013; Lee and Kesner, 2004).

Based on these considerations, feedback inhibition may contribute to the regulation of fundamental cell assembly size, especially through the activation of fast-spiking interneurons (Bartos et al., 2002; Chrobak and Buzsáki, 1995; Pernía-Andrade and Jonas, 2014). In fact, a recent model addressed how fast, rhythmic gamma-frequency feedback inhibition may implement a type of 'k-winners-take-all' operation, termed 'E %max winner-take-all' (de Almeida et al., 2009). This model suggests, that rather than determining a certain fixed fraction of 'winners', the network might select all cells with excitation above a certain fraction of the maximal excitation. Interestingly, in their model that fraction is determined by the ratio of the delay of feedback inhibition and the membrane constant. In the present

study, as well as Strüber et al. (2015), the delay of feedback inhibition was found to be non-uniformly distributed over space. The potential implication is that the effect of feedback inhibition decreases with distance not only due to the decreased amplitude but also due to the increased delay. It is important to realize that the inhibition described by Strüber et al. (2015) and modelled by de Almeida et al. (2009) is exclusively the extremely fast inhibition mediated by fast spiking basket cells. Accordingly inhibition reaches its maximum within several milliseconds and completely decays within 20 ms. This timeframe is based primarily on the observations between individual GC-BC pairs (Geiger et al., 1997; Kraushaar and Jonas, 2000) and the understanding that these cells can generate gamma oscillations (Bartos et al., 2002, 2007). In fact, recent whole-cell patch-clamp recordings in awake animals have demonstrated gamma coherence of IPSCs and GC spiking, consistent with a physiological role of such fast mechanisms (Pernía-Andrade and Jonas, 2014).

The optogenetic activation spread within a 10 to 20 ms window as used in the present study might be viewed as mirroring the population activation within a fundamental assembly window. The ensuing postsynaptic inhibitory conductance elicited by the entire feedback inhibitory network lasted for as long as 100 ms (with a half width of approximately 40 ms) most likely because a variety of interneuron types with differing kinetic properties are non-synchronously activated (Hefft and Jonas, 2005; Savanthrapadian et al., 2014; see also section 4.6.1). This suggests that another relevant time scale is that of a theta cycle. Especially inhibition at remote sites, which occurs between 5 and 10 ms later than local inhibition, may act at theta rather than gamma scales. According to the suggested neural syntax, this would imply that early fundamental assemblies within a theta cycle suppress those which would otherwise occur later, in effect max pooling in time (Buzsáki, 2010). From the perspective of CA3, this would prohibit the synaptic association of fundamental assemblies at different phases of a theta cycle. *In vivo* evidence indicates that the entorhinal input to GCs is theta modulated while the spiking activity of GCs is theta as well as gamma modulated, consistent with the view that dentate GC activity is temporally structured according to theta and gamma cycles (Pernía-Andrade and Jonas, 2014).

#### 4.5.2 Facilitation of Net Feedback Inhibition

Antidromic electrical stimulation revealed that net feedback inhibition arriving at GCs during trains of activity facilitates. Moreover, the optogenetic experiments suggest that during a train of activity, progressively smaller GC populations are required to maintain the same level of inhibition. This differs starkly from area CA1, where feedback inhibition elicited by antidromic electrical stimulation strongly depresses (Pothmann et al., 2014; Pouille and Scanziani, 2004). Net facilitation of feedback inhibition is likely to further enhance the max pooling functionality in time. This may reflect the specific requirement of sparsity over space and time of GC population activity, as opposed to CA1. Furthermore, the facilitation is maintained over the entire course of a train, suggesting that the max pooling functionality can be partially extended to such long time frames. The fact that disynaptic feedback inhibition displays robust facilitation is particularly interesting in light of the numerous studies describing strong depression of interneuron input to GCs (Table 1). How the feedback inhibitory microcircuitry may bring forth these temporal properties as well as the spatial properties described above will be discussed in the following chapter.

#### 4.6 Implications for the Local Feedback Inhibitory Microcircuitry

I have discussed distinctive spatial and temporal features of feedback inhibition in the DG and their possible functional roles. But how does the feedback inhibitory microcircuitry give rise to these properties? Both spatial and temporal features of inhibition are determined by at least three fundamental components: First, the spatial and temporal organization of mossy fiber input onto the population of feedback inhibitory interneurons (including mossy cells); second, the connectivity and temporal properties between, and the intrinsic properties of, these interneurons; and third, the spatial and temporal organization of the outputs of these interneurons. In this chapter I will first summarize the inferences which can be made from the data presented here and propose two simple models of the feedback inhibitory microcircuit which can explain the observed spatiotemporal distribution of feedback inhibition (section 4.6.1). I will then discuss how net facilitation of feedback inhibition during trains of input may arise (section 4.6.2). In order to place these

considerations in context it should also be noted that physiologically, feedback inhibition acts not in isolation but in close coordination with feedforward inhibition (section 4.6.3).

#### 4.6.1 Spatial Distribution of Feedback Inhibition

How could the observed spatiotemporal properties of feedback inhibition be implemented by the local microcircuit? Since both the axonal distributions of GCs and the various interneuron types as well as their dendritic distributions play a role, there are various ways to achieve the observed effects. The spatial features may in part be due to the spatially graded output of individual interneurons (Strüber et al., 2015). Additionally, the distinct morphologies and synaptic properties of different interneuron types could account for the observed distribution (Harney and Jones, 2002; Hosp et al., 2014; Savanthrapadian et al., 2014; see section 1.5.2 for an overview of DG interneurons). Moreover, interconnections within the feedback inhibitory microcircuitry, for instance inhibition of interneurons responsible for different sections of the DG could play a role (Savanthrapadian et al., 2014; Tyan et al., 2014).

A number of inferences about the anatomical connectivity can be made from the data described in the present study. Firstly, since local GC activation leads to locally focused GC inhibition, some interneurons must have not only spatially tuned output, but also spatially tuned input. In other words, interneurons mediating local inhibition must also be preferentially innervated by local GC. A second inference can be made by comparison of the different stimulation paradigms. Since global optogenetic and electrical stimulation activate local as well as remote GCs these types of stimulation should also elicit combined local and remote inhibition in the recorded GC. However, the amplitude of the maximal optogenetic IPSC, elicited by local stimulation, did not increase further during global optogenetic or electrical stimulation. Since remote activation does produce local inhibition, this must be because the 'remote inhibition mediating' population is also already activated by local stimulation. Further inferences can be drawn from the fact that remote inhibition occurs up to 10 ms later than local inhibition and has distinct kinetic properties. In the following I will describe the two simplest models which could bring forth these properties (**Fig. 13**).

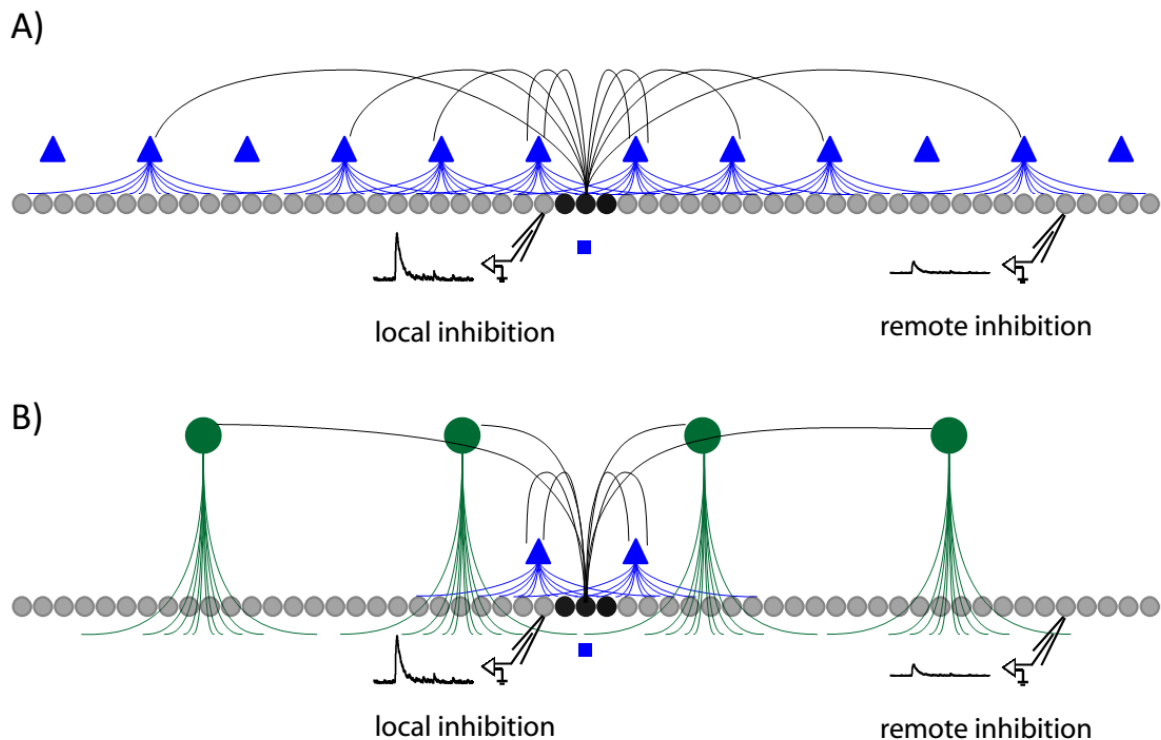


**Fig. 13, Two simple circuit motifs which could underlie the spatiotemporal distribution of feedback inhibition, A)** The most parsimonious model to explain the differential amplitude, delay and kinetics of local and remote inhibition requires only one type of interneuron, where the connection probability from GC to interneurons decreases with distance. **B)** A slightly more complex model includes two different interneuron types which are differentially involved in mediating local and remote inhibition. The stimulation site is illustrated by a blue square, active GCs and mossy fibers by black circles and lines respectively and inactive GCs by grey circles. Interneurons are illustrated as either blue triangles or green circles with respectively colored lines as axons.

The most parsimonious model which could explain the observations outlined above contains only BCs with spatially graded output as described by Strüber et al. (2015) which are innervated by mossy fibers in a spatially graded manner (**Fig. 13A**). In this model the reduced amplitude of remote inhibition would be implemented primarily by a distance dependent decrease in the connection probability between mossy fiber axons and BCs. The increased latency, higher jitter and slower time course of remote inhibition could be caused by a decreased connectivity to BCs, leading to an increased duration until remote interneurons are brought to threshold, combined with spatially graded BC output (Kress et al., 2008; Strüber et al., 2015). Importantly, due to the curvature of the DG the increasing ‘functional’ distance along the GC layer does not correspond to increasing geometrical distance. Yet, in the present study inhibition decreased monotonically with increasing ‘functional’ distance along the contralateral blade, even if all the stimulation spots involved were geometrically

equidistant. This may reflect the anatomical organization of processes of PV<sup>+</sup> perisomatically inhibiting interneurons along the GC layer (Amaral et al., 2007; Hosp et al., 2014). The axonal tree of these cells is restricted largely to the GC layer, spreading out along its length. Furthermore, the connection probability and IPSC amplitude in GCs, decreases with increasing distance from the interneuron soma (Strüber et al., 2015). Additionally, the dendrites of these cells within the hilus often appear rather restricted, consistent with predominantly local activation (Hosp et al., 2014).

However, in light of the presence of multiple DG interneuron types, which are innervated by mossy fibers, it seems unlikely that the effects are carried only by BCs. Interestingly, many dendritically targeting interneurons show longer latencies and slower kinetics than somatically targeting interneurons, suggesting that the spatial variation of IPSC kinetics found here might in part reflect different contributions of these interneuron classes (Harney and Jones, 2002; Hefft and Jonas, 2005; Liu et al., 2014). Notably, HIPP like cells frequently display dendritic trees spanning large parts of the hilus, consistent with activation more independent of GC location (Hosp et al., 2014; Zhang et al., 2009). Moreover, their axons cover a significantly larger area, often spanning large parts of the DG ML (Hosp et al., 2014). Accordingly, in the second most parsimonious model, fast, local inhibition would be mediated by perisomatically inhibiting interneurons such as basket cells, while remote inhibition would be mediated predominantly by dendritically inhibiting interneurons (**Fig. 13B**).

Additional models may incorporate mossy cells as well as additional interneuron types. The anatomical integration of these cell types into feedback circuit suggests that they do play a role. However, given the sparsity of data as to their precise connectivity and its spatial distribution, I will refrain from speculation about this role (but see Larimer and Strowbridge, 2008). Accordingly, the presented models should be viewed as possible microcircuit motifs, which may well act together and in cooperation with additional elements. Especially mossy cells are likely to contribute to the feedback inhibitory microcircuitry since they can not only activate GCs but also hilar interneurons, leading to GC inhibition (Larimer and Strowbridge, 2008; Scharfman, 1995; see also section 1.5.2). Given the difference in latencies between local and remote inhibition (up to 10 ms), the involvement of mossy cells as a relay conveying remote inhibition would also be plausible (Larimer and Strowbridge, 2008).

	From	To	IN location	Method	Freq.	short term dynamics	pulses	species	Authors	
GC to IN e-stim to IN	GC	BC	GC-border	dual patch	50 Hz	PPD	2	juv. wistar rats	Geiger and Jonas (1997)	
	PP & C/A	FS	GC-border	e-stim/ spike prob.	50 Hz	decreased spike prob.	10	juv. SD rats juv. C57/BL6	Liu et al. (2014)	q
	PP	FS	GC-border	e-stim	10 Hz	depression to 40%	20	mice	Ewell and Jones (2010)	q
	PP & C/A	non-FS	GC-border	e-stim/ spike prob.	50 Hz	increased spike prob.	10	juv. SD rats	Liu et al. (2014)	q
	PP & MF	FS	GC-border	e-stim	30 Hz	facilitation		juv. wistar rats	Sambandan et al. (2010)	
	MF	FS	GC-border	e-stim (close)	30 Hz	facilitation, PPF		juv. wistar rats	Dasgupta et al (2015)	
e-stim to MC	MF	MC	Hilus	e-stim	20 Hz	facilitation to 500%	5	juv. wistar rat	Lysetskiy (2005)	q
IN to GC	BC	GC	GC-border	dual patch	10 & 50 Hz	depression to ~25% & 0%	> 850	juv. wistar rats	Kraushaar and Jonas (2000)	q
	CCK & PV	GC	GC-border	dual patch	50 Hz	depression to 20%	10	juv. wistar rats	Hefft and Jonas (2005)	q
	SST	GC	Hilus	dual patch	50 Hz	depression to 20%	20	adult GIN mice juv. C57/BL6	Zhang et al. (2009)	q
	BC	GC	GC-border	dual patch	20 Hz	PPD to 39%	2	mice	Bartos et al. (2002)	q
	FS	GC	GC-border	dual patch	10 Hz	PPD to 85%	2	juv. SD rats	Harney and Jones (2002)	q
	non-FS	GC	GC-border	dual patch	10 Hz	PPD to 77 %	2	juv. SD rats juv. C57/BL6	Harney and Jones (2002)	q
	PP	GC	GC-border	e-stim	10 Hz	depression to 40%	20	mice	Ewell and Jones (2010)	q
	FS	GC	GC-border	dual patch	25 Hz	depression	5	juv. SD rats	Liu et al. (2014)	
	non-FS	GC	GC-border	dual patch	25 Hz	facilitation	5	juv. SD rats	Liu et al. (2014)	
IN to IN	BC	BC	GC-border	dual patch	50 Hz	depression to 50%	10	juv. wistar rats	Savanthrapadian et al. (2014)	q
	HICAP	HICAP	GC-border	dual patch	50 Hz	facilitation to 160%	10	juv. wistar rats	Savanthrapadian et al. (2014)	q
	HIPP	HIPP	GC-border	dual patch	50 Hz	facilitative envelope	10	juv. wistar rats	Savanthrapadian et al. (2014)	q
	HICAP	BC	GC-border	dual patch	50 Hz	no change	10	juv. wistar rats	Savanthrapadian et al. (2014)	q
	HIPP	BC	GC-border	dual patch	50 Hz	no change	10	juv. wistar rats juv. C57/BL6	Savanthrapadian et al. (2014)	q
	BC	BC	GC-border	dual patch	20 Hz	PPD to 26%	2	mice	Bartos et al. (2002)	q
	TML (non-FS)	TML	GC-border	dual patch	50 Hz	facilitation , PPF to ~220%	8	adult wistar rats	Yu et al. (2015)	
	IN	IN	Hilus	dual patch	20 Hz	PPD to ~80%	2	juv. SD rats	Larimer and Strowbridge (2008)	q
MC	IN	MC	Hilus	dual patch	20 Hz	PPD to ~80%	2	juv. SD rats	Larimer and Strowbridge (2008)	q
	MC	IN / MC	Hilus	dual patch	20 Hz	no change	2	juv. SD rats	Larimer and Strowbridge (2008)	q
other	MF	IN	CA3	e-stim	20 Hz	facilitation	5	juv. SD rats	Toth et al. (2000)	q
		IN	CA3	e-stim	20 Hz	depression	5	juv. SD rats	Toth et al. (2000)	q

**Table 1, Literature on the short term dynamics in the DG microcircuit.** Overview over studies reporting on the short term dynamics of postsynaptic events, with potential relevance for the feedback inhibitory microcircuit. Cell identification was variably based on electrophysiological properties, marker expression, or morphology. Cells were activated either by whole-cell current injections or extracellular electrical stimulation. Please refer to the respective original studies for more details.

cells		other	
BC	basket cell	blue	depression, quantitatively described
CCK	cholecystokinin expressing cell	green	facilitation, quantitatively described
FS	fast spiking cell (> 50Hz peak firing frequency)	PPD	paired pulse depression
GC	granule cell	PPF	paired pulse facilitation
HICAP	hilar commissural/associational path associated cell	e- stim	extracellular electrical stimulation
HIPP	hilar perforant path associated cell	C/A	commissural/ associational
IN	not further categorized interneuron	MF	mossy fiber
MC	mossy cell	PP	perforant path
non- FS	non- FS (< 50Hz peak firing frequency)	SD rat	sprague dawley rats
SST	somatostatin expressing cell	juv.	juvenile (12 to 25 days postnatally)
TML	total molecular layer cell	q	quantitatively described

#### 4.6.2 Short Term Dynamics of Feedback Inhibition

Net facilitation in the DG could similarly be due to a number of different microcircuit mechanisms including the dynamics at any of the three fundamental components described above (section 4.6). Interestingly a number of previous investigations into the short term dynamics at different synapses within the feedback inhibitory circuit showed widely varying results (Table 1). Most notably, paired recordings between most known interneuron types and GCs quantitatively show depression of the GC IPSC during repetitive stimulation (Bartos et al., 2002; Harney and Jones, 2002; Hefft and Jonas, 2005; Kraushaar and Jonas, 2000; Zhang et al., 2009). This suggests that a particularly strong facilitation must arise at an upstream step of the feedback circuit. Unfortunately, despite this wealth of dual recording studies, I could not find any report which quantitatively described the short term dynamics of GC inputs onto any hilar interneuron type (but see Geiger et al. 1997). However, a recent study by Liu et al. (2014) reports an increase in spiking probability during trains of perforant path or commissural/associational stimulation in non-fast spiking but not fast spiking interneurons. Anatomical analysis of non-fast spiking interneurons revealed, that they are constituted mainly by HIPP and HICAP cells while fast-spiking cells represent predominantly BCs. Although they did not differentiate between feedforward and feedback inhibition, the timing of spikes suggests that they at least partially reflect feedback activation. In analogy to Pouille et al. (2004) they term the non-fast spiking cells 'late onset'. By contrast, the authors found that fast spiking BCs responded only during the initial pulses of the train, and were accordingly labeled 'early onset cells'. In addition to the increased recruitment of non-fast spiking interneurons, paired recordings revealed that they also display increased release

probability and an increase of the readily releasable pool during stimulation trains. These results suggest increased activation and output of non-fast spiking interneurons as a source of increasing feedback inhibition during trains of stimulation. Additionally, a number of studies report or show trains of depressing or facilitating input to GCs or hilar interneurons but do not describe these quantitatively, making any interpretation difficult (Table 1; Dasgupta and Sikdar, 2015; Geiger et al., 1997; Sambandan et al., 2010). The facilitation of net feedback inhibition may also be partially due to interactions between interneurons in the DG (Larimer and Strowbridge, 2008; Savanthrapadian et al., 2014; Yu et al., 2015). For instance, BC-BC synapses depress rapidly (Savanthrapadian et al., 2014). Finally, mossy cells receive strongly facilitating input from GCs and might act as a boosting relay for inhibition during trains of activity (Lysetskiy et al., 2005). In light of the mostly depressing dynamics in the majority of the previously reported connections within the circuit, the mossy cell input is perhaps the most promising candidate as a source of the net facilitation of feedback inhibition in the DG.

#### 4.6.3 Cooperativity between Feedforward and Feedback Inhibition

Experiments by Ewell et al. (2010) revealed that PV<sup>+</sup> BCs are efficiently recruited by perforant path stimulation. Moreover, when stimulated with trains at 10 Hz but not at other frequencies these cells displayed bursts of APs in which the later spikes were elicited by mossy fiber feedback input. Although these experiments demonstrate a frequency dependent contribution of BC to feedback inhibition, they also suggest that BC may be most efficiently recruited by combined feedforward and feedback input. Indeed, a study by Sambandan et al. (2010) demonstrated that PV<sup>+</sup> BC display preferential recruitment during precisely timed activation of the perforant path and mossy fiber input at a 10 ms interval. Moreover, this coactivation can lead to associative LTP at MF synapses strengthening the feedback activation of these interneurons. It should be noted, that these studies relied on electrical stimulation in the ML and it is therefore possible that they stimulated not only perforant path fibers but also other fibers. Nevertheless, it is important to remember that feedback inhibition does not act in isolation but in tight coordination with feedforward inhibition.

## 4.7 Role of immature GCs

In the present study I have not addressed the role of adult neurogenesis despite the fact that it is considered to be important in the process of pattern separation (Alonso et al., 2012; Clelland et al., 2009; Sahay et al., 2011). Immature GCs are thought to play a special role in DG processing which partially exempts them from feedback inhibition mediated max pooling and assembly competition (Aimone et al., 2011; Li et al., 2012; Marin-Burgin et al., 2012; Temprana et al., 2015). Although the present study has accordingly concentrated solely on inhibition in mature GCs, the results need to be viewed in the context of the contribution of immature GC in order to better understand the implications for pattern separation.

### 4.7.1 The Temporal Tag Hypothesis

The temporal tag hypothesis posits that adult born, immature GCs come to represent contexts or patterns, which the animal is exposed to during a 'critical period' in their maturation (Ge et al., 2007; Kee et al., 2007; Tashiro et al., 2006, 2007). Several studies combining functional *in vitro* data with computational models support this general hypothesis (Li et al., 2012; Marin-Burgin et al., 2012; Temprana et al., 2014; but see Alme et al., 2010; Nakashiba et al., 2012). For instance Temprana et al. (2014) show that immature GCs are incompletely integrated into the feedback network both in terms of their output as well as their input. They argue that the low inhibition and high intrinsic excitability of young adult born granule cells enables them to initially broadly respond to new stimuli. Progressive coupling to feedback inhibition and changes in intrinsic properties then slowly decrease the size of the input field. At the same time Hebbian learning occurs, ultimately allowing the cell to retain a small specific input field. Accordingly, feedback inhibition implements its full canonical functions primarily in mature GCs, while it appears to serve more complex functions during the maturation of new born GCs (Espósito et al., 2005; Ge et al., 2006; Li et al., 2012).

#### 4.7.2 Rate Coding or Population Coding

The fact that immature GCs display much higher firing rates and little response selectivity is inconsistent with the classical theory of pattern separation by sparse population coding (Aimone et al., 2011; Alme et al., 2010; Espósito et al., 2005; Ge et al., 2007). Instead, a comparatively small subpopulation of GCs recorded *in vivo* have displayed relatively unselective responsivity and have been shown to perform pattern separation by rate coding rather than population coding (Leutgeb et al., 2007). Some authors have, rather radically, interpreted the relative quiescence of the majority of GCs *in vivo* to indicate that they ‘opt for early retirement’, that is, no longer contribute to coding (Alme et al., 2010). However, it should be noted that the methodology used for studying *in vivo* activity is biased toward more active GCs since cells with low activity levels are less likely to be successfully isolated from extracellular recordings or to express immediate early genes (Alme et al., 2010; Leutgeb et al., 2007; see also section 4.3.1). Therefore the finding that pattern separation is mediated by rate coding of only a small subset of GC rather than the entire population may be partially due to a preselection of cells implicit in the methods used. Nevertheless, the presence of a small population of GCs, with relatively high mean firing rates and unselective responsivity, conflicts with the classical notion of sparse population coding. Aimone et al. (2011) propose a resolution of this inconsistency, where classical sparse coding is implemented by the mature GC population while more active immature GCs expand the information content of individual assemblies by rate coding (see also sections 0 and 1.1.2).

## 4.8 Implications for DG function in Health and Disease

What are the functional implications of the present findings? Firstly, the tuning of the feedback inhibitory circuit, with exquisite sensitivity when only 1 to 3 % of GCs are active, is ideally suited for the purported functions of max pooling and assembly competition among the mature GC population. Secondly, the spatial tuning of the inhibitory microcircuit may further enhance the efficiency of the max pooling operation during spatially clustered GC activity by efficiently allocating inhibition and thereby equalizing GC activity levels over space. Such spatial tuning further suggests that assembly competition may be most intense at the local level or, more generally, that the feedback inhibitory circuit will shape the distribution of functional GC assemblies in space. Thirdly, the long duration of net feedback inhibition and its facilitation during trains of activity suggests that feedback inhibition mediated max pooling and assembly competition also act over time, segregating consecutive assemblies and limiting the number of assemblies that can be activated within longer time windows. Accordingly, an impairment of the feedback inhibitory microcircuitry is expected to first, increase excitability and activity, second, decrease pattern separation or discrimination ability, and third, decrease the information encoding capability and impair learning. In particular, my results suggest that impairments of these functions in disease may be due not only to the changed excitation/inhibition balance in the DG, but also to changes in the finely tuned spatiotemporal organization of the feedback circuit. Indeed, numerous studies indicate reorganization of the DG microcircuit in diseases which are characterized by deficits in precisely these three functions, namely mesial temporal lobe epilepsy, schizophrenia, and Alzheimer's disease or milder amnesic syndromes, respectively. Moreover, the symptoms of these diseases often display significant overlap (Born, 2015; Heckers et al., 1998; Hester and Danzer, 2014). In the following, I will present just a brief review of evidence linking the named diseases and the respective functional deficits to DG dysfunction.

By far the most intensely studied disease in respect to DG reorganization is mesial temporal lobe epilepsy, which is characterized by marked hyperactivity originating in the hippocampal region. Notably, this form of epilepsy is also associated with cognitive deficits such as impaired learning and is often comorbid with diseases like schizophrenia (Hester and Danzer, 2014). A hallmark of mesial temporal lobe epilepsy is mossy fiber sprouting, the diffuse

outgrowth of GC axons in the hilus and beyond, leading to a profound reorganization of the hilar microcircuit (Buckmaster, 2012; Goldberg and Coulter, 2013; Sloviter, 1987). Most prominently, there is substantial loss of hilar mossy cells and SST<sup>+</sup> interneurons (Buckmaster and Jongen-Rêlo, 1999; Huusko et al., 2015; de Lanerolle et al., 1989), while surviving hilar neurons undergo substantial morphological changes (Buckmaster et al., 2002; Thind et al., 2010; Zhang et al., 2009). The scope of these pathological changes strongly suggests that the intricate spatiotemporal organization of the physiological feedback inhibitory circuit described here may be impaired in temporal lobe epilepsy. Importantly, the question which pathological changes are pathogenic and which are compensatory remains controversial. However, if any of these outgrowth processes are compensatory in order to maintain the overall excitation/inhibition balance in the DG, this would suggest that they may partially occur at the cost of an impaired spatiotemporal tuning of the feedback circuit. Whether this kind of mechanism may underlie the cognitive deficits accompanying temporal lobe epilepsy remains an interesting question for future research.

The association between schizophrenia and DG dysfunction is still emerging (for review see Heckers and Konradi, 2014 and Tamminga et al., 2012). Nevertheless, various authors have begun to establish a link between the disambiguation deficits of schizophrenia and DG dysfunction at the behavioral and molecular levels in animal models and humans (Das et al., 2014; Faghihi and Moustafa, 2015; Knable et al., 2004; Stan et al., 2015). A link between Alzheimer's disease and DG dysfunction is also emerging (Andrews-Zwilling et al., 2012; Gazzaley et al., 1996; Yassa et al., 2011a; for review see Palmer and Good, 2011). For instance, a high resolution functional imaging study reported hyperactivity in the DG/CA3 area in patients with age related mild amnesic cognitive impairment and behavioral discrimination deficits (Yassa et al., 2011b). Interestingly, aged rats with similar symptoms displayed selective hilar interneuron loss (Spiegel et al., 2013).

Whether the spatiotemporal tuning of the DG feedback inhibitory circuit is impaired in these conditions remains to be shown. However, the suspicious overlap of symptoms between these diseases, all of which are associated with classical DG functions, does suggest an association. If this association is confirmed, the precise cellular and molecular alterations within the spatiotemporally graded feedback circuit may help to explain not only the similarities but also the differences between these diseases.

## 5. Summary

Perhaps the most powerful approach to understand how populations of neuronal cells can code and process information is the combination of computational and empirical studies. One recurring theme, consistently predicted by computational work and supported by empirical investigations throughout the brain, is the theory of sparse coding. It posits that only few neurons are active during the representation of any particular piece of information. Sparse coding is thought to optimally balance the different requirements of a network, such as its generalization and discrimination capabilities, its storage capacity and its metabolic cost. In the majority of computational studies, a canonical feedback inhibitory microcircuit motif is used to implement a type of ‘winner-take-all’ operation, enabling information representation by sparse coding. More specifically, this motif is thought to normalize the output of the population, a function termed max pooling, and to mediate assembly competition, a process deemed critical in the selection of neuronal groups. In the dentate gyrus of the hippocampus sparse coding, enforced by a feedback inhibitory microcircuit, is thought to be of particular importance, critically contributing to the functions of pattern separation and information encoding, as well as shielding against over-excitation. Previous studies have addressed how single glutamatergic cells or small groups thereof can recruit feedback inhibition. However, the feedback inhibitory microcircuit motif has never been empirically described over the entire range of population activity.

Therefore, I set out to quantitatively describe the feedback inhibitory microcircuit in the dentate gyrus of the hippocampus. To this end, I used a combination of electrophysiological recordings, population  $\text{Ca}^{2+}$  imaging and optogenetics to systematically probe the feedback inhibition elicited by granule cell populations of various sizes and spatiotemporal configurations. The results show that feedback inhibition is steeply recruited by sparse granule cell activity. Approximately 4 % of granule cells were sufficient to recruit maximal feedback inhibition within the local circuit. Importantly, the gain and sensitivity of the feedback inhibitory circuit were highest below 2 to 3 %, close to the physiological range of activity reported for GCs *in vivo*. Furthermore, the inhibition elicited by a local population of granule cells is distributed non-uniformly over the extent of the granule cell layer. Locally and remotely activated inhibition differ in several key aspects, namely their amplitude, recruitment curves, latencies and kinetic properties; local inhibition is larger, more efficiently

recruited, earlier and faster. This has important implications for the purported DG functions. It implies that the strength of assembly competition is organized in space and time, where competition is most intense locally, but an increased delay and decreased amplitude attenuate competition between more distant GCs. This will shape the spatial distribution of functional GC assemblies and may allow some degree of independent processing between DG blades. Furthermore, it may increase the metabolic efficiency and pattern separation efficacy during phases of spatially clustered input to GCs, by allocating inhibition only where it is needed. Finally, I showed that net feedback inhibition strongly facilitates during repetitive stimulation. This is a stark contrast to area CA1 where net feedback inhibition strongly depresses. It implies that the max pooling and assembly competition functions could also be efficiently implemented in time, thereby separating neuronal assemblies in space and time.

Taken together, these data provide the first quantitative functional description of a canonical feedback inhibitory microcircuit motif. They establish that sparse granule cell activity, within the range observed in-vivo, steeply recruits spatially and temporally graded feedback inhibition.

## 6. Bibliography

- Acsády, L., Kamondi, A., Sík, A., Freund, T., and Buzsáki, G. (1998). GABAergic cells are the major postsynaptic targets of mossy fibers in the rat hippocampus. *J. Neurosci.* *18*, 3386–3403.
- Adesnik, H., Bruns, W., Taniguchi, H., Huang, Z.J., and Scanziani, M. (2012). A neural circuit for spatial summation in visual cortex. *Nature* *490*, 226–231.
- Adrian, E.D., and Zotterman, Y. (1926). The impulses produced by sensory nerve endings: Part 3. Impulses set up by Touch and Pressure. *J. Physiol.* *61*, 465–483.
- Aimone, J.B., Deng, W., and Gage, F.H. (2011). Resolving new memories: a critical look at the dentate gyrus, adult neurogenesis, and pattern separation. *Neuron* *70*, 589–596.
- Alme, C.B., Buzzetti, R.A., Marrone, D.F., Leutgeb, J.K., Chawla, M.K., Schaner, M.J., Bohanick, J.D., Khoboko, T., Leutgeb, S., Moser, E.I., et al. (2010). Hippocampal granule cells opt for early retirement. *Hippocampus* *20*, 1109–1123.
- de Almeida, L., Idiart, M., and Lisman, J. (2009). A second function of gamma frequency oscillations: an E%-max winner-take-all mechanism selects which cells fire. *J. Neurosci.* *29*, 7497–7503.
- Alonso, M., Lepousez, G., Sebastien, W., Bardy, C., Gabellec, M.-M., Torquet, N., and Lledo, P.-M. (2012). Activation of adult-born neurons facilitates learning and memory. *Nat. Neurosci.* *15*, 897–904.
- Amaral, D.G. (1978). A Golgi study of cell types in the hilar region of the hippocampus in the rat. *J. Comp. Neurol.* *182*, 851–914.
- Amaral, D.G., Scharfman, H.E., and Lavenex, P. (2007). The dentate gyrus: fundamental neuroanatomical organization (dentate gyrus for dummies). *Prog. Brain Res.* *163*, 3–22.
- Amilhon, B., Huh, C.Y.L., Manseau, F., Ducharme, G., Nichol, H., Adamantidis, A., and Williams, S. (2015). Parvalbumin Interneurons of Hippocampus Tune Population Activity at Theta Frequency. *Neuron* *86*, 1277–1289.
- Amit, D.J., Gutfreund, H., and Sompolinsky, H. (1987). Statistical mechanics of neural networks near saturation. *Ann. Phys. (N. Y.)* *173*, 30–67.
- Andersen, P., Bliss, T. V, and Skrede, K.K. (1971). Lamellar organization of hippocampal pathways. *Exp. Brain Res.* *13*, 222–238.
- Andrews-Zwilling, Y., Gillespie, A.K., Kravitz, A. V, Nelson, A.B., Devidze, N., Lo, I., Yoon, S.Y., Bien-Ly, N., Ring, K., Zwilling, D., et al. (2012). Hilar GABAergic interneuron activity controls spatial learning and memory retrieval. *PLoS One* *7*, e40555.
- Ang, C.W., Carlson, G.C., and Coulter, D.A. (2006). Massive and specific dysregulation of direct cortical input to the hippocampus in temporal lobe epilepsy. *J. Neurosci.* *26*, 11850–11856.

- Attwell, D., and Laughlin, S.B. (2001). An energy budget for signaling in the grey matter of the brain. *J. Cereb. Blood Flow Metab.* 21, 1133–1145.
- Bakker, A., Kirwan, C.B., Miller, M., and Stark, C.E.L. (2008). Pattern separation in the human hippocampal CA3 and dentate gyrus. *Science* 319, 1640–1642.
- Barak, O., Rigotti, M., and Fusi, S. (2013). The Sparseness of Mixed Selectivity Neurons Controls the Generalization-Discrimination Trade-Off. *J. Neurosci.* 33, 3844–3856.
- Bartos, M., Vida, I., Frotscher, M., Meyer, A., Monyer, H., Geiger, J.R.P., and Jonas, P. (2002). Fast synaptic inhibition promotes synchronized gamma oscillations in hippocampal interneuron networks. *Proc. Natl. Acad. Sci. U. S. A.* 99, 13222–13227.
- Bartos, M., Vida, I., and Jonas, P. (2007). Synaptic mechanisms of synchronized gamma oscillations in inhibitory interneuron networks. *Nat. Rev. Neurosci.* 8, 45–56.
- Bettler, B. (2004). Molecular Structure and Physiological Functions of GABAB Receptors. *Physiol. Rev.* 84, 835–867.
- Binas, J., Rutishauser, U., Indiveri, G., and Pfeiffer, M. (2014). Learning and stabilization of winner-take-all dynamics through interacting excitatory and inhibitory plasticity. *Front. Comput. Neurosci.* 8, 68.
- Bischofberger, J., Engel, D., Li, L., Geiger, J.R.P., and Jonas, P. (2006). Patch-clamp recording from mossy fiber terminals in hippocampal slices. *Nat. Protoc.* 1, 2075–2081.
- Bliss, T. V, and Lomo, T. (1973). Long-lasting potentiation of synaptic transmission in the dentate area of the anaesthetized rabbit following stimulation of the perforant path. *J. Physiol.* 232, 331–356.
- Born, H.A. (2015). Seizures in Alzheimer’s disease. *Neuroscience* 286, 251–263.
- Bramham, C.R., Alme, M.N., Bittins, M., Kuipers, S.D., Nair, R.R., Pai, B., Panja, D., Schubert, M., Soule, J., Tiron, A., et al. (2010). The Arc of synaptic memory. *Exp. Brain Res.* 200, 125–140.
- Brickley, S.G., and Mody, I. (2012). Extrasynaptic GABA(A) receptors: their function in the CNS and implications for disease. *Neuron* 73, 23–34.
- Buckmaster, P.S. (2012). Mossy Fiber Sprouting in the Dentate Gyrus - Jasper’s Basic Mechanisms of the Epilepsies [Internet]. 4th edition. (National Center for Biotechnology Information (US)).
- Buckmaster, P.S., and Jongen-Rêlo, A.L. (1999). Highly specific neuron loss preserves lateral inhibitory circuits in the dentate gyrus of kainate-induced epileptic rats. *J. Neurosci.* 19, 9519–9529.
- Buckmaster, P.S., Yamawaki, R., and Zhang, G.F. (2002). Axon arbors and synaptic connections of a vulnerable population of interneurons in the dentate gyrus in vivo. *J. Comp. Neurol.* 445, 360–373.

- Buračas, G.T., Zador, A.M., DeWeese, M.R., and Albright, T.D. (1998). Efficient Discrimination of Temporal Patterns by Motion-Sensitive Neurons in Primate Visual Cortex. *Neuron* 20, 959–969.
- Busse, L., Wade, A.R., and Carandini, M. (2009). Representation of concurrent stimuli by population activity in visual cortex. *Neuron* 64, 931–942.
- Buzsaki, G. (2006). *Rhythms of the Brain*.
- Buzsáki, G. (1984). Feed-forward inhibition in the hippocampal formation. *Prog. Neurobiol.* 22, 131–153.
- Buzsáki, G. (2010). Neural syntax: cell assemblies, synapsembles, and readers. *Neuron* 68, 362–385.
- Buzsáki, G., and Draguhn, A. (2004). Neuronal oscillations in cortical networks. *Science* 304, 1926–1929.
- Caputi, A., Melzer, S., Michael, M., and Monyer, H. (2013). The long and short of GABAergic neurons. *Curr. Opin. Neurobiol.* 23, 179–186.
- Carandini, M., and Heeger, D.J. (2012). Normalization as a canonical neural computation. *Nat. Rev. Neurosci.* 13, 51–62.
- Cardin, J.A., Carlén, M., Meletis, K., Knoblich, U., Zhang, F., Deisseroth, K., Tsai, L.-H., and Moore, C.I. (2009). Driving fast-spiking cells induces gamma rhythm and controls sensory responses. *Nature* 459, 663–667.
- Chawla, M.K., Guzowski, J.F., Ramirez-Amaya, V., Lipa, P., Hoffman, K.L., Marriott, L.K., Worley, P.F., McNaughton, B.L., and Barnes, C. a (2005). Sparse, environmentally selective expression of Arc RNA in the upper blade of the rodent fascia dentata by brief spatial experience. *Hippocampus* 15, 579–586.
- Chiang, P.-H., Wu, P.-Y., Kuo, T.-W., Liu, Y.-C., Chan, C.-F., Chien, T.-C., Cheng, J.-K., Huang, Y.-Y., Chiu, C.-D., and Lien, C.-C. (2012). GABA is depolarizing in hippocampal dentate granule cells of the adolescent and adult rats. *J. Neurosci.* 32, 62–67.
- Chiu, C.Q., Lur, G., Morse, T.M., Carnevale, N.T., Ellis-Davies, G.C.R., and Higley, M.J. (2013). Compartmentalization of GABAergic inhibition by dendritic spines. *Science* 340, 759–762.
- Chrobak, J.J., and Buzsáki, G. (1995). Temporal structure in spatially organized neuronal ensembles: a role for interneuronal networks. *Curr. Opin. Neurobiol.* 5, 504–510.
- Cichon, J., and Gan, W.-B. (2015). Branch-specific dendritic Ca<sup>2+</sup> spikes cause persistent synaptic plasticity. *Nature* 520, 180–185.
- Claiborne, B.J., Amaral, D.G., and Cowan, W.M. (1990). Quantitative, three-dimensional analysis of granule cell dendrites in the rat dentate gyrus. *J. Comp. Neurol.* 302, 206–219.
- Clelland, C.D., Choi, M., Romberg, C., Clemenson, G.D., Fragniere, A., Tyers, P., Jessberger,

- S., Saksida, L.M., Barker, R.A., Gage, F.H., et al. (2009). A functional role for adult hippocampal neurogenesis in spatial pattern separation. *Science* 325, 210–213.
- Cobb, S.R., Buhl, E.H., Halasy, K., Paulsen, O., and Somogyi, P. (1995). Synchronization of neuronal activity in hippocampus by individual GABAergic interneurons. *Nature* 378, 75–78.
- Coulter, D.A. (2000). Mossy fiber zinc and temporal lobe epilepsy: pathological association with altered “epileptic” gamma-aminobutyric acid A receptors in dentate granule cells. *Epilepsia* 41 Suppl 6, S96–S99.
- Craig, M.T., and McBain, C.J. (2014). The emerging role of GABAB receptors as regulators of network dynamics: fast actions from a “slow” receptor? *Curr. Opin. Neurobiol.* 26, 15–21.
- Crochet, S., Poulet, J.F.A., Kremer, Y., and Petersen, C.C.H. (2011). Synaptic mechanisms underlying sparse coding of active touch. *Neuron* 69, 1160–1175.
- Dannenberg, H., Pabst, M., Braganza, O., Schoch, S., Niediek, J., Bayraktar, M., Mormann, F., and Beck, H. (2015). Synergy of Direct and Indirect Cholinergic Septo-Hippocampal Pathways Coordinates Firing in Hippocampal Networks. *J. Neurosci.* 35, 8394–8410.
- Das, T., Ivleva, E.I., Wagner, A.D., Stark, C.E.L., and Tamminga, C.A. (2014). Loss of pattern separation performance in schizophrenia suggests dentate gyrus dysfunction. *Schizophr. Res.* 159, 193–197.
- Dasgupta, D., and Sikdar, S.K. (2015). Calcium permeable AMPA receptor-dependent long lasting plasticity of intrinsic excitability in fast spiking interneurons of the dentate gyrus decreases inhibition in the granule cell layer. *Hippocampus* 25, 269–285.
- deCharms, R.C., and Merzenich, M.M. (1996). Primary cortical representation of sounds by the coordination of action-potential timing. *Nature* 381, 610–613.
- deCharms, R.C., and Zador, A. (2000). Neural representation and the cortical code. *Annu. Rev. Neurosci.* 23, 613–647.
- Doherty, J., and Dingledine, R. (1998). Differential Regulation of Synaptic Inputs to Dentate Hilar Border Interneurons by Metabotropic Glutamate Receptors. 2903–2910.
- Douglas, R.J., and Martin, K.A. (1991). A functional microcircuit for cat visual cortex. *J. Physiol.* 440, 735–769.
- Elgueta, C., Köhler, J., and Bartos, M. (2015). Persistent discharges in dentate gyrus perisoma-inhibiting interneurons require hyperpolarization-activated cyclic nucleotide-gated channel activation. *J. Neurosci.* 35, 4131–4139.
- Espósito, M.S., Piatti, V.C., Laplagne, D.A., Morgenstern, N.A., Ferrari, C.C., Pitossi, F.J., and Schinder, A.F. (2005). Neuronal differentiation in the adult hippocampus recapitulates embryonic development. *J. Neurosci.* 25, 10074–10086.
- Ewell, L., and Jones, M. (2010). Frequency-tuned distribution of inhibition in the dentate gyrus. *J. Neurosci.* 30, 12597–12607.

- Faghihi, F., and Moustafa, A.A. (2015). A computational model of pattern separation efficiency in the dentate gyrus with implications in schizophrenia. *Front. Syst. Neurosci.* *9*, 42.
- Fanselow, M.S. (2000). Contextual fear, gestalt memories, and the hippocampus. *Behav. Brain Res.* *110*, 73–81.
- Feldt Muldoon, S., Soltesz, I., and Cossart, R. (2013). Spatially clustered neuronal assemblies comprise the microstructure of synchrony in chronically epileptic networks. *Proc. Natl. Acad. Sci. U. S. A.* *110*, 3567–3572.
- Foldiak, P. (2002). Sparse coding in the primate cortex. *Handb. Brain Theory Neural Networks* 7.
- Freund, T.F., and Antal, M. (1988). GABA-containing neurons in the septum control inhibitory interneurons in the hippocampus. *Nature* *336*, 170–173.
- Fujisawa, S., Amarasingham, A., Harrison, M.T., and Buzsáki, G. (2008). Behavior-dependent short-term assembly dynamics in the medial prefrontal cortex. *Nat. Neurosci.* *11*, 823–833.
- Fukunaga, I., Herb, J.T., Kollo, M., Boyden, E.S., and Schaefer, A.T. (2014). Independent control of gamma and theta activity by distinct interneuron networks in the olfactory bulb. *Nat. Neurosci.* *17*, 1208–1216.
- Gabernet, L., Jadhav, S.P., Feldman, D.E., Carandini, M., and Scanziani, M. (2005). Somatosensory integration controlled by dynamic thalamocortical feed-forward inhibition. *Neuron* *48*, 315–327.
- Garaschuk, O., Milos, R., and Konnerth, A. (2006). Targeted bulk-loading of fluorescent indicators for two-photon brain imaging in vivo. *Nat. Protoc.* *1*, 380–386.
- Gassmann, M., and Bettler, B. (2012). Regulation of neuronal GABA(B) receptor functions by subunit composition. *Nat. Rev. Neurosci.* *13*, 380–394.
- Gazzaley, A.H., Siegel, S.J., Kordower, J.H., Mufson, E.J., and Morrison, J.H. (1996). Circuit-specific alterations of N-methyl-D-aspartate receptor subunit 1 in the dentate gyrus of aged monkeys. *Proc. Natl. Acad. Sci. U. S. A.* *93*, 3121–3125.
- Ge, S., Goh, E.L.K., Sailor, K.A., Kitabatake, Y., Ming, G., and Song, H. (2006). GABA regulates synaptic integration of newly generated neurons in the adult brain. *Nature* *439*, 589–593.
- Ge, S., Yang, C.-H., Hsu, K.-S., Ming, G.-L., and Song, H. (2007). A critical period for enhanced synaptic plasticity in newly generated neurons of the adult brain. *Neuron* *54*, 559–566.
- Geiger, J.R., Lübke, J., Roth, A., Frotscher, M., and Jonas, P. (1997). Submillisecond AMPA receptor-mediated signaling at a principal neuron-interneuron synapse. *Neuron* *18*, 1009–1023.

- Geisler, C., Robbe, D., Zugaro, M., Sirota, A., and Buzsáki, G. (2007). Hippocampal place cell assemblies are speed-controlled oscillators. *Proc. Natl. Acad. Sci. U. S. A.* *104*, 8149–8154.
- Gidon, A., and Segev, I. (2012). Principles governing the operation of synaptic inhibition in dendrites. *Neuron* *75*, 330–341.
- Gilbert, P.E., Kesner, R.P., and DeCoteau, W.E. (1998). Memory for Spatial Location: Role of the Hippocampus in Mediating Spatial Pattern Separation. *J. Neurosci.* *18*, 804–810.
- Gilbert, P.E., Kesner, R.P., and Lee, I. (2001). Dissociating hippocampal subregions: double dissociation between dentate gyrus and CA1. *Hippocampus* *11*, 626–636.
- Goldberg, E.M., and Coulter, D.A. (2013). Mechanisms of epileptogenesis: a convergence on neural circuit dysfunction. *Nat. Rev. Neurosci.* *14*, 337–349.
- Gong, S., Zheng, C., Doughty, M.L., Losos, K., Didkovsky, N., Schambra, U.B., Nowak, N.J., Joyner, A., Leblanc, G., Hatten, M.E., et al. (2003). A gene expression atlas of the central nervous system based on bacterial artificial chromosomes. *Nature* *425*, 917–925.
- Gong, S., Doughty, M., Harbaugh, C.R., Cummins, A., Hatten, M.E., Heintz, N., and Gerfen, C.R. (2007). Targeting Cre recombinase to specific neuron populations with bacterial artificial chromosome constructs. *J. Neurosci.* *27*, 9817–9823.
- Gray, C.M., König, P., Engel, A.K., and Singer, W. (1989). Oscillatory responses in cat visual cortex exhibit inter-columnar synchronization which reflects global stimulus properties. *Nature* *338*, 334–337.
- Gulyas, A.I., Hajos, N., and Freund, T.F. (1996). Interneurons Containing Calretinin Are Specialized to Control Other Interneurons in the Rat Hippocampus. *J. Neurosci.* *16*, 3397–3411.
- Guzowski, J.F., McNaughton, B.L., Barnes, C.A., and Worley, P.F. (1999). Environment-specific expression of the immediate-early gene *Arc* in hippocampal neuronal ensembles. *Nat. Neurosci.* *2*, 1120–1124.
- Guzowski, J.F., Miyashita, T., Chawla, M.K., Sanderson, J., Maes, L.I., Houston, F.P., Lipa, P., McNaughton, B.L., Worley, P.F., and Barnes, C.A. (2006). Recent behavioral history modifies coupling between cell activity and *Arc* gene transcription in hippocampal CA1 neurons. *Proc. Natl. Acad. Sci. U. S. A.* *103*, 1077–1082.
- Halasy, K., and Somogyi, P. (1993). Subdivisions in the multiple GABAergic innervation of granule cells in the dentate gyrus of the rat hippocampus. *Eur. J. Neurosci.* *5*, 411–429.
- Han, Z.S., Buhl, E.H., Lörinczi, Z., and Somogyi, P. (1993). A high degree of spatial selectivity in the axonal and dendritic domains of physiologically identified local-circuit neurons in the dentate gyrus of the rat hippocampus. *Eur. J. Neurosci.* *5*, 395–410.
- Harney, S.C., and Jones, M. V (2002). Pre- and postsynaptic properties of somatic and dendritic inhibition in dentate gyrus. *Neuropharmacology* *43*, 584–594.

- Harris, K.D. (2005). Neural signatures of cell assembly organization. *Nat. Rev. Neurosci.* 6, 399–407.
- Hebb, D.O. (1949). *The Organization of Behaviour* (Wiley & Sons).
- Heckers, S., and Konradi, C. (2015). GABAergic mechanisms of hippocampal hyperactivity in schizophrenia. *Schizophr. Res.* 167, 4–11.
- Heckers, S., Rauch, S.L., Goff, D., Savage, C.R., Schacter, D.L., Fischman, A.J., and Alpert, N.M. (1998). Impaired recruitment of the hippocampus during conscious recollection in schizophrenia. *Nat. Neurosci.* 1, 318–323.
- Hefft, S., and Jonas, P. (2005). Asynchronous GABA release generates long-lasting inhibition at a hippocampal interneuron-principal neuron synapse. *Nat. Neurosci.* 8, 1319–1328.
- Heinemann, U., Beck, H., Dreier, J.P., Ficker, E., Stabel, J., and Zhang, C.L. (1992). The dentate gyrus as a regulated gate for the propagation of epileptiform activity. *Epilepsy Res. Suppl.* 7, 273–280.
- Henze, D. a, Wittner, L., and Buzsáki, G. (2002). Single granule cells reliably discharge targets in the hippocampal CA3 network in vivo. *Nat. Neurosci.* 5, 790–795.
- Hester, M.S., and Danzer, S.C. (2014). Hippocampal granule cell pathology in epilepsy - a possible structural basis for comorbidities of epilepsy? *Epilepsy Behav.* 38, 105–116.
- Hopfield, J.J. (1982). Neural networks and physical systems with emergent collective computational abilities. *Proc. Natl. Acad. Sci. U. S. A.* 79, 2554–2558.
- Hosp, J.A., Strüber, M., Yanagawa, Y., Obata, K., Vida, I., Jonas, P., and Bartos, M. (2014). Morpho-physiological criteria divide dentate gyrus interneurons into classes. *Hippocampus* 24, 189–203.
- Hromádka, T., Deweese, M.R., and Zador, A.M. (2008). Sparse representation of sounds in the unanesthetized auditory cortex. *PLoS Biol.* 6, e16.
- Hsu, T.-T., Lee, C.-T., Tai, M.-H., and Lien, C.-C. (2015). Differential Recruitment of Dentate Gyrus Interneuron Types by Commissural Versus Perforant Pathways. *Cereb. Cortex* bhv127 – .
- Hu, H., Ma, Y., and Agmon, A. (2011). Submillisecond firing synchrony between different subtypes of cortical interneurons connected chemically but not electrically. *J. Neurosci.* 31, 3351–3361.
- Hu, H., Gan, J., and Jonas, P. (2014). Fast-spiking, parvalbumin+ GABAergic interneurons: From cellular design to microcircuit function. *Science* (80-. ). 345, 1255263.
- Hubel, D.H., and Wiesel, T.N. (1962). Receptive fields, binocular interaction and functional architecture in the cat's visual cortex. *J. Physiol.* 160, 106–154.
- Hunt, R.F., Scheff, S.W., and Smith, B.N. (2011). Synaptic reorganization of inhibitory hilar interneuron circuitry after traumatic brain injury in mice. *J. Neurosci.* 31, 6880–6890.

- Huusko, N., Römer, C., Nnode-Ekane, X.E., Lukasiuk, K., and Pitkänen, A. (2015). Loss of hippocampal interneurons and epileptogenesis: a comparison of two animal models of acquired epilepsy. *Brain Struct. Funct.* *220*, 153–191.
- Ince, R.A.A., Senatore, R., Arabzadeh, E., Montani, F., Diamond, M.E., and Panzeri, S. (2010). Information-theoretic methods for studying population codes. *Neural Netw.* *23*, 713–727.
- Isaacson, J.S., and Scanziani, M. (2011). How inhibition shapes cortical activity. *Neuron* *72*, 231–243.
- Jinde, S., Zsiros, V., Jiang, Z., Nakao, K., Pickel, J., Kohno, K., Belforte, J.E., and Nakazawa, K. (2012). Hilar mossy cell degeneration causes transient dentate granule cell hyperexcitability and impaired pattern separation. *Neuron* *76*, 1189–1200.
- Jinde, S., Zsiros, V., and Nakazawa, K. (2013). Hilar mossy cell circuitry controlling dentate granule cell excitability. *Front. Neural Circuits* *7*, 14.
- Jung, M.W., and McNaughton, B.L. (1993). Spatial Selectivity of Unit Activity in the Hippocampal Granular Layer. *3*, 165–182.
- Kandel, E.R., Schwartz, J.H., and Jessell, T.M. (2000). *Principles of Neural Science*.
- Kapfer, C., Glickfeld, L., Atallah, B., and Scanziani, M. (2007). Supralinear increase of recurrent inhibition during sparse activity in the somatosensory cortex. *Nat. Neurosci.* *10*, 743–753.
- Katona, I., Acsády, L., and Freund, T.F. (1999). Postsynaptic targets of somatostatin-immunoreactive interneurons in the rat hippocampus. *Neuroscience* *88*, 37–55.
- Kee, N., Teixeira, C.M., Wang, A.H., and Frankland, P.W. (2007). Preferential incorporation of adult-generated granule cells into spatial memory networks in the dentate gyrus. *Nat. Neurosci.* *10*, 355–362.
- Kheirbek, M. a, Drew, L.J., Burghardt, N.S., Costantini, D.O., Tannenholz, L., Ahmari, S.E., Zeng, H., Fenton, A. a, and Hen, R. (2013). Differential control of learning and anxiety along the dorsoventral axis of the dentate gyrus. *Neuron* *77*, 955–968.
- Klausberger, T., and Somogyi, P. (2008). Neuronal diversity and temporal dynamics: the unity of hippocampal circuit operations. *Science* *321*, 53–57.
- Knable, M.B., Barci, B.M., Webster, M.J., Meador-Woodruff, J., and Torrey, E.F. (2004). Molecular abnormalities of the hippocampus in severe psychiatric illness: postmortem findings from the Stanley Neuropathology Consortium. *Mol. Psychiatry* *9*, 609–620, 544.
- Kraushaar, U., and Jonas, P. (2000). Efficacy and Stability of Quantal GABA Release at a Hippocampal Interneuron-Principal Neuron Synapse. *J. Neurosci.* *20*, 5594–5607.
- Kress, G.J., Dowling, M.J., Meeks, J.P., and Mennerick, S. (2008). High threshold, proximal initiation, and slow conduction velocity of action potentials in dentate granule neuron mossy

fibers. *J. Neurophysiol.* *100*, 281–291.

Krook-Magnuson, E., Armstrong, C., Bui, A., Lew, S., Oijala, M., and Soltesz, I. (2015). In vivo evaluation of the dentate gate theory in epilepsy. *J. Physiol.* *593*, 2379–2388.

Krueppel, R., Remy, S., and Beck, H. (2011). Dendritic integration in hippocampal dentate granule cells. *Neuron* *71*, 512–528.

de Lanerolle, N.C., Kim, J.H., Robbins, R.J., and Spencer, D.D. (1989). Hippocampal interneuron loss and plasticity in human temporal lobe epilepsy. *Brain Res.* *495*, 387–395.

Larimer, P., and Strowbridge, B.W. (2008). Nonrandom Local Circuits in the Dentate Gyrus. *J. Neurosci.* *28*, 12212–12223.

Leão, R.N., Mikulovic, S., Leão, K.E., Munguba, H., Gezelius, H., Enjin, A., Patra, K., Eriksson, A., Loew, L.M., Tort, A.B.L., et al. (2012). OLM interneurons differentially modulate CA3 and entorhinal inputs to hippocampal CA1 neurons. *Nat. Neurosci.* *15*, 1524–1530.

Lee, I., and Kesner, R.P. (2004). Encoding versus retrieval of spatial memory: double dissociation between the dentate gyrus and the perforant path inputs into CA3 in the dorsal hippocampus. *Hippocampus* *14*, 66–76.

Lee, S.-H., Marchionni, I., Bezaire, M., Varga, C., Danielson, N., Lovett-Barron, M., Losonczy, A., and Soltesz, I. (2014). Parvalbumin-positive basket cells differentiate among hippocampal pyramidal cells. *Neuron* *82*, 1129–1144.

Lein, E.S., Hawrylycz, M.J., Ao, N., Ayres, M., Bensinger, A., Bernard, A., Boe, A.F., Boguski, M.S., Brockway, K.S., Byrnes, E.J., et al. (2007). Genome-wide atlas of gene expression in the adult mouse brain. *Nature* *445*, 168–176.

Letzkus, J.J., Wolff, S.B.E., Meyer, E.M.M., Tovote, P., Courtin, J., Herry, C., and Lüthi, A. (2011). A disinhibitory microcircuit for associative fear learning in the auditory cortex. *Nature* *480*, 331–335.

Leutgeb, J.J.K.J., Leutgeb, S., Moser, M.M.-B.M., and Moser, E.E.I. (2007). Pattern separation in the dentate gyrus and CA3 of the hippocampus. *Science* (80-. ). *315*, 961–966.

Li, H., Penzo, M.A., Taniguchi, H., Kopec, C.D., Huang, Z.J., and Li, B. (2013a). Experience-dependent modification of a central amygdala fear circuit. *Nat. Neurosci.* *16*, 332–339.

Li, Y., Aimone, J.B., Xu, X., Callaway, E.M., and Gage, F.H. (2012). Development of GABAergic inputs controls the contribution of maturing neurons to the adult hippocampal network. *Proc. Natl. Acad. Sci. U. S. A.* *109*, 4290–4295.

Li, Y., Stam, F.J., Aimone, J.B., Goulding, M., Callaway, E.M., and Gage, F.H. (2013b). Molecular layer perforant path-associated cells contribute to feed-forward inhibition in the adult dentate gyrus. *Proc. Natl. Acad. Sci. U. S. A.* *110*.

Lin, A.C., Bygrave, A.M., de Calignon, A., Lee, T., and Miesenböck, G. (2014). Sparse,

decorrelated odor coding in the mushroom body enhances learned odor discrimination. *Nat. Neurosci.* *17*, 559–568.

Lin, Y.-W., Yang, H.-W., Wang, H.-J., Gong, C.-L., Chiu, T.-H., and Min, M.-Y. (2006). Spike-timing-dependent plasticity at resting and conditioned lateral perforant path synapses on granule cells in the dentate gyrus: different roles of N-methyl-D-aspartate and group I metabotropic glutamate receptors. *Eur. J. Neurosci.* *23*, 2362–2374.

Liu, B., Li, Y., Ma, W., Pan, C., Zhang, L.I., and Tao, H.W. (2011). Broad inhibition sharpens orientation selectivity by expanding input dynamic range in mouse simple cells. *Neuron* *71*, 542–554.

Liu, X., Ramirez, S., Pang, P.T., Puryear, C.B., Govindarajan, A., Deisseroth, K., and Tonegawa, S. (2012). Optogenetic stimulation of a hippocampal engram activates fear memory recall. *Nature* *484*, 381–385.

Liu, Y.-C., Cheng, J.-K., and Lien, C.-C. (2014). Rapid dynamic changes of dendritic inhibition in the dentate gyrus by presynaptic activity patterns. *J. Neurosci.* *34*, 1344–1357.

Lorente De Nó, R. (1934). Studies on the structure of the cerebral cortex. II. Continuation of the study of the ammonic system. *J. Für Psychol. Und Neurol.* *46*, 113–117.

Losonczy, A., Makara, J.K., and Magee, J.C. (2008). Compartmentalized dendritic plasticity and input feature storage in neurons. *Nature* *452*, 436–441.

Lothman, E.W., Stringer, J.L., and Bertram, E.H. (1992). The dentate gyrus as a control point for seizures in the hippocampus and beyond. *Epilepsy Res. Suppl.* *7*, 301–313.

Lovett-Barron, M., Kaifosh, P., Kheirbek, M.A., Danielson, N., Zaremba, J.D., Reardon, T.R., Turi, G.F., Hen, R., Zemelman, B. V., and Losonczy, A. (2014). Dendritic inhibition in the hippocampus supports fear learning. *Science* *343*, 857–863.

Lysetskii, M., Földy, C., and Soltesz, I. (2005). Long- and short-term plasticity at mossy fiber synapses on mossy cells in the rat dentate gyrus. *Hippocampus* *15*, 691–696.

Madisen, L., Mao, T., Koch, H., Zhuo, J., Berenyi, A., Fujisawa, S., Hsu, Y.-W.A., Garcia, A.J., Gu, X., Zanella, S., et al. (2012). A toolbox of Cre-dependent optogenetic transgenic mice for light-induced activation and silencing. *Nat. Neurosci.* *15*, 793–802.

Marin-Burgin, A., Mongiat, L.A., Pardi, M.B., and Schinder, A.F. (2012). Unique Processing During a Period of High Excitation/Inhibition Balance in Adult-Born Neurons. *Science* (80-. ). *335*, 1238–1242.

Marr, D. (1969). A theory of cerebellar cortex. *J. Physiol.* *202*, 437–470.

Marr, D. (1971). Simple memory: a theory for archicortex. *Philos. Trans. R. Soc. Lond. B. Biol. Sci.* *262*, 23–81.

Maurer, A.P., and McNaughton, B.L. (2007). Network and intrinsic cellular mechanisms underlying theta phase precession of hippocampal neurons. *Trends Neurosci.* *30*, 325–333.

- Maurer, A.P., Cowen, S.L., Burke, S.N., Barnes, C.A., and McNaughton, B.L. (2006). Organization of hippocampal cell assemblies based on theta phase precession. *Hippocampus* 16, 785–794.
- McHugh, T.J., Jones, M.W., Quinn, J.J., Balthasar, N., Coppari, R., Elmquist, J.K., Lowell, B.B., Fanselow, M.S., Wilson, M.A., and Tonegawa, S. (2007). Dentate gyrus NMDA receptors mediate rapid pattern separation in the hippocampal network. *Science* 317, 94–99.
- McNaughton, B.L., and Morris, R.G.M. (1987). Hippocampal synaptic enhancement and information storage within a distributed memory system. *Trends Neurosci.* 10, 408–415.
- Miles, R. (1990). Synaptic excitation of inhibitory cells by single CA3 hippocampal pyramidal cells of the guinea-pig in vitro. *J. Physiol.* 428, 61–77.
- Miles, R., Toth, K., Gulyas, A., Hajos, N., and Freund, T. (1996). Differences between Somatic and Dendritic Inhibition in the Hippocampus. *Neuron* 16, 815–823.
- Mody, I., and Pearce, R.A. (2004). Diversity of inhibitory neurotransmission through GABA(A) receptors. *Trends Neurosci.* 27, 569–575.
- Moser, M.-B., Rowland, D.C., and Moser, E.I. (2015). Place cells, grid cells, and memory. *Cold Spring Harb. Perspect. Biol.* 7, a021808.
- Mott, D.D., and Lewis, D. V (1994). The pharmacology and function of central GABAB receptors. *Int. Rev. Neurobiol.* 36, 97–223.
- Mott, D.D., Turner, D.A., Okazaki, M.M., and Lewis, D. V. (1997). Interneurons of the Dentate-Hilus Border of the Rat Dentate Gyrus: Morphological and Electrophysiological Heterogeneity. *J. Neurosci.* 17, 3990–4005.
- Mountcastle, V.B., and Powel, T.P. (1959). Neural mechanisms subserving cutaneous sensibility, with special reference to the role of afferent inhibition in sensory perception and discrimination. *Bull. Johns Hopkins Hosp.* 105, 201–232.
- Myers, C.E., and Scharfman, H.E. (2009). A role for hilar cells in pattern separation in the dentate gyrus: a computational approach. *Hippocampus* 19, 321–337.
- Nadler, J.V., Perry, B.W., Gentry, C., and Cotman, C.W. (1980). Loss and reacquisition of hippocampal synapses after selective destruction of CA3–CA4 afferents with kainic acid. *Brain Res.* 191, 387–403.
- Nakashiba, T., Cushman, J.D., Pelkey, K.A., Renaudineau, S., Buhl, D.L., McHugh, T.J., Rodriguez Barrera, V., Chittajallu, R., Iwamoto, K.S., McBain, C.J., et al. (2012). Young Dentate Granule Cells Mediate Pattern Separation, whereas Old Granule Cells Facilitate Pattern Completion. *Cell* 149, 1–14.
- Neunuebel, J.P., and Knierim, J.J. (2014). CA3 Retrieves Coherent Representations from Degraded Input: Direct Evidence for CA3 Pattern Completion and Dentate Gyrus Pattern Separation. *Neuron* 81, 416–427.

- Nitz, D., and McNaughton, B. (2004). Differential modulation of CA1 and dentate gyrus interneurons during exploration of novel environments. *J. Neurophysiol.* *91*, 863–872.
- Nusser, Z., and Mody, I. (2002). Selective modulation of tonic and phasic inhibitions in dentate gyrus granule cells. *J. Neurophysiol.* *87*, 2624–2628.
- O’Keefe, J., and Dostrovsky, J. (1971). The hippocampus as a spatial map. Preliminary evidence from unit activity in the freely-moving rat. *Brain Res.* *34*, 171–175.
- O’Keefe, J., and Recce, M.L. (1993). Phase relationship between hippocampal place units and the EEG theta rhythm. *Hippocampus* *3*, 317–330.
- O’Reilly, R.C., and McClelland, J.L. (1994). Hippocampal conjunctive encoding, storage, and recall: avoiding a trade-off. *Hippocampus* *4*, 661–682.
- Olsen, R.W., and Sieghart, W. (2008). International Union of Pharmacology. LXX. Subtypes of gamma-aminobutyric acid(A) receptors: classification on the basis of subunit composition, pharmacology, and function. Update. *Pharmacol. Rev.* *60*, 243–260.
- Olsen, S.R.S., Bhandawat, V., and Wilson, R.I.R. (2010). Divisive normalization in olfactory population codes. *Neuron* *66*, 287–299.
- Olshausen, B.A., and Field, D.J. (1996). Emergence of simple-cell receptive field properties by learning a sparse code for natural images. *Nature* *381*, 607–609.
- Palmer, A., and Good, M. (2011). Hippocampal synaptic activity, pattern separation and episodic-like memory: implications for mouse models of Alzheimer’s disease pathology. *Biochem. Soc. Trans.* *39*, 902–909.
- Papadopoulou, M., Cassenaer, S., Nowotny, T., and Laurent, G. (2011). Normalization for sparse encoding of odors by a wide-field interneuron. *Science* *332*, 721–725.
- Pastalkova, E., Itskov, V., Amarasingham, A., and Buzsaki, G. (2008). Internally Generated Cell Assembly Sequences in the Rat Hippocampus. *Science* (80-. ). *321*, 1322–1327.
- Peng, Z., Zhang, N., Wei, W., Huang, C.S., Cetina, Y., Otis, T.S., and Houser, C.R. (2013). A reorganized GABAergic circuit in a model of epilepsy: evidence from optogenetic labeling and stimulation of somatostatin interneurons. *J. Neurosci.* *33*, 14392–14405.
- Pernía-Andrade, A.J., and Jonas, P. (2014). Theta-gamma-modulated synaptic currents in hippocampal granule cells in vivo define a mechanism for network oscillations. *Neuron* *81*, 140–152.
- Petrantonakis, P.C., and Poirazi, P. (2015). Dentate gyrus circuitry features improve performance of sparse approximation algorithms. *PLoS One* *10*, e0117023.
- Pi, H.-J., Hangya, B., Kvitsiani, D., Sanders, J.I., Huang, Z.J., and Kepecs, A. (2013). Cortical interneurons that specialize in disinhibitory control. *Nature* *503*, 521–524.
- Pothmann, L., Müller, C., Averkin, R.G., Bellistri, E., Miklitz, C., Uebachs, M., Remy, S., Menendez de la Prida, L., and Beck, H. (2014). Function of inhibitory micronetworks is

- spared by Na<sup>+</sup> channel-acting anticonvulsant drugs. *J. Neurosci.* *34*, 9720–9735.
- Pouille, F., and Scanziani, M. (2001). Enforcement of temporal fidelity in pyramidal cells by somatic feed-forward inhibition. *Science* *293*, 1159–1163.
- Pouille, F., and Scanziani, M. (2004). Routing of spike series by dynamic circuits in the hippocampus. *Nature* *429*, 717–723.
- Pouille, F., Marin-Burgin, A., Adesnik, H., Atallah, B. V., and Scanziani, M. (2009). Input normalization by global feedforward inhibition expands cortical dynamic range. *Nat. ...* *12*, 1577–1585.
- Ratzliff, A.D.H., Howard, A.L., Santhakumar, V., Osapay, I., and Soltesz, I. (2004). Rapid deletion of mossy cells does not result in a hyperexcitable dentate gyrus: implications for epileptogenesis. *J. Neurosci.* *24*, 2259–2269.
- Renno-Costa, C., Lisman, J., and Verschure, P. (2010). The Mechanism of Rate Remapping in the Dentate Gyrus. *Neuron* *68*, 1051–1058.
- Ribak, C.E., Seress, L., Peterson, G.M., Seroogy, K.B., Fallon, J.H., and Schmued, L.C. (1986). A GABAergic inhibitory component within the hippocampal commissural pathway. *J. Neurosci.* *6*, 3492–3498.
- Rolls, E.T. (2010). A computational theory of episodic memory formation in the hippocampus. *Behav. Brain Res.* *215*, 180–196.
- Rolls, E.T. (2013). The mechanisms for pattern completion and pattern separation in the hippocampus. *Front. Syst. Neurosci.* *7*, 74.
- Rolls, E.T., and Treves, A. (1998). *Neural Networks and Brain Function - Chapter 4: Competitive networks.* 54–74.
- Roux, L., and Buzsáki, G. (2014). Tasks for inhibitory interneurons in intact brain circuits. *Neuropharmacology* *88*, 10–23.
- Royer, S., Zemelman, B. V., Losonczy, A., Kim, J., Chance, F., Magee, J.C., and Buzsáki, G. (2012). Control of timing, rate and bursts of hippocampal place cells by dendritic and somatic inhibition. *Nat. Neurosci.* *15*, 769–775.
- Sahay, A., Scobie, K.N., Hill, A.S., O’Carroll, C.M., Kheirbek, M.A., Burghardt, N.S., Fenton, A.A., Dranovsky, A., and Hen, R. (2011). Increasing adult hippocampal neurogenesis is sufficient to improve pattern separation. *Nature* *472*, 466–470.
- Sambandan, S., Sauer, J.-F.J.-F., Vida, I., and Bartos, M. (2010). Associative plasticity at excitatory synapses facilitates recruitment of fast-spiking interneurons in the dentate gyrus. *J. Neurosci.* *30*, 11826–11837.
- Santoro, A. (2013). Reassessing pattern separation in the dentate gyrus. *Front. Behav. Neurosci.* *7*, 96.
- Savanthrapadian, S., Meyer, T., Elgueta, C., Booker, S. a, Vida, I., and Bartos, M. (2014).

- Synaptic properties of SOM- and CCK-expressing cells in dentate gyrus interneuron networks. *J. Neurosci.* *34*, 8197–8209.
- Scharfman, H. (2007). The CA3 “backprojection” to the dentate gyrus. *Prog. Brain Res.* 627–637.
- Scharfman, H.E. (1995). Electrophysiological evidence that dentate hilar mossy cells are excitatory and innervate both granule cells and interneurons. *J. Neurophysiol.* *74*, 179–194.
- Schmidt, B., Marrone, D.F., and Markus, E.J. (2012). Disambiguating the similar: the dentate gyrus and pattern separation. *Behav. Brain Res.* *226*, 56–65.
- Schmidt-Hieber, C., Jonas, P., and Bischofberger, J. (2004). Enhanced synaptic plasticity in newly generated granule cells of the adult hippocampus. *Nature* *429*, 184–187.
- Schneider, D.M., and Woolley, S.M.N. (2013). Sparse and background-invariant coding of vocalizations in auditory scenes. *Neuron* *79*, 141–152.
- Scoville, W.B., and Milner, B. (1957). Loss of recent memory after bilateral hippocampal lesions. *J. Neurol. Neurosurg. Psychiatry* *20*, 11–21.
- Shannon, C.E. (1948). A mathematical theory of communication. *Bell Syst. Tech. J.* *27*, 379–423.
- Shigemoto, R., Kinoshita, A., Wada, E., Nomura, S., Ohishi, H., Takada, M., Flor, P.J., Neki, A., Abe, T., Nakanishi, S., et al. (1997). Differential presynaptic localization of metabotropic glutamate receptor subtypes in the rat hippocampus. *J. Neurosci.* *17*, 7503–7522.
- Sik, A., Penttonen, M., and Buzsaki, G. (1997). Interneurons in the Hippocampal Dentate Gyrus : an In Vivo Intracellular Study. *Eur. J. Neurosci.* *9*, 573–588.
- Silberberg, G., and Markram, H. (2007). Disynaptic inhibition between neocortical pyramidal cells mediated by Martinotti cells. *Neuron* *53*, 735–746.
- Sillito, A.M. (1975). The contribution of inhibitory mechanisms to the receptive field properties of neurones in the striate cortex of the cat. *J. Physiol.* *250*, 305–329.
- Silver, R.A. (2010). Neuronal arithmetic. *Nat. Rev. Neurosci.* *11*, 474–489.
- Singer, W. (1999). Neuronal Synchrony: A Versatile Code for the Definition of Relations? *Neuron* *24*, 49–65.
- Skaggs, W.E., McNaughton, B.L., Wilson, M. a, and Barnes, C. a (1996). Theta phase precession in hippocampal neuronal populations and the compression of temporal sequences. *Hippocampus* *6*, 149–172.
- Sloviter, R.S. (1987). Decreased hippocampal inhibition and a selective loss of interneurons in experimental epilepsy. *Science* *235*, 73–76.
- Sloviter, R.S., and Brisman, J.L. (1995). Lateral Inhibition and Granule Cell Synchrony Dentate Gyrus in the Rat Hippocampal. *J. Neurosci.* *15*, 811–820.

- Sohal, V.S., Zhang, F., Yizhar, O., and Deisseroth, K. (2009). Parvalbumin neurons and gamma rhythms enhance cortical circuit performance. *Nature* 459, 698–702.
- Somogyi, P., and Klausberger, T. (2005). Defined types of cortical interneurone structure space and spike timing in the hippocampus. *J. Physiol.* 562, 9–26.
- Spiegel, A.M., Koh, M.T., Vogt, N.M., Rapp, P.R., and Gallagher, M. (2013). Hilar interneuron vulnerability distinguishes aged rats with memory impairment. *J. Comp. Neurol.* 521, 3508–3523.
- Staley, K.J., and Mody, I. (1992). Shunting of excitatory input to dentate gyrus granule cells by a depolarizing GABAA receptor-mediated postsynaptic conductance. *J. Neurophysiol.* 68, 197–212.
- Staley, K.J., Otis, T.S., and Mody, I. (1992). Membrane properties of dentate gyrus granule cells: comparison of sharp microelectrode and whole-cell recordings. *J. Neurophysiol.* 67, 1346–1358.
- Stan, A.D., Ghose, S., Zhao, C., Hulsey, K., Mihalakos, P., Yanagi, M., Morris, S.U., Bartko, J.J., Choi, C., and Tamminga, C.A. (2015). Magnetic resonance spectroscopy and tissue protein concentrations together suggest lower glutamate signaling in dentate gyrus in schizophrenia. *Mol. Psychiatry* 20, 433–439.
- Steriade, M., and Timofeev, I. (2003). Neuronal plasticity in thalamocortical networks during sleep and waking oscillations. *Neuron* 37, 563–576.
- Stokes, C.C.A., and Isaacson, J.S. (2010). From dendrite to soma: dynamic routing of inhibition by complementary interneuron microcircuits in olfactory cortex. *Neuron* 67, 452–465.
- Strüber, M., Jonas, P., and Bartos, M. (2015). Strength and duration of perisomatic GABAergic inhibition depend on distance between synaptically connected cells. *Proc. Natl. Acad. Sci. U. S. A.* 112, 1220–1225.
- Tamminga, C.A., Southcott, S., Sacco, C., Wagner, A.D., and Ghose, S. (2012). Glutamate dysfunction in hippocampus: relevance of dentate gyrus and CA3 signaling. *Schizophr. Bull.* 38, 927–935.
- Tan, Z., Hu, H., Huang, Z.J., and Agmon, A. (2008). Robust but delayed thalamocortical activation of dendritic-targeting inhibitory interneurons. *Proc. Natl. Acad. Sci. U. S. A.* 105, 2187–2192.
- Tashiro, A., Sandler, V.M., Toni, N., Zhao, C., and Gage, F.H. (2006). NMDA-receptor-mediated, cell-specific integration of new neurons in adult dentate gyrus. *Nature* 442, 929–933.
- Tashiro, A., Makino, H., and Gage, F.H. (2007). Experience-specific functional modification of the dentate gyrus through adult neurogenesis: a critical period during an immature stage. *J. Neurosci.* 27, 3252–3259.

- Temprana, S.G., Mongiat, L.A., Yang, S.M., Trincherro, M.F., Alvarez, D.D., Kropff, E., Giacomini, D., Beltramone, N., Lanuza, G.M., and Schinder, A.F. (2015). Delayed Coupling to Feedback Inhibition during a Critical Period for the Integration of Adult-Born Granule Cells. *Neuron* 85, 116–131.
- Thind, K.K., Yamawaki, R., Phanwar, I., Zhang, G., Wen, X., and Buckmaster, P.S. (2010). Initial loss but later excess of GABAergic synapses with dentate granule cells in a rat model of temporal lobe epilepsy. *J. Comp. Neurol.* 518, 647–667.
- Toth, K., Soares, G., Lawrence, J.J., Philips-Tansey, E., and McBain, C.J. (2000). Differential mechanisms of transmission at three types of mossy fiber synapse. *J. Neurosci.* 20, 8279–8289.
- Trappenberg, T.P. (2010). *Fundamentals of computational neuroscience*. Oxford Univ. Press.
- Treves, A., and Rolls, E.T. (1992). Computational constraints suggest the need for two distinct input systems to the hippocampal CA3 network. *Hippocampus* 2, 189–199.
- Tyan, L., Chamberland, S., Magnin, E., Camiré, O., Francavilla, R., David, L.S., Deisseroth, K., Topolnik, L., Camire, O., Francavilla, R., et al. (2014). Dendritic inhibition provided by interneuron-specific cells controls the firing rate and timing of the hippocampal feedback inhibitory circuitry. *J. Neurosci.* 34, 4534–4547.
- Varga, C., Golshani, P., and Soltesz, I. (2012). Frequency-invariant temporal ordering of interneuronal discharges during hippocampal oscillations in awake mice. *Proc. Natl. Acad. Sci. U. S. A.* 109, E2726–E2734.
- Vinje, W.E., and Gallant, J.L. (2000). Sparse coding and decorrelation in primary visual cortex during natural vision. *Science* 287, 1273–1276.
- Wehr, M., and Zador, A.M. (2003). Balanced inhibition underlies tuning and sharpens spike timing in auditory cortex. *Nature* 426, 442–446.
- Wiedemann, H.R. (1994). Hans Berger (1873-1941). *Eur. J. Pediatr.* 153, 705.
- Wilson, N.R., Runyan, C. a, Wang, F.L., and Sur, M. (2012). Division and subtraction by distinct cortical inhibitory networks in vivo. *Nature* 488, 343–348.
- Wozny, C., Gabriel, S., Jandova, K., Schulze, K., Heinemann, U., and Behr, J. (2005). Entorhinal cortex entrains epileptiform activity in CA1 in pilocarpine-treated rats. *Neurobiol. Dis.* 19, 451–460.
- Wright, B.J., and Jackson, M.B. (2014). Long-term potentiation in hilar circuitry modulates gating by the dentate gyrus. *J. Neurosci.* 34, 9743–9753.
- Yassa, M.A., Mattfeld, A.T., Stark, S.M., and Stark, C.E.L. (2011a). Age-related memory deficits linked to circuit-specific disruptions in the hippocampus. *Proc. Natl. Acad. Sci. U. S. A.* 108, 8873–8878.
- Yassa, M.A., Lacy, J.W., Stark, S.M., Albert, M.S., Gallagher, M., and Stark, C.E.L. (2011b).

Pattern separation deficits associated with increased hippocampal CA3 and dentate gyrus activity in nondemented older adults. *Hippocampus* 21, 968–979.

Yu, J., Swietek, B., Proddatur, A., and Santhakumar, V. (2015). Dentate total molecular layer interneurons mediate cannabinoid-sensitive inhibition. *Hippocampus* 25, 884–889.

Zhang, W., Yamawaki, R., Wen, X., Uhl, J., Diaz, J., Prince, D. a, and Buckmaster, P.S. (2009). Surviving hilar somatostatin interneurons enlarge, sprout axons, and form new synapses with granule cells in a mouse model of temporal lobe epilepsy. *J. Neurosci.* 29, 14247–14256.

Zipp, F., Nitsch, R., Soriano, E., and Frotscher, M. (1989). Entorhinal fibers form synaptic contacts on parvalbumin-immunoreactive neurons in the rat fascia dentata. *Brain Res.* 495, 161–166.

## 7. List of Abbreviations

AP	action potential
BC	basket cell (PV <sup>+</sup> unless otherwise indicated)
C/A	commissural/ associational path
CA1	cornu ammonis 1
CA3	cornu ammonis 3
CC	current clamp
CCD	charge coupled device
CCK	cholecystokinin
DG	dentate gyrus
e- stim	extracellular electrical stimulation
EPSC	excitatory postsynaptic current
EPSP	excitatory postsynaptic potential
FS	fast spiking cell (> 50Hz peak firing frequency)
GC	dentate gyrus granule cell
HICAP	hilar commissural/associational path associated cell
HIPP	hilar perforant path associated cell
IN	not further categorized interneuron
juv.	juvenile (12 to 25 days postnatally)
LTD	long term depression
LTP	long term potentiation
MC	mossy cell
MCP	maximum connectivity plane
MF	mossy fiber tract
ML	molecular layer
non- FS	non- FS (< 50Hz peak firing frequency)
OGB-1-AM	Oregon Green <sup>®</sup> 488 BAPTA-1 acetoxymethyl ester
PP	perforant path
PPD	paired pulse depression
PPF	paired pulse facilitation
PV	parvalbumin
SD rat	sprague dawley rats
SST	somatostatin
STD	short term depression
STDP	spike timing dependent plasticity
STP	short term potentiation
TML	total molecular layer cell
VC	voltage clamp
$\Delta F/F$	Ca <sup>2+</sup> fluorescence increase normalized to baseline